Master of Science Thesis

Torsion Box Rudder Spar Concept Design for Load Alleviation in the Rudder Shells

A Feasibility and Parametric Study Conducted on the Airbus Single-Aisle Rudder

G. M. Maties

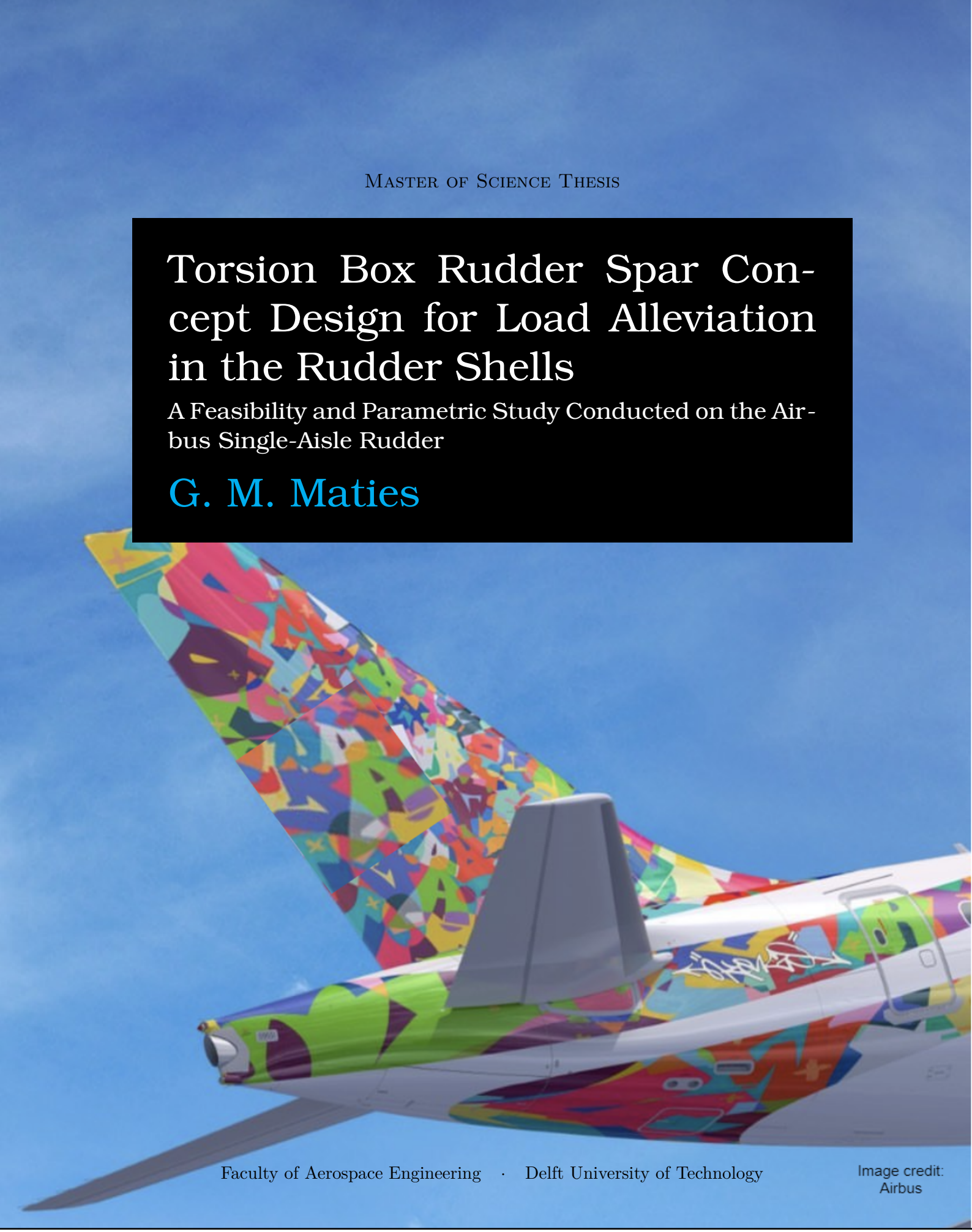

Faculty of Aerospace Engineering · Delft University of Technology

Image credit: Airbus

TU Delft Delft University of Technology

MSCCONFIDENTIAL

Torsion Box Rudder Spar Concept Design for Load Alleviation in the Rudder Shells

A Feasibility and Parametric Study Conducted on the Airbus Single-Aisle Rudder

Master of Science Thesis

For obtaining the degree of Master of Science in Aerospace Engineering
at Delft University of Technology

G. M. Maties

13 December 2023

Faculty of Aerospace Engineering · Delft University of Technology

The work in this thesis was supported by Airbus Operations GmbH. Their cooperation is gratefully acknowledged.

Delft University of Technology
Faculty of Aerospace Engineering
Department of Aerospace Structures and Materials

GRADUATION COMMITTEE

Dated: 13 December 2023

Chair holder:

Dr. Calvin D. Rans

Committee members:

Prof. Dr. Chiara Bisagni

Dr. ir. Daniël M. J. Peeters

Dipl. Ing. Henrik Lüttmann

Abstract

The rudder is one of the few aircraft primary composite structures that experience relatively low external aerodynamic loading during flight. This aspect renders the rudder shell the perfect component to investigate the possibility of using sustainable composite materials, with lower mechanical properties, in aircraft primary structures. However, the rudder must be strong enough to carry potential actuator jamming loads, which do not occur frequently.

This thesis investigates the feasibility of locally redesigning the CFRP rudder spar as a torsion box in order to alleviate the load in the shells and facilitate the internal-external load separation in the rudder, as the actuator brackets are attached to the spar. The goal of the new rudder spar-box concept is to take up the actuator jamming loads, while the shells only carry the relatively low aerodynamic forces, which do not require the use of an extremely strong material.

The attachment of the spar-box to the shells plays a major role in the load distribution, thus two load separation principles are investigated. In the first one, the original spar-shell connection is retained. The addition of the box to the spar increases locally the torsional stiffness and alleviates the loads in the shell. The main advantage is represented by the retention of the fin-rudder connection stiffness ensured by the actuators. The disadvantage is represented by the fact that part of the jamming load is still carried by the shells, as the spar-shell connection provides a load path.

In the second one, the part of the spar enclosed by the box is disconnected from the shells in the area of the actuators (physically this implies the removal of rivets), completely decoupling the jamming load path from the shells. The main advantage is represented by the complete internal-external load separation between the spar-box and the shells. However, the structural de-coupling of the actuators from the shells leads to local stiffness alterations that may lead to major changes in the natural frequencies of the vertical tail.

Moreover, the effectiveness of actuator bracket material change from metallic to composite is also investigated, as the composite brackets can be directly integrated in the spar-box design. Thus, three concepts are analysed and subjected to a trade-off, with focus on static analysis: two concepts incorporate the first principle implemented for both metallic and composite brackets and the third concept is based on the second principle implemented for composite

brackets only. The trade-off results show that due to the lack of bracket design integration in the spar-box design, the first principle implemented for metallic brackets does not reduce the loads in the shells. Both principles perform for composite brackets.

A preliminary design based on static analysis performance assessment (static, modal and buckling) is proposed for the two feasible concepts, identifying the enclosed area as more important than the spar-box thickness in alleviating the loads in the shells. Due to the complete spar-box decoupling from the shells, the decoupled concept is lighter and more efficient in separating the loads than the local torsional stiffens concept, as the required closed area is smaller, but further detailed dynamic analysis is required. The local torsion stiffness concept does not use the material as efficiently as the decouplede concept, because a big profile area is required to alleviate the loads in the shells, which are still partially taken by the shells.

Table of Contents

List of Figures

List of Tables

Preface

I can not imagine a better feeling than waking up and being the person you want to be, living the life you want to live. In my case, becoming an aerospace engineer has always been a significant part of my identity. This Master's thesis marks the end of my eventful student years, full of challenges, meaning and rewards. It also represents a bridge between my academic and industrial knowledge, that enabled me to grow and transition.

The idea of the thesis has roots in the Faster H2 project organised by Clean Aviation, whose work package 3 is concerned with the ECO Rudder design. The rudder spar concept investigated in this thesis would enable the load alleviation of the shells during actuator jamming events and consequently the use of green materials with lower mechanical properties. The proposed structural design can be one of the enablers of sustainable aviation, and I am happy to have contributed to these efforts.

I am grateful to all the people who played a role in shaping me while I was an aerospace engineering student. Particularly, I would like to thank Henrik Lüttmann and Ralf Hilgers for being my supportive supervisors at Airbus, always available to answer my questions, guide me, share with me their expertise and experiences, and discuss the promising and challenging future of sustainable aviation. Special thanks go to Ivano Bertolini and Jens Mozar for enabling my thesis at Airbus, to the Single-Aisle team in particular and to the entire VTP department for their kind support. Thank you.

My gratitude goes to Prof. Chiara Bisagni, for being a constructive critic of my work and providing her invaluable guidance. I am also grateful to all the teachers at TU Delft who inspired me throughout my Bachelor's and Master's and built the mentality of a critical aerospace engineer, who always acts with integrity. Thank you.

TU Delft and Airbus are of great importance to me also because they enabled me to meet some of my best friends, who became like family during my studies, internship and thesis. Thank you for always bringing me joy and making me laugh. Let's set sail for many more adventures!

Nonetheless, I would like to thank my parents and family for their unconditional support and love. And to myself, for caring, persisting, continuously learning and (at least always trying to) do my best.

"The most contrarian thing of all is not to oppose the crowd, but to think for yourself."

— *Peter Thiel, From zero to one*

Nomenclature

Abbreviations

Abbreviation	Meaning
AC	Actuator
Al	Alluminium
BR	Hinge Bracket
CFRP	Carbon Fibre Reinforced Plastics
DFEM	Detailed Finite Element Model
FEM	Finite Element Method
GFEM	Gloabal Finite Element Model
GFRP	Glass Fibre Reinforced Plastics
LC	Load Case
RF	Reserve Factor
VTP	Vertical Tail Plane

Table 1: Abbreviations

Symbols

Variable	Meaning
A	Area
c	Constant
E	Young's Modulus
G	Shear Modulus
l	Length
q_0	Shear Flow Due to Torsion
s	Length Integration Variable
t	Thickness
T	Torque
v	Intermediate Weight Factor
w	Weight Factor
γ	Engineering Shear Strain
τ	Shear Stress
θ	Twist
ε	Axial Strain

Table 2: Symbols

Chapter 1

Introduction

The active use of recyclable materials in aerospace primary components represents one of the industry's priorities in its efforts to make the transition to sustainable serial aircraft production and reduce waste. Given the predominant utilisation of unrecyclable thermoset-based composites in aircraft primary structures, current research, aimed towards the safe and reliable introduction of sustainable composite materials, is widely conducted both in academia and industry.

One of the aerospace industry's endeavours to replace thermoset-based composites in primary structures is represented by the ECO Rudder project undertaken by Airbus, which investigates the possibility of manufacturing the single-aisle sandwich composite rudder out of sustainable materials, including CFRP thermoplastics [46] [30][43][44][12] and bio-composites. Due to the compatible rudder-to-fin attachment design of the single-aisle VTP (Vertical Tail Plane), the rudder is interchangeable, regardless of the aircraft variant, which enables the structure's substitution in the currently active fleet, eliminating the need to wait for the next-generation aircraft to introduce the usage of recyclable materials.

Previous research has systematically identified a lower mechanical performance of recycled and bio-materials, in addition to a scatter increase in the experimentally determined material properties, due to their dependency on the environmental growing conditions [33], [32]. On the other hand, under normal flight conditions, the rudder is a relatively low-loaded structure [1], rendering it the perfect candidate to study the possibility of introducing different types of sustainable materials with lower mechanical properties in primary structures.

However, one key structural aspect has to be treated before the introduction of thermoplastic or lower-performance green materials in the rudder shells is resolutely pursued. Namely, in the area of the actuators, the rudder shells are reinforced in the form of locally extra face sheet layers, due to the possibility of experiencing actuation system failures. This phenomenon is called actuator force fight or actuator jamming (note, that in the context of this study, jamming is not used with the meaning of physical jamming), which is characterised by the situation when one malfunctioning actuator acts in the opposite direction than the other actuators, leading to local introduction of high torsional loads in the shells.

These locally high torsional loads need to be supported by a strong connection (and material). Thus, at a first glance, lower-performance materials can not be used in the rudder shells. Moreover, an out-of-the-autoclave multi-layer thermoplastic-based shell design could pose manufacturing complications.

However, actuator jamming occurs with very low frequency (a few yearly cases for the entire fleet). Therefore, the capabilities of the high-strength material would be rarely required. The introduction of sustainable materials with lower strength or one-layer thermoplastic rudder shells would be possible if another structure would bear the torsional loads induced by the actuator jamming and the shells would only carry the aerodynamic loads.

One solution that would enable the required load separation is a local redesign of the rudder spar as a torsion box. Hence, the current study aims to provide a feasibility study, concept proposal and preliminary design optimisation of a rudder spar-box, sized for static loading [28], [9].

This study represents the first step in enabling the pursuit of sustainable material introduction in the sandwich rudder design, by investigating whether the internal-external load separation is possible without a significant rudder weight increase. Subsequently, for the current rudder torsion box spar feasibility study, the thermoset CFRP rudder shell material properties are retained, due to their similar mechanical properties to thermoplastic-based composites, as the carbon fibres are the main load carrier.

If the rudder torsion-box spar concept feasibility for static loading can be proven for thermoset CFRP unreinforced shells, the next step could be represented by extending the research, calculations and design proposals to VTP models featuring different rudder shell materials. While the use of bio-materials would render the rudder a completely compostable structure, the introduction of novel concepts in the aerospace industry is a gradual process, due to strict certification requirements.

The thesis outcome forms the basis for future studies regarding rudder shell design solutions which can be based on both thermoplastic CFRP or green composites with different material properties than the current ones. Eventually, a rudder prototype with thermoplastic or bio-composite shells and a torsion-box spar could be built and tested to validate the spar-box concept integration in the VTP design.

Moreover, the relevance of the project is bolstered by the lack of studies regarding recyclable sandwich rudders. While Fokker successfully designed a thermoplastic multi-rib rudder and implemented it in the Gulfstream G650 design [21], [1] the use of sandwich structures for the moveable part of the VTP has better weight performance and fewer components [17].

The study commences with the presentation of the current single-aisle rudder geometry and components, its corresponding FEM (Finite Element Method) idealisation and the overall load envelope in chapter 2, describing thus the unmodified input provided by Airbus. The torsion spar-box concept generation process and the identified possible designs are presented in chapter 3, which are subsequently subjected to a trade-off process, presented in chapter 4. The feasible concepts are optimised for weight reduction in chapter 5 and chapter 6, ending the study with the conclusions in chapter 7.

Chapter 2

Airbus Single Aisle Rudder Design Overview

This chapter aims to present the design starting point and the unmodified input provided by Airbus, describing the current Airbus Single Aisle rudder geometry in section 2.1, relevant flight scenarios and corresponding load envelope in section 2.2 and the structural idealisation and finite element method (FEM) modelling of the VTP in section 2.3, which has been received from Airbus. The provided FEM model is verified and validated by Airbus.

Since no alterations or structural analyses have been performed on any other VTP component besides the rudder, such as the rear fuselage or the VTP fin, the description is provided for the rudder only, as it is the main focus of the current study. Information regarding the other components does not influence the outcome of the study.

2.1 Airbus Single Aisle Rudder Overview

The first section presents the main rudder structural components and summarises the materials utilised in the rudder design in subsection 2.1.1. The general rudder overview is complemented by a brief description of the rudder attachment to the VTP fin and actuation system in subsection 2.1.2.

2.1.1 Rudder Structural Components and Materials

The Airbus Single Aisle rudder is a 6.6 m high structure that consists of 15 main structural elements: 2 rudder sandwich shells, a metallic tip, a monolithic CFRP C-shaped spar, a monolithic CFRP root rib and 10 metallic brackets (or fittings) riveted to the spar, as depicted in Figure 2.1. The rudder is attached to the VTP fin through 7 metallic hinge arms and 3 actuators, the spar providing the interface for the rudder connection to the VTP fin, accommodating the 3 metallic actuator fittings (AC) and 7 metallic hinge arm fittings (BR), with their location along the spar illustrated as well in Figure 2.1 and Figure 2.2.

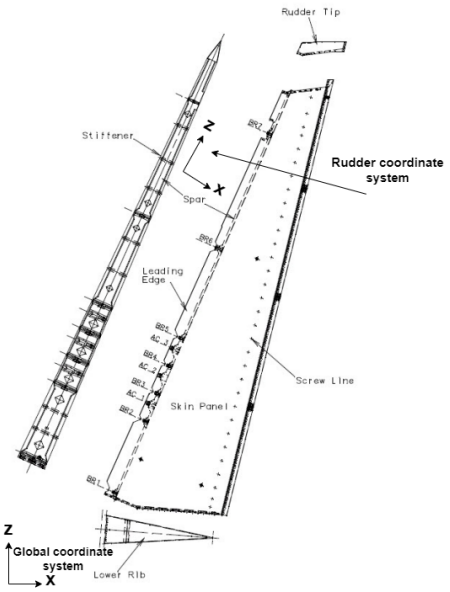

Figure 2.1: Rudder Components Overview (Airbus Courtesy)

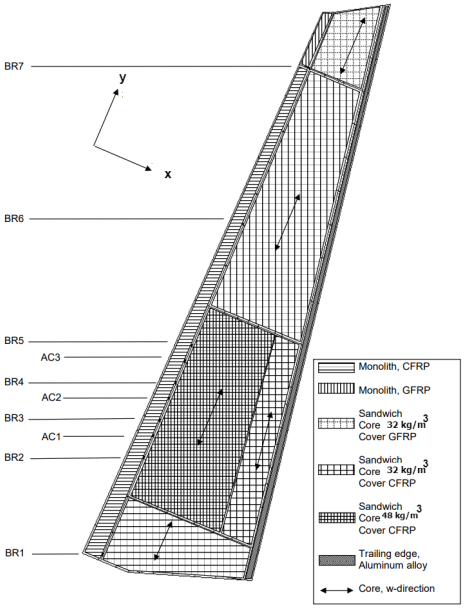

Figure 2.2: Rudder Materials Overview (Airbus Courtesy)

All CFRP monolithic components (including the sandwich face sheets) are manufactured out of bi-woven fabric, hence a layer orientation of 45° automatically entails a set of fibres oriented in the -45° direction, and a layer oriented of 0° automatically implies the presence of a layer of 90° as well, one CFRP fabric layer having a thickness of 0.35 mm. Towards the rudder tip, the shell's face sheets are made out of glass fibre-reinforced plastic (GFRP) fabric, to provide lighting strike protection.

Moreover, the sandwich shell core is a Nomex honeycomb structure, irrespective of the face sheet, and the brackets are made out of a typical aluminium alloy. The mechanical properties of the materials utilised in the rudder are summaries in Table 2.1 with the material distribution in the rudder shells illustrated in Figure 2.2.

Material	$\rho[kg/m^3]$	E_{11} [MPa]	E_{22} [MPa]	ν_{12} [-]	G_{12} [MPa]	G_{23} [MPa]	G_{13} [MPa]
CFRP	1600	66600	66600	0.03	3400	-	-
GFRP	2550	19500	19500	0.044	1800	-	-
Nomex	32	1	1	0.9	1	12.4	15.2
Nomex	48	1	1	0.9	1	19	31
Al alloy	2800	71	-	0.33	28300	-	-

Table 2.1: Rudder Materials Properties

Each rudder shell has a 30 mm Nomex honeycomb core and two 45° carbon fabric face sheets, as they mainly carry shear, one on the inside and one on the outside of the core. As depicted in Figure 2.2, there is a reinforced (or booster) area in the actuator region in the form of additional 0° layers, reinforcement determined by the calculations for actuator force fighting

cases. In the booster area, the core has a density of 48 kg/m^3 and in the rest of the rudder, the core has a density of 32 kg/m^3.

The 32 kg/m^3 core was chosen to avoid the core crushing due to the high pressure in the autoclave during shell curing, and the 48 kg/m^3 core in the booster area was chosen due to locally increased loads in the case of system malfunction. Due to the sandwich structure of the shells and selected core height, their bending stiffness is high and therefore the structural architecture of the shells does not have to make use of ribs or stringers to avoid buckling.

In order to provide the interface for spar joining, the rudder shells present a curved monolithic overhang area at the leading edge. The transition from sandwich to monolithic is achieved with a ramp-down, as depicted in Figure 2.5 and Figure 2.6. Some 0° layers of the monolithic overhang area extend a few tens of centimetres to the sandwich shells to provide a smooth transition between the monolithic overhang area and the sandwich shells.

The spar is also made out of fabric, with 45° layers placed outwards and 0° layers in the middle, varying in number from 10 in the actuator region to 2 towards the tip, which is not highly loaded. The bottom rib has a constant thickness with layers oriented mostly in the 0° direction.

Three coordinate systems are used throughout the thesis to describe the VTP geometry and results: the global (aircraft) coordinate system with the origin in the aircraft centre of gravity, depicted in Figure 2.1 (only the orientation of the axes), in which the rudder sweep is defined and FEM illustrations are provided; the rudder coordinate system, which is the global coordinate system rotated by the sweep angle of the rudder, also illustrated in Figure 2.1, in which the rudder components' displacements and xy-plane views are always reported; and the analysis/material coordinate system in which the rudder shell strains are reported throughout the thesis, shown in Figure 2.2, all systems having the third axis oriented inwards the page.

2.1.2 Rudder to VTP Fin-box Attachment

The rudder is attached to the VTP fin through 7 metallic, triangle-shaped hinge arms, illustrated in Figure 2.3 (BR span-wise locations, see Figure 2.2) and 3 actuators, depicted in Figure 2.4 (AC span-wise locations, see Figure 2.2).

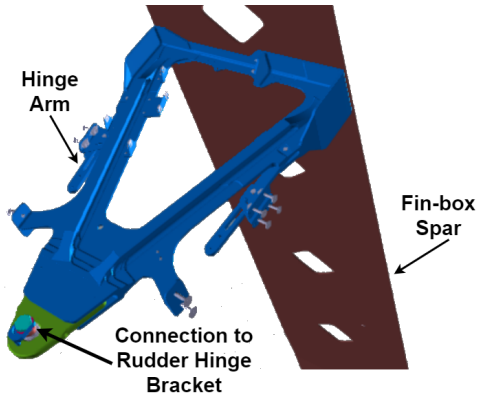

Figure 2.3: Hinge Arm Design (Airbus Courtesy)

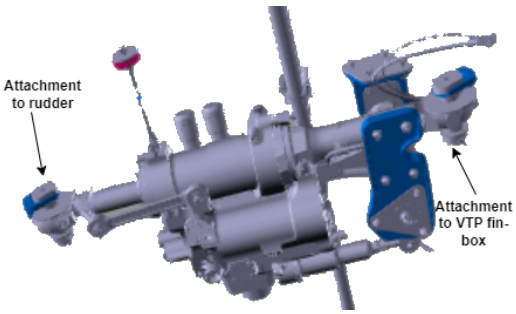

Figure 2.4: VTP Actuator (Airbus Courtesy)

The hinge is placed along the ”symmetry line” of the rudder, thus the design of the 7 hinge brackets, shown in Figure 2.5, has a rounded attachment area in the middle to accommodate the bolt connecting the rudder to the hinge arms. The VTP half that contains the rudder actuation hinge line is referred to as the left-hand side, its position being chosen to create a hinge moment due to the actuator forces, the actuator bracket being depicted in Figure 2.6. The 10 metallic brackets are double-flanged and each flange has a gradual thickness variation of up to 10% from the bolt region to the extremities, obtained through milling.

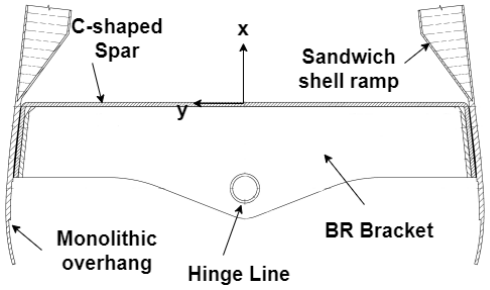

Figure 2.5: Hinge Brackets Design at BR Locations (see Figure 2.2) in the Rudder Coordinate System (Airbus Courtesy)

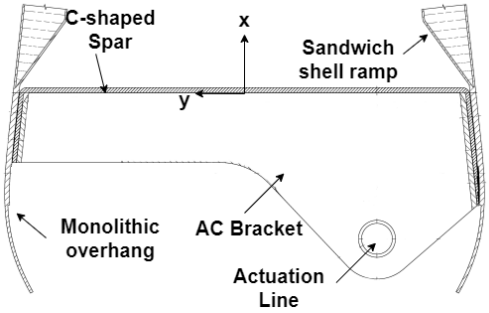

Figure 2.6: Actuator Brackets Design at AC Locations (see Figure 2.2) in the Rudder Coordinate System (Airbus Courtesy)

The Single Aisle rudder is currently actuated mechanically and displaced hydraulically, the three actuators being placed at a 60° angle with respect to the spar web in the undeflected rudder state. This angle minimises the distance between the rudder spar and fin spar while still providing enough actuation force in the x-direction, as the length of the actuator is a fixed input during the VTP design. The rudder is deflected as the actuators retract (negative deflection of the rudder to the left-hand side (LHS) as depicted in Figure 2.7) or extend (positive deflection to the right-hand side (RHS) as depicted in Figure 2.8).

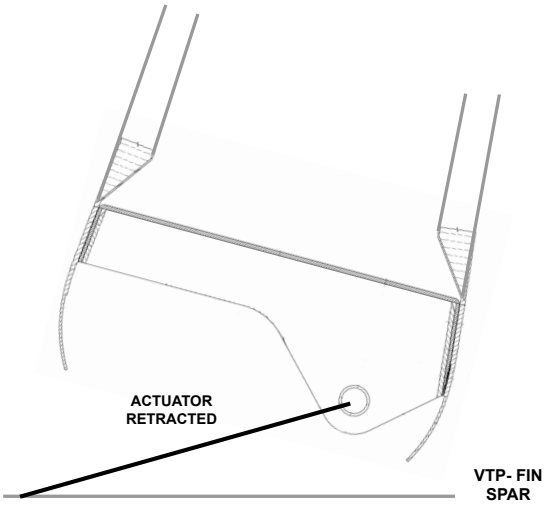

Figure 2.7: LHS Deflection

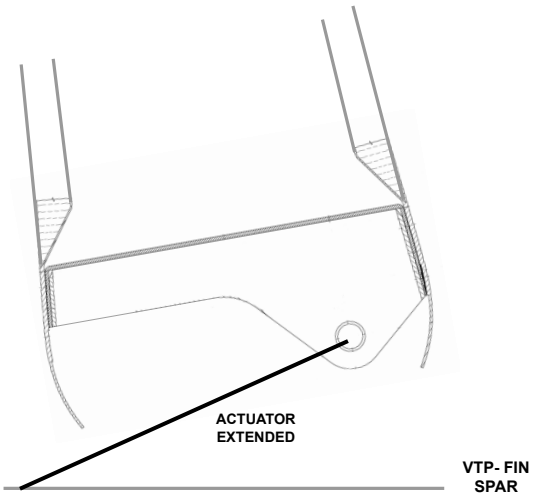

Figure 2.8: RHS Deflection

The actuators are displacement-controlled, the rudder being always deflected to the target angle with full speed. Due to the rudder deflection, an aerodynamic force develops perpendicular to the shell surface, giving rise to an aerodynamic hinge moment, which is in equilibrium with the rudder hinge moment, created by the reaction forces that develop in the actuator. The load generation and interaction in the rudder are further detailed in the following section 2.2.

2.2 Rudder Operational Role and Loads

The VTP has to fulfil three main functions: provide equilibrium, control and stability in the yaw direction during certain flight conditions. The most important flight scenarios for the VTP sizing are lateral gusts, crosswind landings, one engine out conditions and yaw manoeuvres.

In the context of the flight conditions mentioned above, there are four types of loads acting on the VTP: aerodynamic (external) loads, given by the pressure distribution that develops on the VTP surface when the rudder is deflected or when the VTP surface is hit by lateral gusts, described in subsection 2.2.1; inertial loads, due to the aircraft acceleration (and VTP weight); system failure (internal) loads, caused by the malfunction of the actuation system in the form of force fighting between the three actuators, case in which one of the actuators acts against the other two (e.g. one extending when the other two are retracting), detailed in subsection 2.2.2; thermal loads, induced by the material expansion or contraction at different flight atmospheric conditions, presented in subsection 2.2.3.

The external (aerodynamic) and inertial loads are superimposed to provide the external limit load envelope, and the FEM analysis is run with all types of loads applied, including thermal loads and the internal (system failure) loads, to give the complete VTP loading. The following subsections provide a more detailed overview of the VTP (and implicitly rudder) sizing loads.

2.2.1 Aerodynamic (External) Loads and Inertial Loads

The first step in identifying the sizing load cases (LCs) for the VTP sizing is the creation of a load envelope at different span-wise locations for a handful of relevant flight scenarios. While a wide range of possible flight conditions are known, the ones leading to the highest loads can only be identified by plotting the complete load envelope.

The most relevant load envelope is the one corresponding to the VTP root, at the VTP-fuselage interface, where the loads attain the highest values. The load envelope utilised for the rudder design contains the reaction fin-box bending moment (around the x-axis) at the VTP-fuselage interface against the rudder hinge moment, these two being the relevant loads for the rudder sizing load case selection.

For each of the selected cases to create the envelope contour, the numerical values of the bending moment at the VTP-fuselage interface and the rudder hinge moment are obtained from a stick model of the aircraft, where the different flight conditions are implemented (including flight derivatives, Mach number, angle of attack, etc.). In this model, for each flight condition, the aerodynamic load distribution, obtained from the Double Lattice Method [41], corrected for wind tunnel experimental results, and the inertial loads, given by the accelerations corresponding to the flight scenario, are simultaneously applied.

The rudder is not perfectly symmetric due to heavier reinforcements on the left-hand side, actuator load application point and actuator bracket geometry. Hence, for each load scenario, both rudder deflection directions must be assessed.

While assuming rudder symmetry could be appropriate for the development of analytical calculations, slightly different results for the two rudder deflections could be obtained from FEM simulations (in the order of tens of micro-strains). The reaction forces at the VTP root are not different for the two deflections, but the component strains obtained from FEM analysis could be, due to the slight rudder asymmetry.

Instead of caculating two different load cases, the reaction loads are generated for one rudder deflection only and the numerical values are mirrored about the origin to account for both positive and negative rudder deflection, as shown in Figure 2.9. This approach has been validated by Airbus with past simulations.

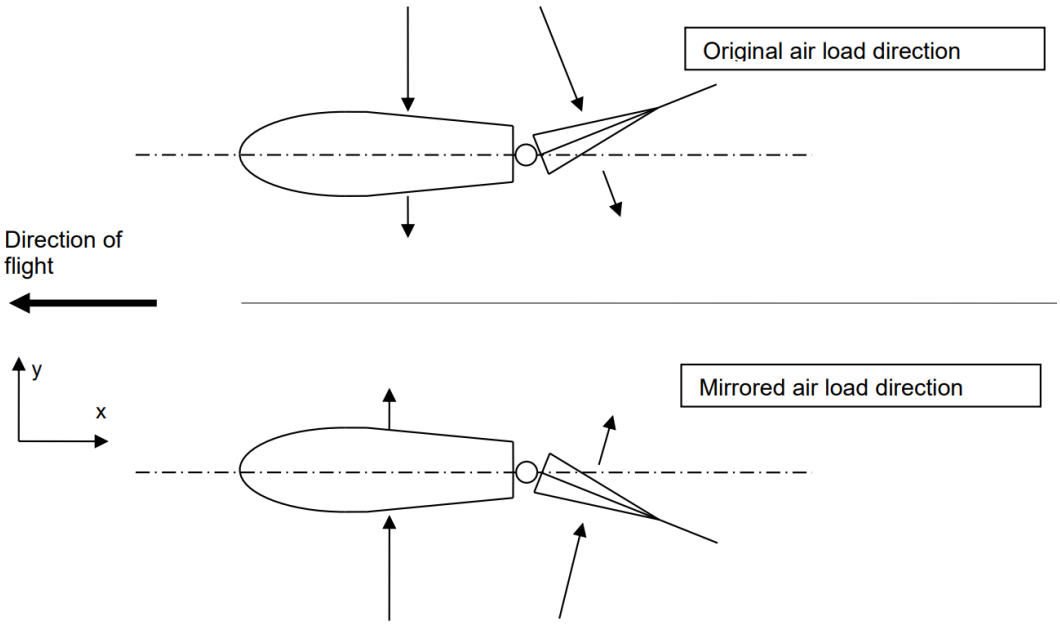

Figure 2.9: Mirrored Loads Visualisation (Airbus Courtesy)

The external limit load envelope for the operational conditions mentioned above has been provided by Airbus and is depicted in Figure 2.10 for fin-box bending vs. hinge moment at the VTP root, relevant for the rudder design. This plot will be used in the subsequent chapter for sizing load selection to reduce the number of analysed load cases.

The green dots represent the load state for different load cases, and the yellow envelope defines the boundaries of attainable limit loads during the aircraft operation. Moreover, cruise yaw manoeuvres and cross-wind landings have been put together under the general category of yaw manoeuvres.

As it can be seen in Figure 2.10, the gusts have the highest bending moment without any hinge moment since the sizing gusts occur during the cruise flight when the rudder is not deflected. Thus, it can be expected that the gust conditions will not entail high strain levels in the rudder. The yaw manoeuvre case is characterised by a combination of relatively high bending

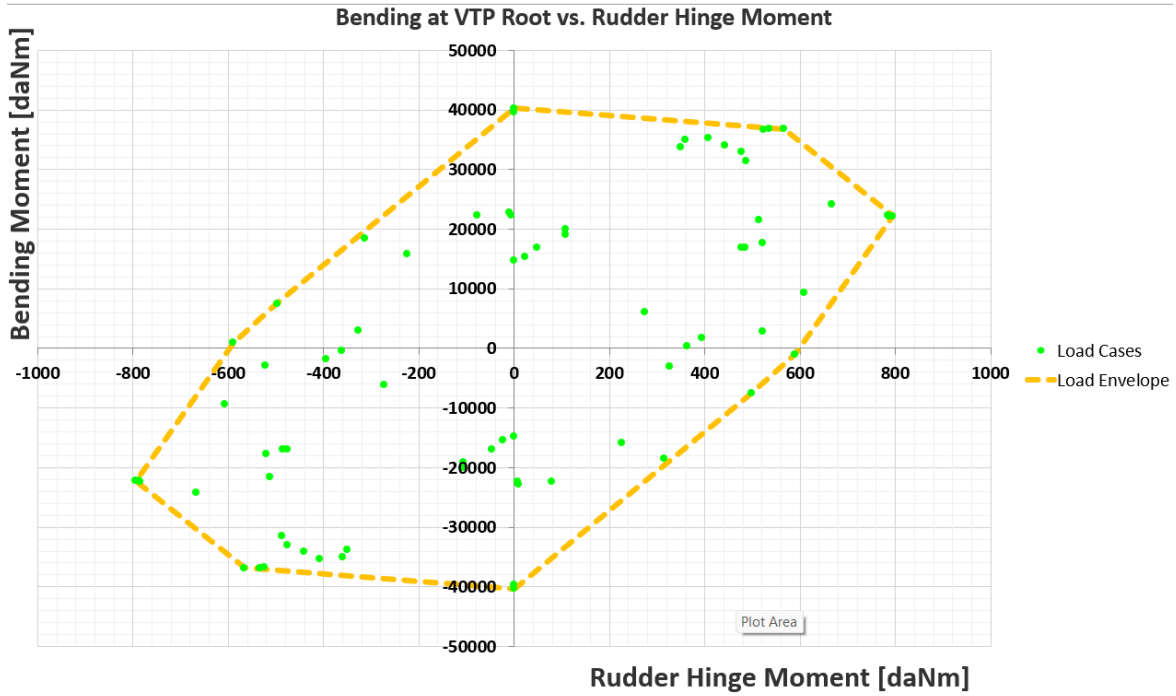

Figure 2.10: External Load Envelope at the VTP Root: Bending Moment of the Fin vs. Rudder Hinge Moment (Airbus Courtesy)

and high hinge moments, while the one engine out case is characterised by relatively low bending moment but high hinge moment, highest on the envelope, as big rudder deflections are needed to balance the resulting moment.

2.2.2 System Failure (Internal) Loads

The rudder is actuated by three hydraulic pistons, having a positive deflection (to the right) when the actuators are extended and a negative deflection (to the left) when the actuators are retracted. The actuators are displacement controlled, meaning that there is a rudder displacement (angle) target for any load condition, the rudder being always actuated with maximum (constant) speed, irrespective of the target deflection.

At the required rudder deflection angle, the actuator valve is closed, keeping the rudder in position, the reaction forces that develop in the actuator providing the equilibrium reaction moment to counteract the aerodynamic loading.

More precisely, the actuator reaction force component in the x-direction, multiplied by the distance from the actuation point to the hinge point (the actuator moment arm), provides a moment in the z-axis that counteracts the aerodynamic hinge moment.

The aerodynamic force is generated perpendicular to the rudder shells, with the main contribution in the y-axis, which multiplied by the distance in the x-direction between the resultant load point and hinge line creates the moment around the z-axis that has to be counteracted. The aerodynamic hinge moment is the result of this y-force multiplied by the distance in the

x-axis from the aerodynamic resultant to the hinge line. The hinge moment equilibrium is illustrated in Figure 2.11.

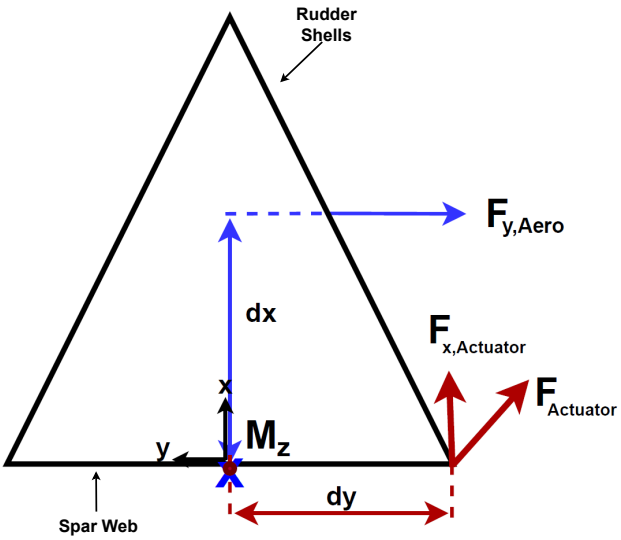

Figure 2.11: Hinge Moment Equilibrium Viewed on a Simplified Rudder Shell Cross-section Sketch in the Rudder Coordinate System (Sandwich Core and Actuator Bracket are not Represented for Simplification Purposes)

Malfunctions of the actuation system, actuator force fighting in particular (referred to also as jamming, a direct consequence of the displacement-controlled nature of the actuation system), can lead to high load introduction in the rudder shells. This also represents the reason why there are three actuators: one actuator can act in the opposite direction than intended, while the other two actuators function properly. In this case, one of the functioning actuators balances the malfunctioning actuator, and the third one is deflecting the rudder to the desired angle. In this way, the target deflections can always be attained due to the actuator redundancy and the actuation system is operationally safe.

As presented in Table 2.2, in the context of the flight scenarios with the associated external loading (load case id given by the cursor i), any of the three actuators can fail (while extending or retracting), leading to 7 subcases per load case, no actuator failure being the seventh subcase. Eventhough the subcases when the same actuator is retracting or extending generate very similar load levels and reserve factors, both subcases are considered due to the reserve factor sensitivity for values around 1.

Load Case Numbering	Load Case
LC-i-00	No Actuator Force Fighting
LC-i-01/02	Actuator 1 Retracting/ Extending
LC-i-03/04	Actuator 2 Retracting/ Extending
LC-i-05/06	Actuator 3 Retracting/ Extending

Table 2.2: Actuator Force Fight Load Subcase Nomenclature

The two movement possibilities per actuator (extending or retracting) also account for the

original and mirrored loads. While the aerodynamic loading is the same, the orientation of the jamming load differs.

As the actuators function always at full speed, a load as high as 56kN can develop in the actuators, which is considered to be an ultimate load. In case of system failure, this load can be locally introduced in the rudder shells through the actuator brackets and spar, being transmitted as a torsional load span-wise, and is the load that sizes the rudder shell reinforcement.

2.2.3 Thermal Loads

Each one of the loading scenarios can occur at any flight altitude, where the air temperature is different, inducing additional loads in the structure due to the contraction or expansion of the materials. By initial design requirements, the highest temperature the VTP has to withstand is 80 $°C$ and the lowest design temperature is $-54°C$.

The addition of the temperature loads leads to 14 load subcases per load case so far, as the 7 actuator failure subcases load scenarios can occur in the context of the two limit temperatures. In Table 2.3 the subcase notation given the addition of thermal loads is provided, where i is the main load case cursor and j is the system failure case cursor.

Load Case	Temperature [$°C$]
LC-0i-0j-01	80
LC-0i-0j-02	-54

Table 2.3: Thermal Load Subcase Nomenclature

2.3 FEM Modelling of the Current Single Aisle Rudder

This section aims to present the structural idealisation and FEM modelling of the real rudder geometry, modelling assumptions and their effect. The simulations are conducted on a global finite element model (GFEM) of the VTP including the aft fuselage, with the utilised FEM solver being NASTRAN, the pre-processing is performed in Hypermesh and post-processing is conducted in Hyperview.

The NASTRAN cards [36] utilised throughout the entire study are briefly presented in subsection 2.3.1, completed by the structural idealisation of the VTP in subsection 2.3.2 and FEM meshing in subsection 2.3.3. The applied boundary conditions are presented in subsection 2.3.4 and subsection 2.3.5, and the utilised load factors are explained in subsection 2.3.6. Finally, the result post-processing methodology, which also accounts for result validation, is detailed in subsection 2.3.7.

2.3.1 NASTRAN Commands Overview

When using NASTRAN as the FEM solver, each element is assigned the constituting grid points (nodes), a material property and in the case of composites, the material coordinate

system. Each grid point is defined by its coordinates in a specified coordinate system and is assigned a coordinate system in which the results are given. The VTP GFEM contains only 2D, CQUAD4 (4 nodes) and CTRIA3 (3 nodes) elements, in the rudder shells, spar, rib and brackets, due to the relatively small thickness of the components compared to the component dimensions.

Moreover, the actuators and the hinge arms, which are very stiff metallic components, are modelled with 1D CROD elements, equivalent to truss elements, that can only take up tension, compression and torsion, but no bending. Given that the ends of the actuators and hinge arms accommodate hinges for the VTP-rudder connection and there are no translational z-forces, the actuators mainly take up axial x-forces and the hinge arms carry x and y axial forces. As the resulting bending moments are negligible, the actuators are modelled as one CRDO element, in the corresponding orientation of the undeflected rudder, and the hinge arms are modelled with three CROD elements, in the shape of a triangle.

For the 2D elements, only two types of properties are used: PSHELL and PCOMP. PSHELL is defined by the material mechanical properties and element thickness, making it ideal for modelling metallic parts. It can also be used for composites during the design process if the target laminate properties are known but not the thickness and exact fibre sequence. The required laminate thickness to meet sizing requirements can be determined by assigning different thicknesses to the PSHELL property.

Once the approximate required thickness is known, the transition to a more accurate, PCOMP property definition can be made, defining the layer sequence, based also on the composite design guidelines. The PCOMP card requires the laminate reference plane (where through the thickness is the load applied), the fibre orientation, the thickness and material of each layer.

The material cards used in the GFEM model are MAT1 for isotropic and MAT8 for orthotropic materials (composites).

The loads are modelled by first determining the nodal force component magnitudes in the grid point coordinate system, defined with the FORCE card. The original aerodynamic load distribution is fitted to a function that can yield the force magnitude at the location of the FEM nodes. Subsequently, a LOAD card can collect the FORCE cards, enabling the application of general load factors, such as the ultimate load factor.

Boundary conditions are defined mainly with two NASTRAN cards: SPC (single-point constraint) and MPC (multi-point constraint). With the SPC card, the numerical values of the boundary conditions (0 or enforced displacement) can be assigned to the 6 nodal degrees of freedom. With the MPC, a dependent motion of a dependent node can be defined, with respect to an independent node.

They are used at the three main VTP interfaces: between the fin root and the fuselage, at the bracket-actuator /hinge arm on both the fin and the rudder side. Moreover, the MPC card is also used to simulate a virtual deflection of the rudder, by rotating the resultant force at the bracket-actuator /hinge arm interface by the deflection angle associated with the load case. This enables the correct force transfer between the rudder and the fin.

In the case of enforced displacements, the SPCD card can be used, which acts as both a loading and a boundary condition. It is especially advantageous when it is desired to isolate a sub-component from a larger analysed structure.

2.3.2 VTP FEM Idealisation and Assumptions

The VTP GFEM mesh created and provided by Airbus is depicted in Figure 2.12 in the global coordinate system, with the current rudder modelling illustrated in Figure 2.13, where the span-wise locations of the 2D FEM AC brackets model, hidden by the rudder shell, are also indicated. Each colour indicates elements with different properties (e.g. different thicknesses, materials or layup sequences). The Z-strut indicated in Figure 2.13 is a connection between the fin-box and rudder that carries vertical loads, attached to BR 6.

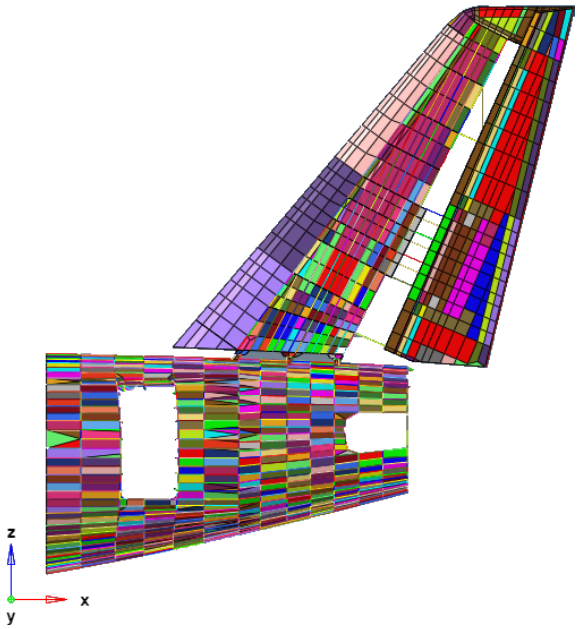

Figure 2.12: GFEM VTP Model in the Global Coordinate System

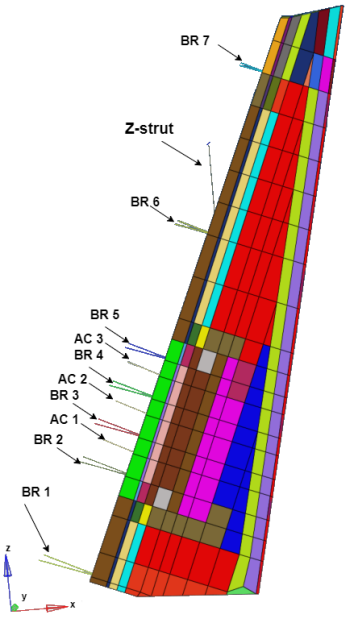

Figure 2.13: Current Rudder FEM Model

For the rudder analysis, a GFEM of the rear fuselage and vertical tail system is utilised for the calculations, to simulate different rudder deflections, as well as the internal system loads between the VTP fin-box and the rudder. The aft fuselage section is modelled as well to avoid the use of rigid elements to simulate the fuselage-VTP interface.

The GFEM represents an idealisation of the real structure, meant to capture the stiffness of large components, such as the VTP, being suitable for preliminary designs [13]. Thus, simplifications and assumptions have to be performed to obtain reliable results in a relatively simple manner. The simplifications performed for the rudder idealisation only (the structure defined by Figure 2.13, including the actuators and hinge arms) are enumerated below, reminding that the current study is meant to provide a preliminary sizing of the rudder spar-box concept, the assumptions being appropriate for a preliminary study.

1. Thin-wall structures have been assumed, as the component thicknesses are generally 10 times smaller than the other geometrical dimensions, which enables the use of 2D elements

2. The sandwich shell ramp-down is captured by one row of elements only (third row in

Figure 2.13) with the average thickness of the ramp (full sandwich thickness divided by two, thus 15 mm)

3. The actuators and hinge arms are modelled with 1D elements, as explained in subsection 2.3.1

4. The overhang area is represented as a straight geometry, given that in reality, it is slightly curved, the idealisation being depicted in Figure 2.14. The overhang is represented by two rows of elements only (in Figure 2.13, the first row and the second row, the later one corresponding to the size of the spar flange due to the riveted interface)

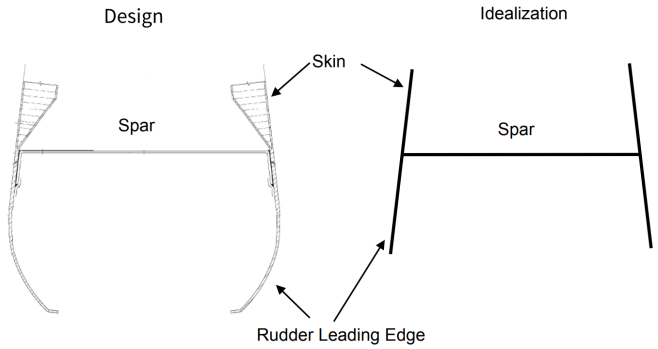

Figure 2.14: Rudder Leading Edge Structural Idealisation (Airbus Courtesy)

5. The sandwich rudder shells are modelled with 2D elements as the core does not carry (significant) loads, but the PCOMP properties assigned to the shells contain the thickness of the core [13]

6. The hand holes present in the rudder spar are not modelled (argumentation provided below)

7. The brackets are modelled in 2D as one flange with the thickness of the two real flanges combined, with three different thicknesses assigned in three different regions, to simulate the varying thickness, the comparison between reality and FEM model being provided by Figure 2.15 and Figure 2.16

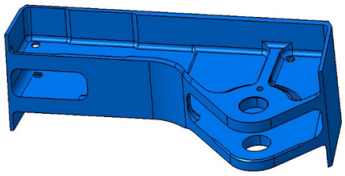

Figure 2.15: AC Bracket in Reality

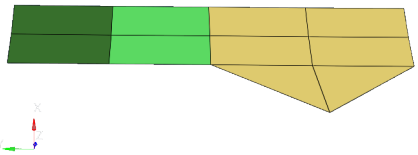

Figure 2.16: AC Bracket 2D FEM Idealisation and Mesh

8. The joints (rivets and bolts with corresponding stiffnesses) are not idealised, the connections being simulated by common grid points (nodes)

9. The spar flanges and rudder overhang elements are superimposed as two elements on top of each other (thickness offset not taken into account due to its small value)

The GFEM results should represent the overall stiffness distribution through the structure and the far-field strain and stresses, that enable the provision of a reliable spar-box preliminary design. Given that no fatigue studies are performed on the brackets, the 2D representation should correctly capture their stiffness in the context of the entire VTP.

Moreover, the sandwich shells are modelled with 2D elements because the GFEM aims to represent their stiffness in the context of the entire VTP and compare their strains with the ones experimentally obtained [13]. Since the study does not aim to model the damages in the sandwich structure [16] or investigate the structural behaviour for the buckling[39] or impacts [23] of the face sheets and core using the FEA method, the shells are not modelled with 3D elements and the face sheets and the core are not modelled with separate elements.

The hand holes present in the spar are relatively small (smaller than the size of one GFEM element) and in reality, the load can be successfully redistributed in the area of the cut-outs, as demonstrated by Airbus structural validation tests. Hence, the inclusion of details such as the hand holes in the GFEM modelling would not contribute to the evaluation of the preliminary rudder spar-box concept.

2.3.3 FEM Meshing

As presented in the previous subsection, the VTP GFEM also contains the aft part of the fuselage, modelled to avoid the overestimation of the fuselage-VTP stiffness. While the fuselage idealisation is not relevant for the calculations (post-processing not performed for the fuselage), it avoids the use of very rigid elements, which could lead to underestimated VTP displacements. An overview of the utilised elements is summarised in Table 2.4.

Component	Elements	Property	Number
Rudder Shells	CQUAD4	PCOMP	482
Rudder Shells	CTRIA3	PCOMP	12
Actuators	CROD	BEAM	3
AC Brackets (3)	CQUAD4	PSHELL	24
AC Brackets (3)	CTRIA3	PSHELL	6
Hinge Brackets (7)	CQUAD4	PSHELL	42
Hinge Brackets (7)	CTRIA3	PSHELL	28
Spar	CQUAD4	PCOMP	134
Rib	CQUAD4	PCOMP	10

Table 2.4: FEM Elements Summary

The rudder shells, spar and bottom rib are modelled with a PCOMP property card applied to CQUAD4 and a few CTRIA3 elements, as the fibre orientation in each ply is known and well-defined. The few CTRIA3 elements are used due to the rudder taper but are not located at critical (highly loaded) points. The brackets are assigned PSHELL properties due

to the isotropic material (aluminium alloy) and the actuators and hinge arms are modelled as CROD elements. They are more rigid, but they are not located in critical (or high) strain-level regions, thus their usage shall not negatively influence the results.

At the element level, the load is applied at the specified reference plane in the PCOMP card. In the monolithic areas (such as the spar web), the reference plane is set to -0.5 of the thickness. In the case of the sandwich rudder shells, the reference plane is set to 0, because the load is introduced at the outer face sheets, due to their connection to the monolithic overhang area. The composite stacking vector is oriented inwards, indicating the direction of the stacking sequence starting at the reference plane (the outer fabric layer), as depicted in Figure 2.17 by the white arrows in the FEM model of the left-hand shell and indicated in Figure 2.18 by arrows for the real structure. This modelling captures the bending effect [14].

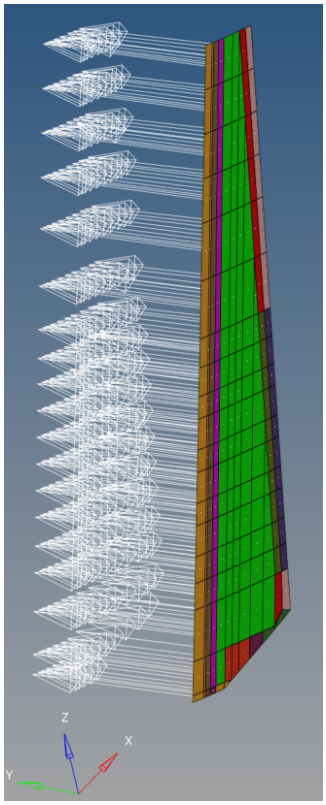

Figure 2.17: Mesh Staking Orientation Vector

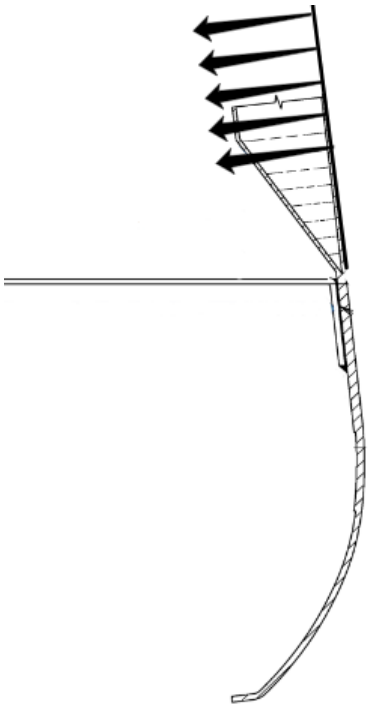

Figure 2.18: Stacking Orientation Vector on Real Shell Geometry

The 10 brackets are metallic and modelled with a PSHELL property card, the thickness variation being captured by three different thicknesses assigned to the property cards of each bracket, emphasized by the three different colours depicted in Figure 2.16. In reality, the brackets have two flanges, but in the GFEM they are modelled in 2D as one flange with the thickness of the two flanges combined. The actuators and the hinge arms are simply modelled as CROD elements.

2.3.4 Boundary Conditions

The hinge arms and actuators provide the boundary conditions (BCs) applied on the rudder. There are in total 13 connection points (or nodes with applied BCs) that define the VTP fin-rudder connection: 7 hinge points on the rudder side (the hinge arms are riveted at the fin-box side, hence, this connection is modelled by sharing element nodes), 3 actuator-rudder hinge points and 3 fin box-actuator hinge points.

At the 10 hinge points defined on the rudder brackets, the rotational degrees of freedom around x and y-axes are set to 0 through the use of SPCs, and the translational degrees of freedom are defined by MPCs, to simulate the rudder deflection, further explained in the next subsection. The nodes on which the boundary conditions are applied on the rudder-side brackets (the structure of interest in this study) are emphasised as white dots in Figure 2.19, which depicts the rudder shells, spar, actuator and hinge brackets mesh.

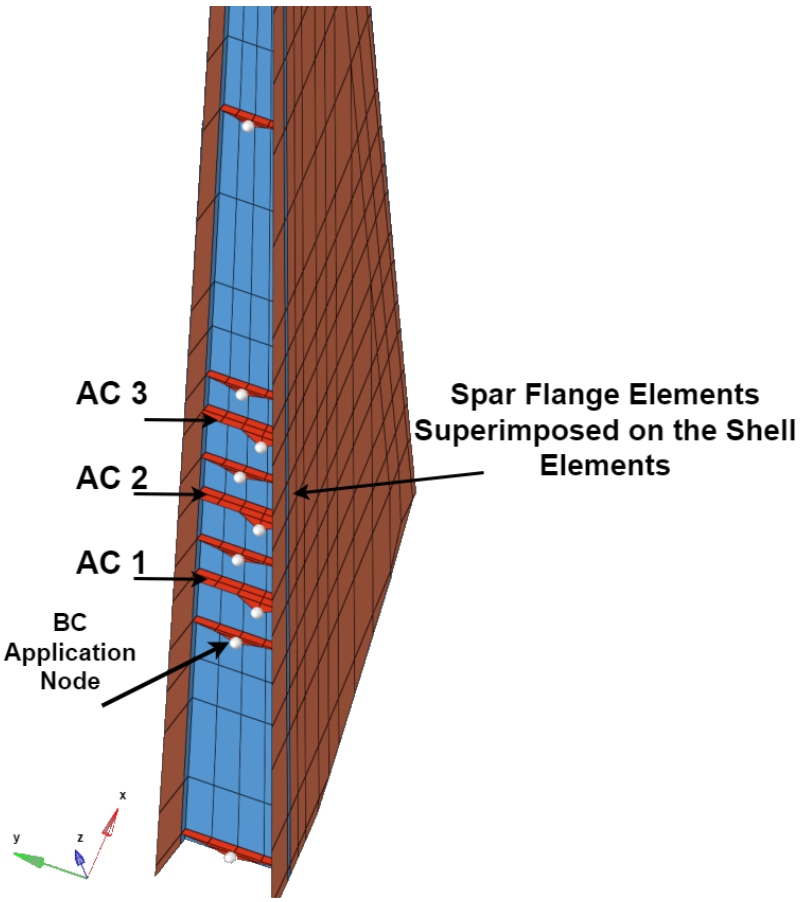

Figure 2.19: Boundary Conditions Application Nodes on the Rudder-side Brackets, Depicted on the Rudder Shells, Spar, Actuator and Hinge Brackets GFEM Mesh. Each Colour Corresponds to a Different Structural Component

2.3.5 Loads and Virtual Deflection

The loads are defined at the shell nodes (thus surface) by adjusting an experimentally determined aerodynamic pressure to match the resultant reaction loads provided in the load envelope (Figure 2.10) and as explained in subsection 2.2.1. At each node, the FORCE card is used to define the load magnitude, and the forces are collected by LOAD cards to define different load cases. The actuator force fighting loads are applied on the actuator node at the actuator-rudder connection, as depicted in Figure 2.20.

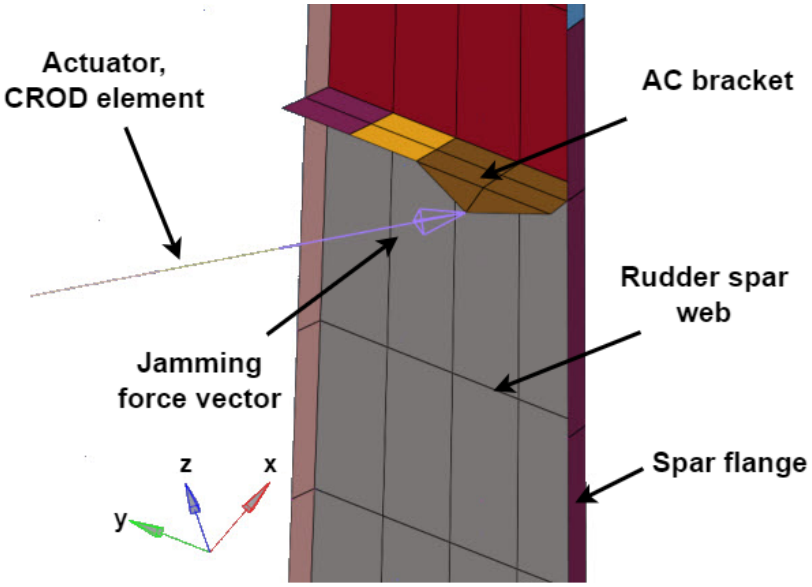

Figure 2.20: Actuator Force Fighting Load Application

One GFEM geometry with 0° rudder deflection is used for all load cases, which, in reality, entail different rudder deflections. This approach avoids the laborious creation of different GFEM models but leads to inaccurate load transmission at the actuator interface. Consequently, the use of MPCs at the rudder-actuator connection grid points ensures the virtual rudder deflection and the correct resultant load transmission.

The independent grid point is always defined on the actuator and hinge arm and the dependent grid points are defined on the rudder brackets and fin-box brackets. Thus, a virtual motion of the dependent nodes with respect to the independent ones can be implemented to simulate the rudder deflection per load case.

The application of MPCs to simulate the rudder deflection is of paramount importance, as it ensures the correct orientation and transmission of the resultant force in the actuator element. As the aerodynamic loads are computed for a deflected rudder state, the resultant force in the actuator would be oriented in the direction of the real actuator position required for the rudder deflection. Without the MPCs, the resultant force would not be aligned with the actuator element and thus the load transfer would be incorrect, as depicted in Figure 2.21.

This misalignment can significantly change the strains (thus stiffness) results for high rudder deflections, which can go up to 30°, due to the inaccurate load transmission and subsequently lower nodal forces in the VTP fin-box.

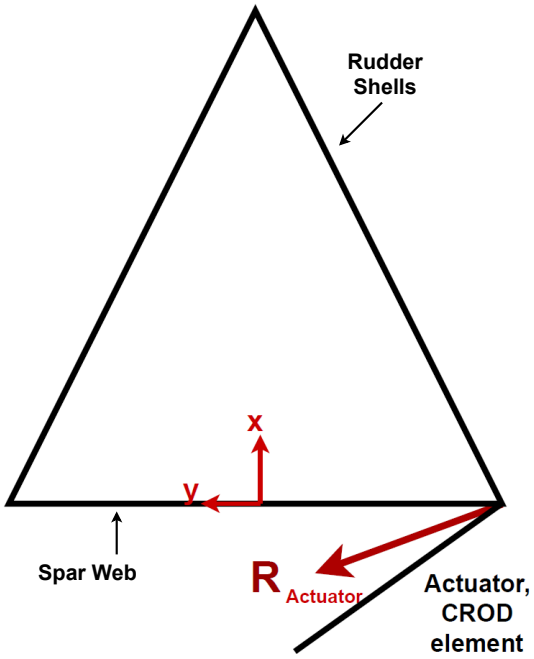

Figure 2.21: Misalignment of the Resultant Nodal Force at the Actuator Element in the Absence of the Virtual Deflection Viewed on a Simplified Rudder Shell Cross-section Sketch in the Rudder Coordinate System (Sandwich Core and Actuator Bracket are not Represented for Simplification Purposes)

While the SPCs constrain rotations around the x and y-axis, the MPCs provide the boundary conditions for the translational degrees of freedom at the rudder hinge lines. However, the implementation of MPCs has further implications on the reaction forces at the VTP fin-fuselage interface, discussed in the next subsection.

2.3.6 Load Factors

The load envelope values are reported as limit loads, which should be safely carried by the structure. However, the rudder has to be certified for ultimate load requirements as stated by CS.25 regulations [10], obtained by scaling the limit loads by a factor equal to 1.5. Due to the 1.5 factor, no additional safety factors are applied. Hence, the loads corresponding to Figure 2.10 are scaled by a factor of 1.5 during the FEM calculations.

As the rudder deflection is simulated through MPCs and not by analysing a FEM model with the rudder geometrically deflected, it has been observed that the reaction forces at the VTP-fuselage interface do not match the target values plotted in Figure 2.10. This is caused by the fact that during the MPC application, the loads remain perpendicular to the rudder surface, but the contributing rudder force in the y-direction is scaled by the cosine of the deflection angle, as depicted in Figure 2.22.

Thus, for the undeflected GFEM model, the fin-box aerodynamic nodal loads are scaled to match the target bending force and moment at the VTP root. The rudder aerodynamic loads are not scaled, as they are calculated initially to match the target hinge moment. Since the

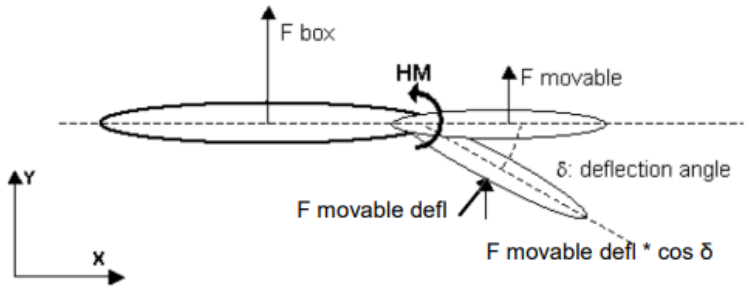

Figure 2.22: Box and Rudder Loads on the VTP Cross-section Geometry Sketch (Airbus Courtesy)

loads remain perpendicular to the rudder surface when the MPC is applied, the resultant hinge moment does not change.

The load factors that account for the virtual rudder deflection have to be applied to the fin aerodynamic loads, computed as one general factor per load case with Equation 2.1, where $M_{x,target}$ is the target bending moment retrieved from the load envelope illustrated in Figure 2.10, $M_{x,rudd}$ is the reaction moment at the VTP root due to rudder aerodynamic forces only (separate FEM simulations were conducted to obtain these values) and $M_{x,box}$ is the reaction bending moment due to fin-box aerodynamic loads.

$$f = \frac{M_{x,target} - M_{x,rudd}}{M_{x,box}} \tag{2.1}$$

2.3.7 Post-processing

The rudder design that has been presented throughout the chapter is the result of static calculations performed for the scaled ultimate load cases shown in Figure 2.10. The rudder structural performance is quantified and validated by the computation of reserve factors (RFs), based on experimentally determined strain allowables.

Composites are generally more prone to imperfections than metals due to the core sensitivity to impacts [45], temperature variations [18] and moisture ingression, even from manufacturing stages [6], [27] which are sometimes undetectable due to their relatively small size. However, their combined effect might entail a loss in load-carrying capabilities in time. To ensure the safe use of composite materials during the rudder design, their mechanical properties must include the influence of damages. While analytical methods have been developed to quantify the effect of damages on the structural performance, they are not able to accurately predict the composite behaviour in case of combined damages (such as the combined effect of debonding and porosities) [24], [35], [49], [34].

Hence, Airbus has experimentally determined a set of allowable strains by testing both damaged sandwich and monolithic specimens, containing different defects of different sizes, as stipulated by regulations (including delaminations, impact damages, burnt sandwich core, water ingression and disbonding). They enable validation of the FEM results through the computation of the reserve factor, expressed in Equation 3.1, with the principal strains $\varepsilon_x, \varepsilon_y$

and γ_{xy} extracted from the FEM analysis (in the material coordinate system defined in Figure 2.2). The engineering shear strain allowable $\gamma_{xy,allow}$ is 70% of the axial strain allowables ($\varepsilon_{x,allow} = \varepsilon_{y,allow}$), turning the (engineering) shear strains into an important check during the analysis, as changes in shear strain affect the reserve factor results the most due to the lower design allowable. The reserve factor formula is based on the strain failure criterion [8].

$$RF = \frac{1}{\sqrt{\left(\frac{\varepsilon_x}{\varepsilon_{x,allow}}\right)^2 + \left(\frac{\varepsilon_y}{\varepsilon_{y,allow}}\right)^2 + \left(\frac{\gamma_{xy}}{\gamma_{xy,allow}}\right)^2}} > 1 \tag{2.2}$$

The results of the test campaign undertaken to determine the strain allowables are representative for far-field strains in unnotched test specimens loaded in tension, compression and shear, tests being conducted for both individual and combined loading [7]. While this method is not explicitly a damage tolerance assessment, it incorporates experimentally determined damage tolerance considerations. Tests have been performed also to study the growth rate of these defects, the utilised strain allowables being 6 or 8 times smaller than the recorded failure values, and for this reason, further damage tolerance methods are not further pursued for the spar-box design. The fibre orientation of the specimens placed in the testing machines was varryed (e.g. compression tests were carried for specimens with 0° and 45° orientation of the fabric layer), eliminating the need to apply rotation matrices on the strain results yielded by the FEM simulation.

The strains were measured in the middle of the panels during the tests, recording far-field strains. Thus, a relatively coarse mesh with elements of an average size of 100 mm x 80 mm is used for the preliminary designs. The strain allowables would not be representative for elements of smaller sizes used in a GFEM, because if small, local damages are present in the structure, the rest of the components can safely redistribute the load. The determined strain allowables are valid for both sandwich and monolithic structures.

Chapter 3

Spar-box Concepts Generation

This chapter aims to detail the new rudder shell concept and explore the spar-box design possibilities that would enable the separation between the internal and the external loads.

Firstly, the sizing load cases are selected in section 3.1, to simplify the design process by identifying the real rudder sizing external loads. The design space with desired changes in the rudder shells, spar-box design requirements, allowables and constraints are presented in section 3.2.

Subsequently, section 3.3 describes the design principles that could enable the load separation, from which possible design concepts can be derived, exploring also the advantages of changing the actuator brackets' material to composite in section 3.4. Lastly, each spar-box concept and corresponding rudder design modifications are thoroughly described in section 3.5 and further subjected to a trade-off in the next chapter.

In the project's first iteration, thermoplastic CFRP composites will be utilised in the rudder shells, the current booster area being substituted with the spar-box, whose design principles are detailed in this chapter. This material choice ensures the rudder stiffness retention, given that the fibres are the main load carrier, rendering the new design more viable to be introduced in service without major changes to the VTP system.

Nonetheless, with the proven feasibility of a spar-box and a sizing methodology, the use of different sustainable materials can be explored for the rudder shell design.

3.1 Load Selection

In order to ease the design process and provide a preliminary design of the spar-box, only three relevant sizing load cases are selected, which correspond to the three corners seen on the load envelope contour depicted in Figure 3.1, at the VTP-fuselage interface (which is also the VTP root). Since the load levels and reserve factors are very similar, the mirrored loads are not considered. These cases provide the maximum rudder limit loading (the bending of the fin and the rudder hinge moment) that could occur during the aircraft's operational life,

covering any load level corresponding to the other cases, which entail lower loads, avoiding additional analysis steps that would not further influence the design of the rudder spar-box, in the form of lower reserve factors.

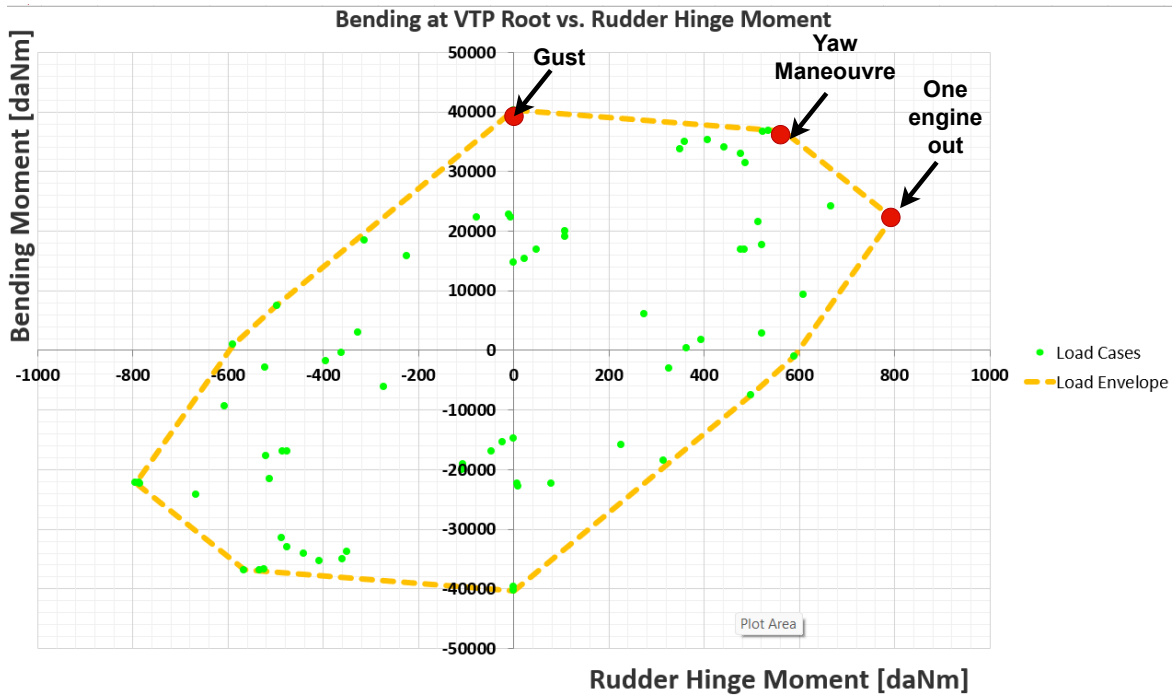

Figure 3.1: Selected Load Cases

The corners of the load envelope also correspond to three different operational conditions, the lateral gust having maximum bending moment at 0 rudder deflection, one engine out with maximum hinge moment, and a combination of relatively high bending and hinge moments during yaw manoeuvres. The selected load cases, their corresponding load ID and reaction moments are presented in Table 3.1.

LC Code	Load Case	Bending Mom. [kNm]	Hinge Mom. [kNm]	Rudder deflection [deg]
LC-01	Lateral Gust	400	0	0 °
LC-02	Yaw manoeuvre	380	6	7°
LC-03	One Engine Out	220	8	30°

Table 3.1: Selected Load Cases

However, even with three main load cases selected, there would be a total of 42 subcases. Their number can be further reduced, by disregarding the subcase with no actuator failure, as the entailed internal loading is equal to 0. With no additional internal load, the strain levels are relatively lower compared to the jamming cases, thus this subcase will be omitted, reducing the number of subcases to 36. Moreover, jamming in AC 2 leads to lower internal loading compared with AC 1 or AC 3 jamming, as the load could be taken evenly by AC

1 and AC 3. Hence, AC 2 jamming subcases can be disregarded, leading to a total of 24 sub-cases being evaluated. This number could be further reduced by only considering the jamming while retracting or extending, but both subcases are kept in order to identify the highest shear loading, even though it varies in the order of tens of micro-strains.

For the selected load cases, the smallest reserve factor of the rudder shells, 1.27, occurs in the sandwich ramp-down element above AC1 for the one engine out conditions (also highest rudder hinge moment) at -54°C with AC1 jammed while retracting, an aspect mainly influenced by the high shear strain, as shown in Table 3.2.

LC	$\frac{\varepsilon_{XX}}{\varepsilon_{XX,allow}}$	$\frac{\varepsilon_{YY}}{\varepsilon_{YY,allow}}$	$\frac{\gamma_{XY}}{\gamma_{XY,allow}}$	RF	Location
03-01-02	0.09	0.35	0.70	1.27	Ramp Above AC 1

Table 3.2: Original Rudder Shell Minimum Reserve Factor

Thus, it can be concluded that the hinge moment induces higher shear loads than the bending created by the aerodynamic loads. Moreover, the smallest reserve factors occur in the weakest area of the sandwich, the ramp-down, in the vicinity of the jammed actuator, as would be expected, also emphasising the load-carrying role of the 0° booster layers.

The fact that the reserve factor surpasses the unit value is not an over-design indicator, given that the structure is subjected to a certification process to enter operations. Additionally to the ultimate load factor (1.5), there is a margin required for further knock-down factors related to manufacturing to ensure the safety of the structure. However, applying such factors for the current re-design is not part of the thesis scope, as the manufacturing processes would be different for the new rudder concept and the thesis covers a spar-box concept feasibility, not a structure certification process.

Additionally, as stated in subsection 2.3.7, the strain allowables are very conservative, up to eight times lower than the recorded fracture load for panels containing defects (e.g. delaminations). Thus, the reserve factors of the shells obtained during the spar-box design optimisation are allowed to go as low as 1.01. With the selected load cases, no modifications on the loads and boundary conditions (NASTRAN LOAD, FORCE, MPC and SPC cards) are performed. The loads are applied to the VTP system as described in section 2.2.

3.2 Defining the Design Space

This section commences with the description of the desired changes in the rudder shells and the updated GFEM model in subsection 3.2.1. Next, the design requirements are defined in subsection 3.2.2, and the allowed changes and constraints during the spar-box design are presented in subsection 3.2.3 and subsection 3.2.4 respectively.

3.2.1 Desired Shell Changes and Updated FEM Model

Given the goal of the thesis to separate the structures that carry the system failure and aerodynamic loads, the shell reinforcements in the actuator area are removed, providing a

homogenous shell design (up to the rudder tip, where GFRP is used), that is sufficiently stiff to carry the aerodynamic loads without any reinforcement.

If the torsion box spar concept feasibility is proven, the next step would be to investigate the use of thermoplastic CFRP rudder shells, as they have comparable stiffness to the current thermoset shells. Due to this material choice, the alterations in the shell design would not lead to problems from an aeroelastic perspective, allowing the introduction of the sustainable rudder in service without major changes to the VTP system. The physical desired changes for the future recyclable CFRP rudder shells are enumerated below.

- **RUD-CHANGE-01:** The resin used in the rudder shell design is changed from thermoset to thermoplastic
- **RUD-CHANGE-02:** The 0° reinforcement layers are removed from the rudder shells
- **RUD-CHANGE-03:** The Nomex core with 48 kg/m^3 density, used only in the booster area, is substituted with a core density of 32 kg/m^3, leading to a uniform core density in the shells

Some of the changes have a direct impact on the FEM model, which has to be updated to match desired physical alterations. The resin change, stated in **RUD-CHANGE-01**, does not lead to a material card change, as the mechanical properties of the thermoplastic and thermoset resins are similar.

Considering that the use of carbon fibre would not change, which is the main load-carrying component in the composite, material cards do not have to be updated. Moreover, a specific new material has not yet been selected for the rudder shells, emphasizing the fact that the main purpose of the thesis is to study the feasibility of a spar-box design to carry system failure loads.

Conversely, the modifications stated in **RUD-CHANGE-02** and **RUD-CHANGE-03** are simply implemented by deleting the current property cards corresponding to the booster FEM elements. Instead, the already existing PCOMP properties without reinforcement (30 mm core of 32 kg/m^3 density with one 45° inner fabric layer and one 45° outer fabric layer) are assigned.

Since the shell material does not change in the current study, the original mesh size is retained throughout the entire thesis due to the strain allowables that were experimentally determined. This makes the use of the strain allowables characterizing the far-field strains of damaged fabric composites appropriate for the spar-box design validation, as explained in subsection 2.3.7.

The changes apply to both rudder shells, and the differences in FEM modelling between the current and unreinforced shells can be visualised in Figure 3.2 and Figure 3.3 for the left-hand side shell, where each element colour corresponds to a different PCOMP property. Additionally, it can be observed that the shell elements in the monolithic overhang area which are superimposed on the spar flanges elements (second row of elements from the leading edge) are homogenised as well since reinforcement layers were also present in that region.

The third row of rudder elements, which is the first row of elements corresponding to the sandwich structure, is modelled with a 15cm Nomex core thickness to simulate the ramp-down and the next row of elements is modelled with a 30cm core thickness and still one 0°

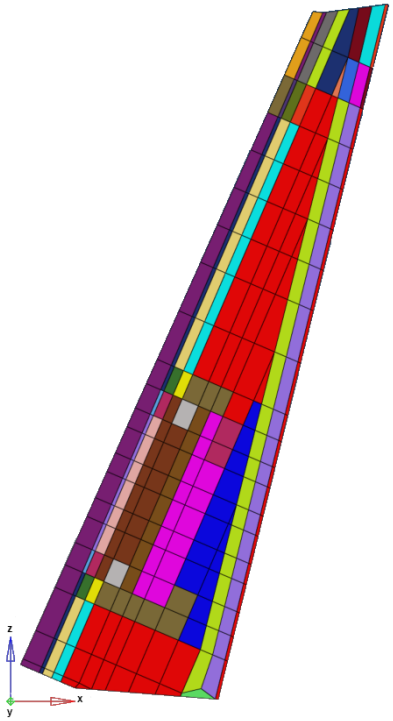

Figure 3.2: Properties of the Reinforced Shells

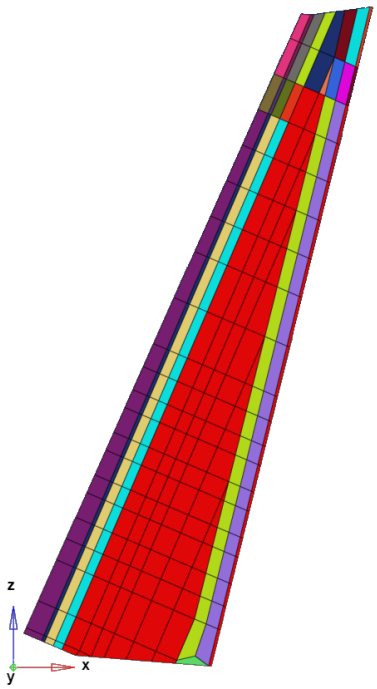

Figure 3.3: Properties of the Unreinforced Shells

layer. The following element rows depicted in red contain the 30 cm core thickness with one fabric layer of 45° on each side, representing the homogenised rudder shells.

The rudder shell properties further used in the FEM analyses are provided below, each colour being associated with a different PCOMP property, the legend being provided in Figure 3.4. The rudder shells are symmetric and the property designation is valid for the right-hand-side shell as well. The layup sequence per property is provided in Figure 3.5

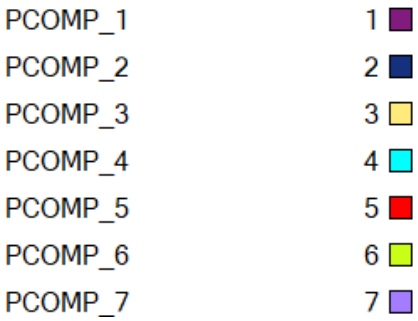

Figure 3.4: PCOMP Property Legend

Property	Sequence
PCOMP_1	$45°/0°/45°/0°/0°/45°/45°$
PCOMP_2	$[45°/0°/45°/0°]_s$
PCOMP_3	$45°/0°_2/15$ mm core$/0°_2/45°$
PCOMP_4	$45°//0°/30$ mm core$//0°/45°$
PCOMP_5	$45°/30$ mm core$/45°$
PCOMP_6	$45°/20$ mm core$/45°$
PCOMP_7	$45°/0°/10$ mm core$/0°_2/45°$

Figure 3.5: Layup Sequence per PCOPMP Property

Thus, Figure 3.3 also shows that for the first few tens of centimetres in the sandwich area, accounting for the third row of elements, the 0° layer continuing from the overhang monolithic area is kept in the updated model, to provide a smooth transition from the overhang to the sandwich area and provide the required skin thickness for riveting. It also becomes clear that

the current reinforcements extend span-wise beyond the actuator location, emphasizing the size of the affected area in case of actuator malfunctions.

With these changes performed on the rudder shell element properties, the minimum reserve factor with no actuator jamming is 1.06, occurring for one engine out loads (LC-03-00-02). However, once the actuator jamming loads are introduced, the minimum reserve factor becomes 0.55 (LC-03-01-02).

This comparison emphasises the external load-carrying capabilities of the unreinforced shells, and the exclusive contribution of the reinforcements in carrying the internal, system failure loads. Thus, the addition of the spar-box in the actuator area is a necessity to alleviate the loads in the shells in case of actuator jamming, and the design requirements derived for the spar-box design are further presented in the next subsection.

3.2.2 Requirements

Material or local geometry modifications can affect the stiffness, load path and load distribution within the rudder, which are important for the structural performance under static loads and for aeroelastic considerations. Moreover, these modifications also have an impact on the structural weight, which highly influences the aircraft's performance. Hence, several requirements can be derived for the spar-box design, as stated below, to ensure the concept viability.

- **REQ-01-DESIGN:** The minimum reserve factor of all rudder composite FEM elements shall be higher than 1
- **REQ-02-DESIGN:** The elastic eigenfrequencies shall not change more than 7%
- **REQ-03-DESIGN:** No new elastic modes shall be introduced in the structure
- **REQ-04-DESIGN:** The weight of the new rudder design shall not exceed by more than 15% (77 kg limit) the weight of the current rudder (67 kg)
- **REQ-05-DESIGN:** The new rudder structural elements shall not buckle under ultimate load

The first requirement, **REQ-01-DESIGN**, addresses the material damage tolerance considerations, the structural performance under static loads and the design validation of all rudder components, as thoroughly explained in subsection 2.3.7. The reserve factor is expressed again in Equation 3.1 for convenience, with the principal strains extracted from the FEM analysis. The engineering shear strain allowable $\varepsilon_{xy,allow}$ is 70% of the axial strain allowables ($\varepsilon_{x,allow} = \varepsilon_{y,allow}$), rendering the (engineering) shear strains the main target during the analysis.

$$RF = \frac{1}{\sqrt{\left(\frac{\varepsilon_x}{\varepsilon_{x,allow}}\right)^2 + \left(\frac{\varepsilon_y}{\varepsilon_{y,allow}}\right)^2 + \left(\frac{\gamma_{xy}}{\gamma_{xy,allow}}\right)^2}} > 1 \tag{3.1}$$

Composites are prone to imperfections, which are sometimes undetectable. In order to ensure structural safety, the materials must be able to sustain the pre-described loads including damages. Thus, the experimentally determined strain allowables, valid for both CFRP sandwich and monolithic composites, have been set at least 6 times smaller than the failure load of the tested panels containing damages (including delaminations, core burn, and disbonding areas).

The second requirement, **REQ-02-DESIGN**, addresses stiffness and weight changes that might lead to aeroelastic problems. The structural stiffness and weight have direct implications on natural frequencies and modes, which were finely tuned for the current rudder design to avoid aeroelastic and dynamic response problems.

After the static analysis, the second check that hints at the spar-box design feasibility is the modal analysis that computes the VTP eigenfrequencies and modes. Since the spar-box is a concept in the preliminary design phase, the maximum allowed change in the eigenfrequencies is 7%. A higher change in natural frequencies would indicate a clear design problem, but with a maximum initial variation of 7%, aeroelasticity-related problems that might occur at later detailed design phases can be corrected.

In addition to significant variations in eigenfrequencies, the introduction of new modes shall also be avoided, as stated in **REQ-03-DESIGN**, as this could also dramatically change the dynamic behaviour and response of the VTP to dynamic loads.

Weight is a driving factor in any aircraft subsystem change, as it plays a key role in defining the aircraft's operational performance. Given that the main aim of the project is to introduce the use of sustainable materials, a slight weight increase is allowed, as stated in **REQ-04-DESIGN**. As nowadays the reinforcement in the actuator area of both shells accounts for approximately 9 kg, the maximum allowed weight of the box shall be around 10.35 kg. However, the requirements target the overall rudder weight and not the spar-box alone, as different designs for the brackets or spar could be proposed, leading to further weight reductions.

Buckling in the rudder components (both sandwich and monolithic) is not allowed due to the certification nature of the Airbus single-aisle VTP, which must be able to carry the ultimate loads without buckling, an aspect incorporated in **REQ-05-DESIGN**. Throughout the thesis, the already existing structures, including the shells and the spar, will not be checked for buckling, as the chosen sandwich thickness (30 mm) and the spar thickness were proven experimentally by Airbus to ensure the buckling onset at higher loads than the ultimate ones.

In case the new spar-box structure buckles under ultimate load conditions, the load would be redistributed in the shells, which is not desired, given that the main purpose of the spar-box is to alleviate the loads in the rudder shells. **REQ-05-DESIGN** is a reflection of a general Airbus single-aisle rudder design requirement to avoid buckling under ultimate loads.

3.2.3 Allowed changes

In order to accommodate an efficient spar-box incorporation in the rudder architecture, some other rudder modifications might be required. Below, the overall allowed changes with respect to the current design are enumerated. As long as the requirements stated above are met, the following changes can be performed.

- **DES-ALLOW-01:** The sandwich ramp-down can be shifted aftwards

- **DES-ALLOW-02:** The rudder properties can locally vary span-wise
- **DES-ALLOW-03:** The actuator fittings material can be changed
- **DES-ALLOW-04:** The actuator fittings design can be changed
- **DES-ALLOW-05:** Dividing the spar in multiple components is allowed
- **DES-ALLOW-06:** The spar thickness can be changed in the area of the spar-box

Depending on the design philosophy, the spar-box might be connected to the rudder shells at different locations. However, due to moisture ingression problems and the sensitivity of the sandwich structure to damage, no holes and fasteners should be present in the sandwich area [37], [26], [11]. For this reason, the monolithic overhang area might be extended aft the spar web, moving the ramp-down up-wards, as asserted in **DES-ALLOW-01**.

The shells can be manufactured as one piece from the beginning, or in different blocks, thus the properties might be different span-wise, as stated in **DES-ALLOW-02**. This is of importance because, for instance, the ramp-down can be moved upwards only locally, in the actuator area.

As the actuator loads are introduced in the structure through the brackets, their material and design are allowed to change if this could increase the efficiency of the spar-box, as stated in **DES-ALLOW-03** and **DES-ALLOW-04**. Hence, a composite bracket design, for instance, can be investigated in an attempt to efficiently introduce the loads in the spar-box design and further reduce the overall weight. Note that since the hinge brackets do not constitute a direct internal load introduction path, their material will stay metallic.

Depending on the design solutions, the rudder spar web might have to be manufactured in multiple components, which is allowed according to **DES-ALLOW-05**. Moreover, stress calculations might indicate the need to increase or reduce the thickness of the current spar, which can be done according to **DES-ALLOW-06**.

3.2.4 Constraints

There are also default limitations to the changes that can be performed while introducing the spar-box design, and some of the constraints enunciated below apply to the above-mentioned allowables.

- **DES-CONSTR-01:** The hinge line and actuation line locations are fixed
- **DES-CONSTR-02:** The width of the spar and rudder shell planform dimensions are fixed
- **DES-CONSTR-03:** The used material for the spar-box is fabric
- **DES-CONSTR-04:** Regarding the use of fabrics, only layer orientations of 0° and 45° can be used
- **DES-CONSTR-05:** If the ramp-down is moved, the resulting monolithic area shall not buckle

Regardless of the aircraft variant, the rudders of the Single Aisle family are interchangeable. For this reason, the actuator and hinge lines location is contained in all directions **DES-CONSTR-01**, as new rudder designs could substitute rudders in past aircraft. The rudder planform geometry is mainly dictated by aerodynamic, control and stability requirements, and they are not subjected to change during the structural design, as stated by **DES-CONSTR-02**.

In order to ease the design process, it is desired to design the spar-box with the currently used materials. Since no UD laminates are used in the rudder structural components, the spar-box shall be initially designed with fabric materials, as stated in **DES-CONSTR-03**. However, this is not a hard constraint. If subsequent considerations prove the benefits of using UD, their use can be investigated.

Additionally, from both manufacturing and calculation considerations, it is more efficient to use 0° and ±45° fibre orientations only as stated in **DES-CONSTR-04**, since they correspond to the principal axial and shear axis respectively. Moving the ramp-down upwards is limited by buckling constraints. While the introduction of additional stiffeners is not desired due to the weight increase, the buckling performance might be improved by increasing the thickness. **DES-CONSTR-05** also comes as a constraint for the boundary conditions.

3.2.5 Composite design rules

While determining the layer sequence during the spar-box design, the design rules stated below should be accounted for [25], [31].

- If both 0° and 45° orientations are used, no more than 4 plies with the same orientation shall be stacked consecutively
- 45° plies should be placed at the outer skin to avoid delaminations
- Symmetric layups shall be used to avoid in-plane-out-of-plane load coupling
- Balanced layers shall be used to avoid in-plane-shear load coupling

3.3 Spar-box Design Philosophies

In this section, different design philosophies that would enable the redirection of the internal loads inside the spar-box are analysed in subsection 3.3.1, generating different spar-box concepts, later subjected to a trade-off. The spar-box design and FEM model used in the subsequent trade-off are described in subsection 3.3.2.

3.3.1 Design Philosophies

The purpose of the spar-box is to take up the torsional loads induced in the case of actuator malfunction and not redirect them in the rudder shells. While investigating answers on how to achieve this goal, it was concluded that the load separation can be obtained in two different

ways: by locally increasing the torsional stiffness with the addition of the spar-box or by interface (and implicitly load) decoupling, by removing the spar-shell connection, while still enclosing the spar in the area of the actuators by a box to carry the torsional jamming loads. The two design principles are enunciated below.

- **Principle 1:** Locally increasing the torsional stiffness by attaching a box to the rudder spar in the area of the actuators while keeping the original rudder shell-spar riveted interface (the box would not be attached to the spar throughout the entire rudder span)
- **Principle 2:** Structurally decoupling the spar-box from the shells by removing the riveted interface (between the spar flange and the monolithic overhang area of the shells) in the area of the actuators

By analysing the two principle statements, it becomes clear that the connection of the spar-box to the shells is of paramount importance in achieving the load separation, and can be implemented in two different ways. With principle 1, the shells still provide a load path for the jamming loads due to the riveted interface between the spar, where the actuator brackets are attached, and the shells, but the magnitude of the load entering the shells is reduced by the torsionally stiff spar-box. By removing the riveted connection as stated by principle 2, the spar-box and the shells are structurally decoupled and the jamming loads do not have a path to the shells.

In a second analysis step regarding the goal of decoupling the internal and external rudder loads, an efficient connection between the spar-box and actuator brackets should be considered, given that the internal loads are introduced in the rudder via the actuator brackets. A direct connection of the actuator brackets to the spar-box could lead the jamming loads in the box more effectively. Hence, to guide the actuator loads in the spar-box, it is desired to connect the actuator brackets to the roof of the box.

The two principles would correspond to two different spar-box concepts. However, since the brackets are to be connected to the box roof, there might be a problem regarding material compatibility. Given that the spar-box would be manufactured with composites, it could be easier to connect composite brackets to the spar-box. On the other hand, retaining the metallic design of the actuator brackets would imply fewer changes performed on the current rudder design, keeping in mind that metallic-composite connections are prone to galvanic corrosion and require additional insulating material.

Hence, the bracket-box connection can be done via a monolithic web in the case of composite brackets or a truss structure in the case of metallic brackets. Thus, three different concepts will explore the implementation of the two design principles for load decoupling and the two different actuator bracket materials: the two principles implemented for composite actuator brackets design and principle 1 implemented for metallic actuator design.

When considering the first design philosophy, it is known that the maximum shear stress (and implicitly strain) for a closed structure is dependent on the enclosed area and thickness, as stated in Equation 3.2, where T is the applied torque, A is the enclosed area, τ is the shear stress and t is the shell thickness.

$$\tau_{max} = \frac{T}{2A_{encl}t} \tag{3.2}$$

Inevitably, the rudder shells enclose a bigger area than the spar-box. Consequently, the rudder shell structure possesses a higher torsional stiffness, and part of the internal loads will be introduced in the shells. However, in the absence of the booster area, the load levels lead to reserve factors below 1, loads which can be alleviated by locally increasing the torsional stiffness in the actuator region.

As closed structures are torsionally the stiffest geometry, the shell loads can be alleviated with the addition of the spar-box. In this case, the spar flanges would provide the interface for the rudder shells and spar-box connection at span-wise locations between the actuator brackets, as depicted in Figure 3.6.

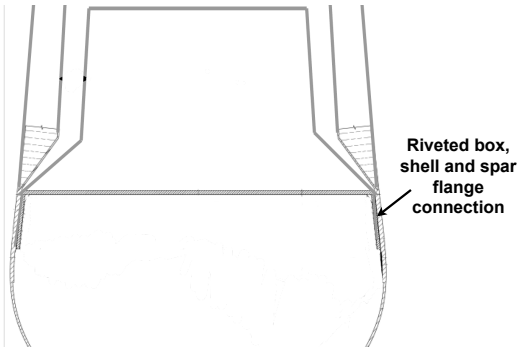

Figure 3.6: Spar-box Integation in the Rudder Design. Geometry in the x-y Plane Representative at Locations Between the Actuator Brackets

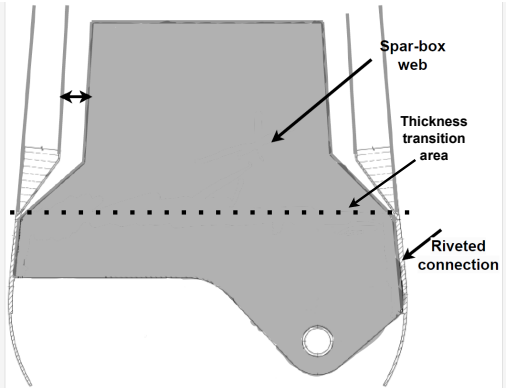

Figure 3.7: Spar-box Integration in the Rudder Design at the Actuator Brackets Locations in the x-y Plane by Extending the Bracket

By connecting the brackets to the spar-box roof, it is deemed that the internal loads would be further introduced in the spar-box and not rudder shells. This assumption is computationally checked in the subsequent chapter via FEM simulations. The actuator bracket integration in the spar-box design via a composite web is illustrated in Figure 3.7.

The actuator brackets and the web could be manufactured as one piece, but it is possible that two components would require different thicknesses. This design is similar to the fin lug (the VTP fin connection to the fuselage) transition to the fin skin, with a thickness ratio of 5:1 lug-skin.

Conversely, the second principle makes use of interface disconnection to guide the internal loads in the box. The de-coupled concept relies on the fact that the internal loads can not reach the shells from the spar-box if the two components are not connected, as shown in Figure 3.8. Hence, the spar has to be split into different components and the spar-box area is not joined to the shells by means of riveting.

However, to ensure the transfer of the actuation load under normal circumstances when the rudder has to be deflected, one connection point is required. Thus, the actuation load would be transferred through a shear joint only. As no rivetting is allowed in the sandwich area, the

ramp-down has to be moved aftwards in the area of the actuators, to provide a monolithic interface for the shear joint as illustrated in Figure 3.9.

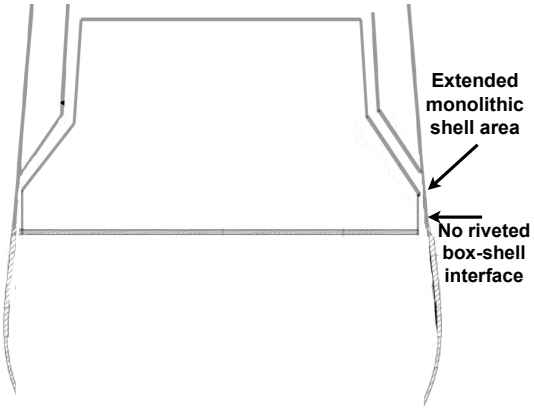

Figure 3.8: Profile View of the Decoupled Spar-box Concept at the location Between Actuator Brackets

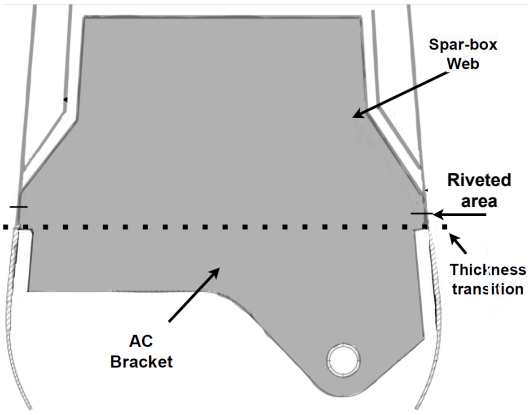

Figure 3.9: Profile View of the Decoupled Spar-box Concept at the location of AC 2

The third concept incorporates the first design philosophy with the current metallic actuator bracket design retention. Compared to the first concept, the actuator brackets are connected to the box via a truss structure, as shown in Figure 3.10. Thus, the connection of the box to the spar depicted in Figure 3.7 is valid for the truss box concept as well.

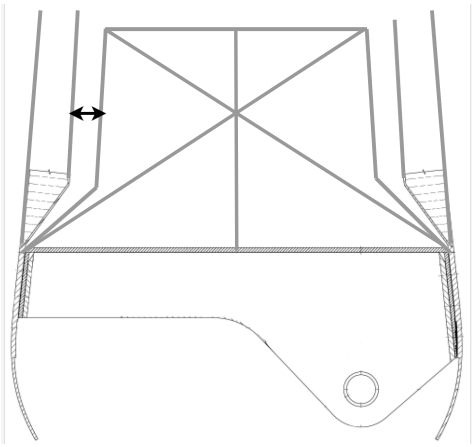

Figure 3.10: View in the x-y Plane at Actuator Bracket Location of the Truss Spar-box Concept

With three proposed concepts, a trade-off is performed to identify the best design philosophy, the bracket material and the feasibility of each concept. The concepts have different advantages and disadvantages, and the trade-off outcome could also indicate that more than one design is feasible. Before the trade-off presentation, the implications of each concept on the overall rudder design are further described in the upcoming sections.

3.3.2 General Spar-box Modelling

In order to conduct an unbiased trade-off for the three concepts, the spar-box is given a specific preliminary design used in the trade-off calculations. The spar-box FEM model presented in this subsection is used for the analysis of all three spar-box concepts during the trade-off. This ensures an objective assessment and comparison of the design principles, identifying the most effective design philosophy and actuator bracket material. The FEM model of the spar-box is created in a FEM pre-processing dedicated software, Hypermesh.

Moreover, the spar-box mesh elements have the same dimensions as the other rudder components (on average 100 mm x 80 mm). This enables the use of the allowables representing the far-field strains for damaged composites, as thoroughly explained in subsection 2.3.7 and ensures a consistent mesh size of the GFEM.

The initial spar-box mesh comprises a total of 154 CQUAD4 elements and 6 CTRIA3 elements, two per spar-box web at the top, due to their trapezoidal shape. The general box shape and its FEM meshing is depicted in Figure 3.11 (the webs connecting the actuator brackets to the box top substituted with a truss structure for concept C and the actuator bracket material change from metallic to composite is treated in section 3.4).

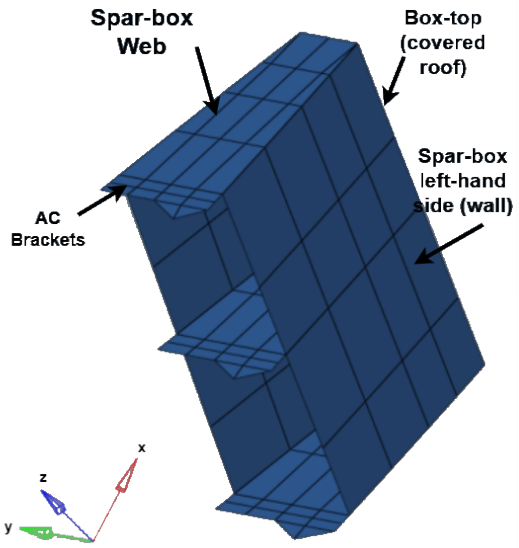

Figure 3.11: General Spar-box FEM Modell and Design Displayed in the Global Coordinate System with Spar-box Components

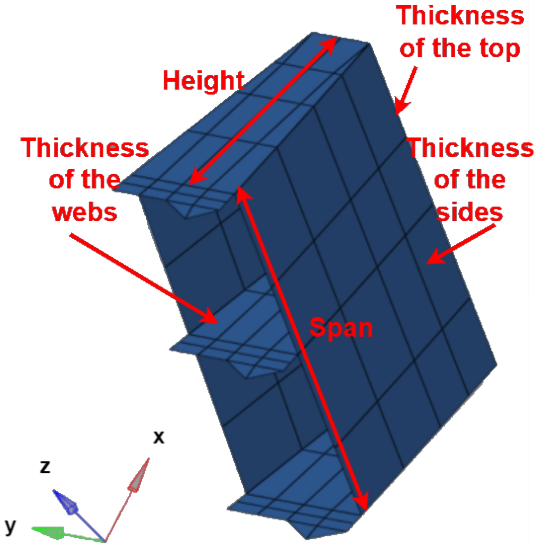

Figure 3.12: General Spar-box FEM Modell and Design Displayed in the Global Coordinate System with Spar-box Variables

The spar-box variables are: box span (length in the z-axis), box height (dimension in the x-axis), face sheets, roof and webs individual thicknesses and layup sequences. The cross-sectional shape is also a variable, but given the limitation on the enclosed area which has to be maximised, only the possibility of curving the box is explored, as the boundaries created by the shell geometry restrict the profile of the spar-box. The variables are indicated in Figure 3.12.

For initial calculations during the trade-off, the box encloses the same width as the shells

in order to maximise the enclosed area. The actual geometry (accounting for the 30 mm thickness of the sandwich core and clearance between the rudder shell and the spar-box) will be revised in the detailed design phase, based also on the observed maximum displacements of the shells and spar-box obtained from the static simulations. By designing the box geometry coincident with the rudder shell geometry, the required clearance between the shells and the spar box can be determined based on the resulting displacements (for instance, if the spar-box has a higher local displacement that interferes with the geometry of the shells, it would be considered in the optimised modelling).

Moreover, since the box is designed to take up the actuator jamming loads and includes the webs connecting the actuator brackets to the roof, the spar box spans between the upper and lower actuator brackets only. The current reinforcements span-wise extend beyond the actuator location, but the need to extend the span of the spar box will be investigated in later stages. As the box is a substitute for the current booster area, for the initial design, the height of the spar box matches the length in the x-axis of the current reinforcement.

For the trade-off, the layup sequence and thickness of the spar web (3.5 mm) which represents the bottom part of the spar-box is not changed. A relatively high thickness of roughly 5 mm is assigned to the spar-box components in the initial design used during the trade-off in order to avoid buckling problems, based on engineering judgment. Further spar-box design optimisation will investigate the possibility of removing layers and reducing the thickness, as this parameter also plays a role in shear flow distribution.

The final thickness and subsequently the layup sequence of the spar-box variables will be checked for buckling in the spar-box optimisation stage only because the trade-off is aimed at investigating the feasibility of the concepts, not at optimising the structure for weight minimisation. Since the same spar-box design is used, it will not generate weight differences between concepts.

The layup sequence (modelled with the PCOMP card in the FEM model) and the thickness overview of the spar-box elements used for the trade-off is given in Table 3.3, noting that the original spar web layup is retained and unmodified. The argumentation for layup choices is provided below.

Region	Layup	Thickness [mm]
Walls	$[45^\circ_3/0^\circ_2/45^\circ_2]_s$	4.9
Roof	$[[45^\circ_3/0^\circ_2/45^\circ_2]_s$	4.9
Webs	$[[45°/0^\circ_3/45°/0^\circ_2]_s$	4.9
Spar Web	$[0^\circ_2/45°/0^\circ_2]_s$	3.5

Table 3.3: Spar-box Component Layup Sequence and Thickness Summary

As the webs connecting the actuator brackets and the box top should introduce the actuator loads (that mainly act on the x-axis, perpendicular to the spar web) in the spar-box, the sequence is mainly 0°, with the introduction of a few 45° layers as imposed by the composite design rules. The side walls and the box top would take up the shear loads resulting from the actuator jamming, thus mainly 45° layers are used in these areas.

The composite bracket design, including the thickness and layup choice, will be treated separately in the subsequent section. Except the webs which are replaced by a truss structure for the metallic bracket concept, the properties presented in Table 3.3 are valid for all three spar-box concepts FEM model used during the trade-off process.

The peculiarities of each concept are further described. The next subsection presents the composite AC brackets design, as they are part of the box design in the case of concepts A and B.

3.4 Metallic to Composite Bracket Conversion

This section describes the actuator material change from metallic to composite, with the overall design process presented in subsection 3.4.1. A comparison aimed to investigate whether local fibre tailoring, even though harder to achieve in manufacturing, makes the design more efficient, leads to an analysis with quasi-isotropic layers in some regions of the brackets in subsection 3.4.2 and another analysis with homogeneous layer orientation in subsection 3.4.3. The final composite actuator bracket design is presented in subsection 3.4.4.

3.4.1 Design Process

A change from metallic to (monolithic) composite actuators represents an important step in the box-spar design, given the intention to guide the system loads in the spar-box by connecting the actuator brackets to the roof of the box. The bracket material change is incorporated in concepts A and B, concept C still exploring the possibility of retaining the metallic AC bracket design.

The design process of the composite brackets, which will be further utilised in the concept trade-off, is further described, noting that the geometrical shape of the brackets (both physical and FEM model) is not changed.

The original FEM model of the metallic brackets is divided into three areas with different properties, differing in the assigned thickness, as depicted in Figure 3.13, a feature retained in the composite bracket design process. As previously described, in reality, the brackets have two flanges, hence the thickness assigned in the 2D FEM model is the thickness of the two flanges combined.

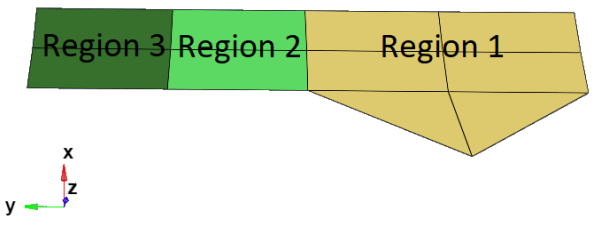

Figure 3.13: Actuator Brackets FEM Model. Different Colours Correspond to different Thicknesses

During the bracket transition to composite materials, two features have to be determined, noting the use of fabrics in the initial design: the thickness and the layup sequence. These

features are mainly driven by the load introduced by the actuators, which provide the reaction force when the rudder is deflected for the hinge moment balance or introduce internal loads in the case of force-fighting actuators failure scenario.

However, determining the layup sequence without knowing the target thickness represents a rather difficult task. By initially using the PSHELL property (which only needs the overall laminate property and not the individual properties of each layer) to model the brackets, the flange thickness can be determined first, as the PSHELL property card only requires membrane and bending stiffness.

Due to the use of fabric (with $E_{11} = E_{22}$) and fibre orientation limitations (0° and 45°), laminate target properties are rather easy to determine, irrespective of the laminate thickness, using the lamina properties in TABLE. In the case of quasi-isotropic layups, with 45° on the outer layers and 0° in the middle (to account for the design rules), the axial stiffness is equal to 47 GPa and shear stiffness is 17.86 GPa.

In case the fibre orientation is mainly 0°, the axial properties are similar to the fabric properties, with the stiffness roughly equal to 58 GPa, but lower shear stiffness, around 1 GPa. Thus, it can be seen that the fabric composite brackets can not attain the same stiffness as the current metallic ones (aluminium E-modulus is 71GPa) due to the use of fabrics and a higher thickness for composite might be required.

A first estimate of the thickness can be computed with the target stiffness known. Subsequently, PCOMP properties can be used, as with a target thickness and composite design rules, the layup sequence is easier to determine. The bracket design process is depicted in Figure 3.14.

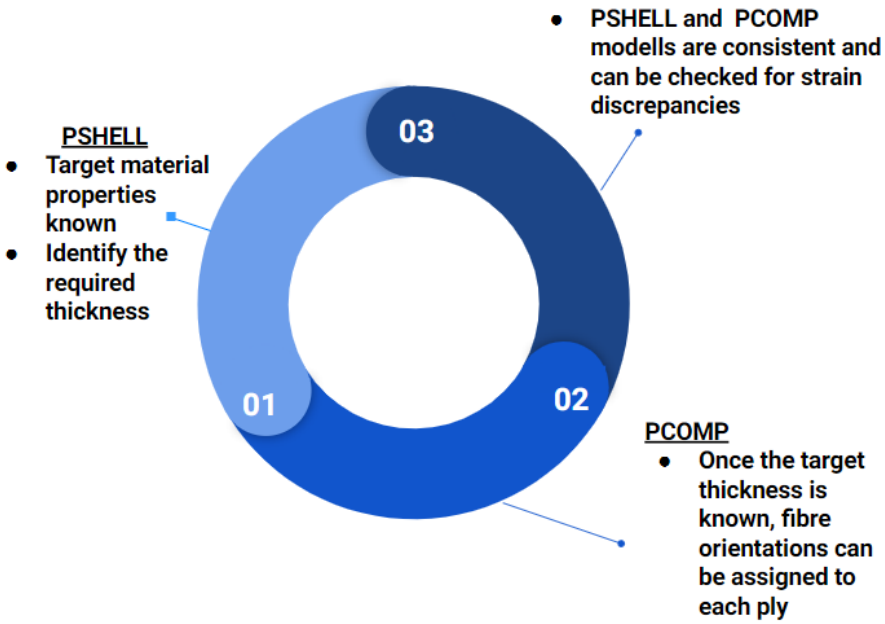

Figure 3.14: Actuator Brackets Material Change Process

Moreover, a sizing criterion has to be formulated for the initial design. If the original modelling of the reinforced shell is considered, due to the bracket material changing from metallic to

composite, it is expected that the individual strain values in the three directions might change. However, the value of the minimum shell reserve factor is the important one.

Due to the material change to fabric, it can not be expected to perfectly match the strains in all directions, thus the initial composite bracket design is accepted if the subsequent reserve factor does not change more than 5% for the critical load case and 7% for the other load cases. This is allowed because of the design margin provided by the original minimum reserve factor, which is 1.27.

As a starting point, the bracket thicknesses will not be changed compared to the metallic brackets, but they are expressed as a multiple of 0.35. If a change higher than 7% is observed in the reserve factors (or 5% for the critical load case), the bracket thickness is further increased.

Even though the actuator is placed at an angle, it mainly provides and introduces local loads in the x-direction. Thus, the yellow area has the main fabric orientation in 0°. Since the loads are transmitted globally as shear, the other two properties with lower thickness would be quasi-isotropic 0°/45°.

However, when determining the sequence manufacturing also has to be taken into account. Having different layer sequences in different regions of the bracket is not easy to manufacture. Moreover, the spar-box rib layers that connect the brackets with the box roof are also mainly 0° oriented. Hence, having 0 as the main orientation is better for the overall bracket from a manufacturing point of view.

Since it can not be predicted if the local tailoring of the actuator brackets would entail benefits for the rudder shell strains, 2 simulations are performed: one for quasi-static layers in the brackets and one for mainly 0°.

3.4.2 Quasi-isotropic Layup in Regions 2 and 3

The MAT1 material card entries for both membrane and bending properties used in the PSHELL property used in the brackets design are given in Table 3.4. Even though the material is orthotropic, the laminate is symmetric and the target material stiffness is known.

AC area	$E_m[GPa]$	$G_m[GPa]$	$E_b[GPa]$	$G_b[GPa]$	$\nu_{12,m}$	$\nu_{12,b}$	Thick. [mm]
Region 1	57	10	54	10	.18	.18	22.4
Region 2	47	18	45	18	0.3	0.3	15.4
Region 3	47	18	45	18	0.3	0.3	9.8

Table 3.4: Material Property Summary for PSHELL Card

Using the MAT2 material card for orthotropic materials would not improve the results and would make the design process more difficult since the MAT2 card requires ABD matrix predictions. Moreover, the results are not used to investigate the bracket reserve factors but to predict the effect of the material change on the rudder shells.

The maximum change for the minimum shell reserve factor between the original and PSHELL AC bracket modelling is 4%, as reported in Table 3.5, and it does not occur for the sizing

load case of the original rudder modelling. It is recorded for the yaw manoeuvre with AC1 jammed at $-54°$C LC-02-01-02, and, as expected, the highest difference is observed in the shear strain.

Bracket Mat.	LC	$\frac{\varepsilon_{XX}}{\varepsilon_{XX,allow}}$	$\frac{\varepsilon_{YY}}{\varepsilon_{YY,allow}}$	$\frac{\gamma_{XY}}{\gamma_{XY,allow}}$	RF	Max Δ	Location
Metallic	02-01-02	0.13	0.27	0.70	1.31	-	Ramp Above AC1
CFRP	02-01-02	0.12	0.29	0.73	1.26	4%	Ramp Above AC1

Table 3.5: Rudder Shell Minimum Reserve Factor for PSHELL Bracket Modelling

The element location of maximum strains in the rudder shells and AC brackets does not change. The location and values of the strain and von Mises stress distribution in the metallic hinge arm brackets (BR) also do not modify. Since the PSHELL bracket modelling met the set design criterion, a simulation with PCOMP modelling is also performed. It is expected that PSHELL is slightly stiffer than PCOMP due to the inaccurate material stiffness approximation in the PSHELL modelling. The PCOMP properties are given in Table 3.6, with the use of the MAT8 material card.

Bracket region	Layup	Thickness [mm]
Region 1	$[[45/0_4]_2/45/0_3/[45/0_4]_3/45/0_2]_s$	22.4
Region 2	$[45/0]_{22s}$	15.4
Region 3	$[45/0]_{14s}$	9.8

Table 3.6: PCOMP Properties of the AC Brackets per Region

The minimum shell reserve factor results corresponding to the PCOMP AC bracket modelling are given in Table 3.7. With both PSHELL and PCOMP properties, the value and location of the highest strains in the metallic hinge arm brackets do not change.

Bracket Mat.	$\frac{\varepsilon_{XX}}{\varepsilon_{XX,allow}}$	$\frac{\varepsilon_{YY}}{\varepsilon_{YY,allow}}$	$\frac{\gamma_{XY}}{\gamma_{XY,allow}}$	RF	Max Δ	Location
Metallic	0.13	0.27	0.70	1.31	-	Ramp Above AC1
CFRP PSHELL	0.12	0.29	0.73	1.26	4%	Ramp Above AC1
CFRP PCOMP	0.12	0.29	0.74	1.24	5.6%	Ramp Above AC1

Table 3.7: Rudder Shell Minimum reserve factor for load case LC-02-01-02 for Different AC Bracket Modelling

The results show, as expected, that the composite AC bracket design entails lower reserve factors in the rudder shells compared to the metallic brackets design due to overall slightly lower material stiffness, but the change is less than 5% for critical load case and less than 7% for the other load cases (5.6%) and that the difference between the shell minimum reserve factors obtained with the PSHELL and PCOMP bracket modelling is also not big, 1.6%.

3.4.3 Mainly 0° Layup in Regions 2 and 3

The MAT1 material card entries for the PSHELL property used in the brackets design are given in Table 3.8.

AC area	$E_m[GPa]$	$G_m[GPa]$	$E_b[GPa]$	$G_b[GPa]$	$\nu_{12,m}$	$\nu_{12,b}$	Thick. [mm]
Region 1	57	10	54	10	.18	.18	22.4
Region 2	57	10	54	10	.18	.18	15.4
Region 3	57	10	54	10	.18	.18	9.8

Table 3.8: PSHELL Property Summary

The maximum change in shell minimum reserve factor between the original and PSHELL AC bracket modelling according to in Table 3.9 is 3.1% and it does not occur for the most critical load case (the load case with the highest shear strain). The load case for which the highest difference in reserve factor is observed is LC-02-01-02, which is the yaw manoeuvre with AC1 jammed at −54°C with left-hand side deflection (retracting).

Bracket Mat.	$\frac{\varepsilon_{XX}}{\varepsilon_{XX,allow}}$	$\frac{\varepsilon_{YY}}{\varepsilon_{YY,allow}}$	$\frac{\gamma_{XY}}{\gamma_{XY,allow}}$	RF	Max Δ	Location
Metallic	0.13	0.27	0.70	1.31	-	Ramp Above AC1
CFRP	0.12	0.29	0.72	1.27	3.1%	Ramp Above AC1

Table 3.9: PSHELL Results for Maximum RF Change for LC 02-01-02

For PSHELL AC bracket modelling, the location of maximum strains in the rudder shells and brackets does not alter. The strain and von Mises stress distribution and magnitude do not modify in the metallic hinge arm brackets, thus a static simulation with PCOMP bracket modelling is also run. The PCOMP equivalent version with which the simulation is carried is given in Table 3.10, with the use of the MAT8 material card.

Bracket region	Layup	Thickness [mm]
Region 1	$[[45/0_4]_2/45/0_3/[45/0_4]_3/45/0_2]_s$	22.4
Region 2	$[[45/0_3]_4/[45/0_2]_2]_s$	15.4
Region 3	$[[45/0_3]_2/[45/0_2]_2]_s$	9.8

Table 3.10: PCOMP Properties of the AC Brackets per Region

The results regarding the rudder shell minimum reserve factor corresponding to the PCOMP AC bracket modelling are given in Table 3.11, for the load case with the highest change in minimum shell reserve factor, which does not change compared to the previous simulations.

The results show, as expected, that the composite AC bracket design entails lower reserve factors in the rudder shells compared to the metallic brackets design due to overall slightly lower material stiffness, but the change is less than 5% for critical load case and less than 7%

Bracket Material	$\frac{\varepsilon_{XX}}{\varepsilon_{XX,allow}}$	$\frac{\varepsilon_{YY}}{\varepsilon_{YY,allow}}$	$\frac{\gamma_{XY}}{\gamma_{XY,allow}}$	RF	Max Δ	Location
Metallic	0.13	0.27	0.70	1.31	-	Ramp Above AC1
CFRP PSHELL	0.12	0.29	0.72	1.27	3.1%	Ramp Above AC1
CFRP PCOMP	0.12	0.29	0.74	1.24	5.6%	Ramp Above AC1

Table 3.11: Rudder Shell Minimum Reserve Factor Summary for LC-02-01-02

for the other load cases (5.6%) and that the difference between the shell minimum reserve factors obtained with the PSHELL and PCOMP bracket modelling is also not big, 2.4%.

For both PSHELL and PCOMP composite bracket modelling, the strains, von Mises stress and the location of the maximum strain in the metallic hinge arm brackets did not change.

An important remark is represented by the fact that the choice of the layup stacking sequence in regions 2 and 3 of the AC brackets did not produce different results. This implies that minor, local changes in the AC brackets (such as small thickness variations and limited layer orientation alterations) do not impact the overall GFEM stiffness.

3.4.4 Final Composite Bracket Design

The static simulation results indicate that the choice of fibre orientation in regions 2 and 3 of the actuator brackets does not lead to changes in the minimum reserve factors of the rudder shell. Given the manufacturing ease to simply have ply drops from region 1 to region 2 to vary the thickness, it is opted for a layup that is dominated by the 0° orientation in regions 2 and 3.

As previously mentioned, the highest difference in the minimum reserve factor of the shells does not occur for the critical load case of the original rudder. For comparison, the minimum reserve factors for the original design critical load case (one engine out with retracting AC 1 jamming at -54° LC 03-01-02) are summarised in Table 3.12, noting that for the composite brackets, the shell minimum reserve factors increase compared to the results obtained with metallic brackets. The relative difference in shell minimum reserve factor for the metallic and PCOMOP modelling of the composite brackets is 3.1% (thus, below 5% for the original sizing load case).

AC Bracket Material	$\frac{\varepsilon_{XX}}{\varepsilon_{XX,allow}}$	$\frac{\varepsilon_{YY}}{\varepsilon_{YY,allow}}$	$\frac{\gamma_{XY}}{\gamma_{XY,allow}}$	RF	Location
Metallic	0.09	0.35	0.70	1.27	Ramp Above AC1
CFRP PSHELL	0.09	0.33	0.68	1.31	Ramp Above AC1
CFRP PCOMP	0.12	0.33	0.68	1.31	Ramp Above AC1

Table 3.12: Rudder Shell Minimum Reserve Factor Summary for LC-03-01-02

The shear strain distribution in the rudder shells corresponding to the load case for which the maximum difference in reserve factor was observed (AC1 retracting jamming during yaw manoeuvres at -54 °C LC-02-01-02) is shown in Figure 3.15 for the FEM modelling of original

metallic brackets, PSHELL and PCOMP modelling of the composite bracket. It can be seen that the strain distribution is not affected by the change in bracket material.

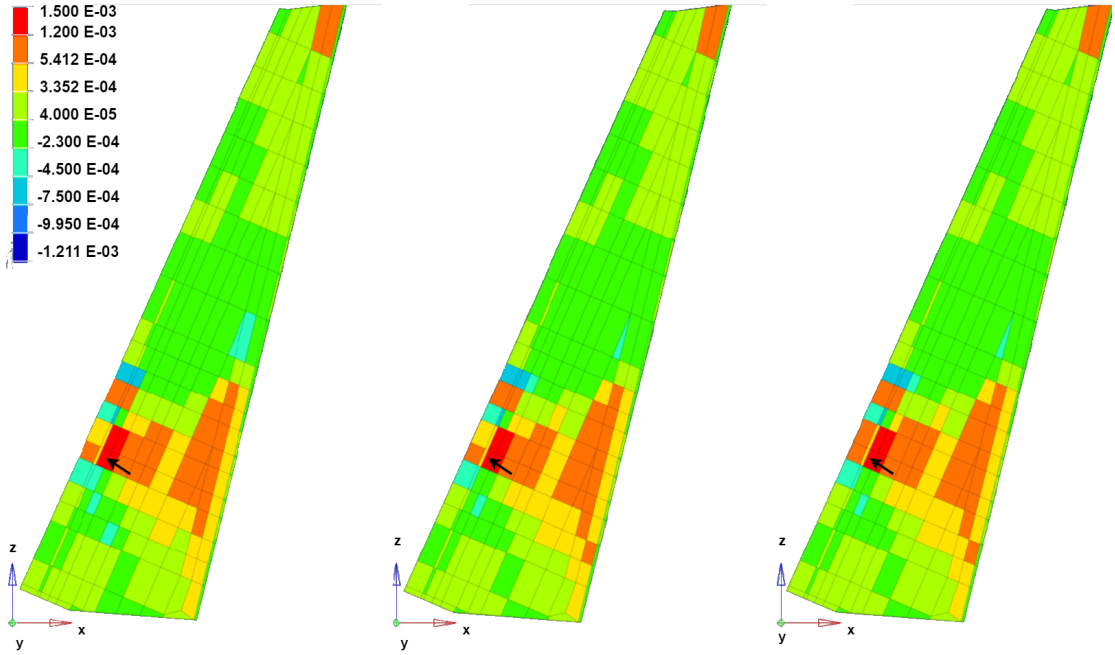

Figure 3.15: Shear Strain Distribution Comparison in the Original Rudder Shells (Figure 3.2) obtained by running a static analysis of the GFEM (Figure 2.12) for the sizing load case (minimum RF) LC 02-01-02. From left to right, the strains are plotted for the results obtained with the original metallic brackets, the composite brackets modelled with PSHELL properties and the composite brackets modelled with PCOMP properties. The arrows indicate the minimum reserve factor element.

As previously summarised in Table 3.11, the maximum relative difference in shell minimum reserve factor between the results obtained with original and composite PCOMP is 5.6%, which does not occur for the original sizing load case. The location of the critical element did not change, and the relative difference in shell minimum reserve factor for PSHELL and PCOMP bracket modelling is 2.4%, corroborating that the design methodology chosen in subsection 3.4.1 for the bracket modelling is appropriate.

As the design criteria requirements regarding the minimum reserve factors in the shells for composite actuator brackets as described in subsection 3.4.1 are met, the minimum reserve factor of the actuator brackets is investigated. The minimum reserve factor for the composite actuator brackets only is shown in Table 3.13. It occurs for the same main load that sizes the original rudder shells (one engine out) and temperature (-54°C), but jamming of AC 1 in extension instead of retraction.

Bracket Mat.	LC	$\frac{\varepsilon_{XX}}{\varepsilon_{XX,allow}}$	$\frac{\varepsilon_{YY}}{\varepsilon_{YY,allow}}$	$\frac{\gamma_{XY}}{\gamma_{XY,allow}}$	RF	Location
CFRP	03-02-02	0.02	0.17	0.57	1.68	Aft Row Region 3 AC 1

Table 3.13: AC Brackets Minimum Reserve Factor Summary for PCOMP Bracket Modelling

The area with the highest shear strains in the original metallic brackets is in the triangular elements in region 1, the attachment point to the actuators. The strain distribution in the composite bracket differs from the original design by having the maximum strain element in region 3 instead of the actuator attachment region.

This is a sign that the bracket area in region 3 has to be increased if is desired to retain the location of the minimum reserve factor element. It is desired to obtain the maximum shear strain at the load introduction point and not elsewhere, even if all reserve factors are above 1, as the current maximum shear strain element has one interface to the spar flange and one to the spar web, riveted surfaces.

Hence, the thickness is increased with 2 0° plies in region 3. The PSHELL simulations indicate that the minimum reserve factor is in the bracket actuator attachment area of AC 1 and strains are decreased, as the minimum reserve factor becomes 1.74. The PCOMP modelling results in the attachment area of AC 1 as the location of the highest loaded element, with the minimum reserve factor of 1.67. The final comparison for the minimum reserve factor for the actuator bracket is shown in Table 3.14, noting that the addition of the 2 plies in the brackets did not change the minimum reserve factor for the rudder shells.

Property	$\frac{\varepsilon_{XX}}{\varepsilon_{XX,allow}}$	$\frac{\varepsilon_{YY}}{\varepsilon_{YY,allow}}$	$\frac{\gamma_{XY}}{\gamma_{XY,allow}}$	RF	Location
PSHELL	0.02	0.16	0.55	1.74	Attachment area AC1
PCOMP	0.01	0.18	0.57	1.67	Attachment area AC1

Table 3.14: Final AC Brackets Minimum Reserve Factor Summary for LC-03-02-02

The final layup proposed per region for the composite actuator brackets is given in Table 3.15. The only change is brought in region 3 with the addition of the two 0° plies, increasing the thickness by 0.7 mm.

Bracket region	Layup	Thickness [mm]
Region 1	$[[45/0_4]_2/45/0_3/[45/0_4]_3/45/0_2]_s$	22.4
Region 2	$[[45/0_3]_4/[45/0_2]_2]_s$	15.4
Region 3	$[[45/0_4]_2/[45/0_2]_2]_s$	10.5

Table 3.15: Final PCOMP Properties of the AC Brackets per Region

As the shell reserve factors meet the design criterion, no further attempt to reduce the strain levels by increasing the actuator bracket thickness was attempted in the stage due to no extra benefit at the cost of weight. The strains can be further decreased by increasing the thickness, but not significantly, as the material properties do not change with increasing thickness, while unnecessarily increasing the weight.

The overall maximum strains occur in the hinge arm metallic brackets and the von Mises changes are below 5%. The final material properties per region given the layup sequence presented in Table 3.15 are given in Table 3.16.

AC area	$E_m[GPa]$	$G_m[GPa]$	$E_b[GPa]$	$G_b[GPa]$	$\nu_{12,m}$	$\nu_{12,b}$	Thick. [mm]
Region 1	59.2	9.7	58.2	10.5	0.14	0.15	22.4
Region 2	57.3	11.2	56.0	12.1	0.16	0.18	15.4
Region 3	57.1	11.3	55.7	12.2	0.17	0.19	10.5

Table 3.16: Final AC Brackets Material Properties Summary

The shear strain distributions for the original metallic, composite PSHELL and PCOMP are depicted in Figure 3.16. The shear strain distribution in the composite brackets did not change with the addition of the two 0° plies in region 3, only the location of the minimum reserve factor element changes.

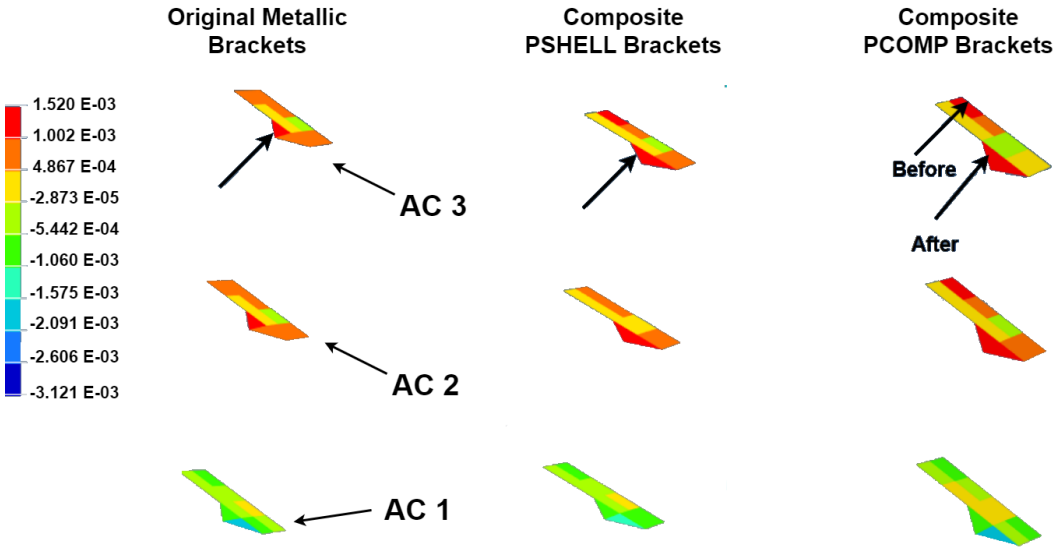

Figure 3.16: Final Strain Distribution in the Actuator Brackets Comparison Before and After the Increase in Thickness in Region 3. From left to right, the results correspond to the original metallic brackets modelling, SHELL and PCOMP modelling of the composite brackets

Lastly, the load transfer capacity in the attachment area (region 1, which accommodates a bolt) is analysed. The bracket attachment area is the first load introduction of the actuator jamming load. The peak strains at the load introduction elements are checked for load transfer viability. Even though the reserve factors are above 1, the load transfer is checked for bearing failure, given by Equation 3.3 [50],[15], where F is the nodal force extracted from the FEM results, $\sigma_{bearing}$ is the bearing stress, t is the thickness of one flange, n is the number of rivet rows and d is the bolt diameter. The maximum allowed bearing stress for composite is 440 MPa (Airbus cortesy), and the number of fastener rows n in the x and z axes is one, as the connection is ensured by one bolt.

$$\sigma_{bearing} = \frac{F_x}{n_z t d} \tag{3.3}$$

Since the actuator-bracket interface contains one bolt with a diameter of 25 mm, the thickness of one flange in the actuator attachment region is 11.2 mm and the transferred force in the x-direction is 16.5kN, the actual bearing stress in the bracket is 60 MPa, way below the 440 MPa limit, rendering the design safe.

As the overall bracket strain distribution remains unaltered and the RF in the shell presents a small, acceptable difference compared to the original design, no further iteration for bracket thickness has been performed, as this would lead to weight increase while the reserve factor is above 1.

3.5 Spar-box Concepts

All rudder modifications implied by the introduction of each spar-box concept are thoroughly described in this section, which commences with the presentation of the concepts containing the composite brackets design for principles 1 and 2 in subsection 3.5.1 and subsection 3.5.2, subsequently. Eventually, the metallic bracket design applied in the context of principle 1 is delineated in subsection 3.5.3.

3.5.1 Concept A: Local Torsion Stiffening Spar-Box Concepts

The first proposed concept encapsulates principle 1 and involves attaching a box on the spar in the area of the actuators, riveting it at the interface between the spar and the rudder shell. The metallic brackets are substituted with composite ones and become part of the box ribs, extending the brackets up to the roof of the spar-box, as illustrated in Figure 3.17.

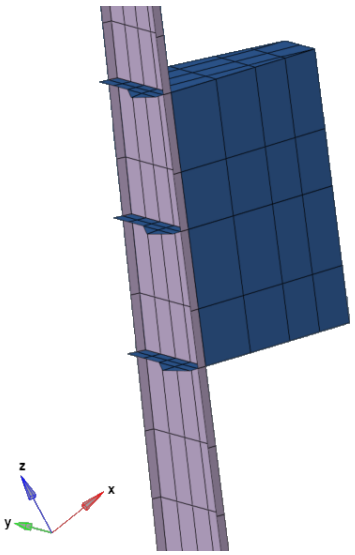

Figure 3.17: Concept A FEM Mesh. Different Colours Correspond to Different Components

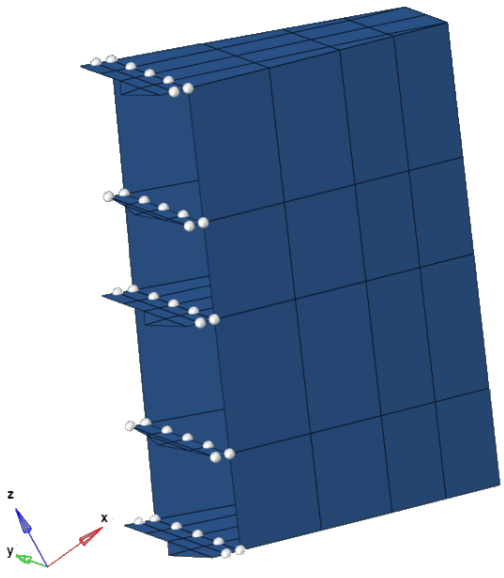

Figure 3.18: Box Concept A Connection Nodes Between the Spar Web, Rudder Shells Monolithic Overhang, Spar-box, Actuator and Hinge Brackets

The structure resulting from the merging of the AC bracket and spar-box web is connected to the spar, Figure 3.18 showing the common grid points with the spar. In reality, rivets connect the spar components to the box and rudder shells along those lines (rivet pitch is different from grid point pitch). The material of the hinge brackets, which provide the attachment interface for the hinge arm, remains metallic.

This spar-box attachment to the spar and rudder shells is the reflection of the first identified design philosophy to separate the internal loads from the external loads, which eventually will enable the use of green materials with lower mechanical properties or CFRP thermoplastics, which present multi-layer manufacturing challenges. While the rudder shells are torsionally stiffer than the spar-box as they enclose a higher area, the spar-box enables load relief in the rudder shells in case of system failure due to the locally increased torsional stiffness.

The changes performed on the rudder system compared to the current model for concept A are listed below.

- Enclosing the spar in the AC area with a box, modelled as described in subsection 3.3.2
- The AC brackets are turned to composites (instead of metallic) as described in subsection 3.4.4
- AC brackets extend to the roof of the spar-box as box ribs
- The reinforcements are removed and the rudder shell model presented in subsection 3.2.1 is used
- The spar is sectioned into 4 components. However, the rivets are not modelled

The advantage of concept A is that except for the actuator bracket material, there is no other major design alteration required in the original rudder components to accommodate the box, which makes the concept easier to implement. The actuator-spar-shell connection remains the same, thus no major stiffness modifications occur and consequently no change in modal shapes and natural frequencies is expected.

The disadvantage of this design is that due to the shell-to-spar connection, part of the jamming load is still taken by the shells. The torsional stiffness of the shells is higher than that of the box, due to the higher enclosed area. Thus, to reduce the strain values, the box also requires a relatively big profile area, but the loads in the box will not be very high, thus relatively high reserve factors are expected, which indicates an inefficient use of material rendering the structure heavier than it should be.

Analysing the design requirements, some expectations can be created for the outcome of the modal and static analyses. Since no major stiffness modifications have been performed for concept A, the natural frequencies or modes are not expected to vary significantly from the current ones.

The reserve factors are expected to be slightly smaller due to the bracket material change, already predicted by results shown in subsection 3.4.4. On the other hand, the main load case for which the minimum RF occurs is not expected to change (one engine out), along with the critical location, which is the ramp above AC1.

3.5.2 Concept B: Structurally De-coupled Spar-box Concept

Concept B incorporates the second designing principle, structural decoupling. The box has the same geometry as concept A with the brackets being made out of composite, the difference being represented by the spar-box attachment to the rudder shells.

In order to avoid the introduction of the jamming loads in the shells, they are disconnected from the rudder spar in the area of the actuators. Physically, this is equivalent to the rivet removal between AC 1 and AC 3 at the spar-shell interface.

In the FEM model, this design feature is implemented by creating two sets of nodes with the same coordinates at the spar-shell interface between AC 1 and AC 3, disconnecting the spar elements (containing one set of nodes) from the shell elements (containing the other set of nodes).

Due to the spar-shell structural separation (represented by the lack of rivetting) in the area of the actuators, the spar flanges between AC 1 and AC 3 are removed from the design, as their sole function is to provide the interface surface for riveting (no loads are applied at the spar flanges nodes). This enables a slight reduction of the spar weight, one of the design advantages.

The free edges created at the spar-shell interface and between the three independent spar components are indicated in Figure 3.19 as red lines, the spar-box covering the middle spar component. Additionally, the deletion of the spar flanges between AC 1 and AC 3 can also be visualised in Figure 3.19.

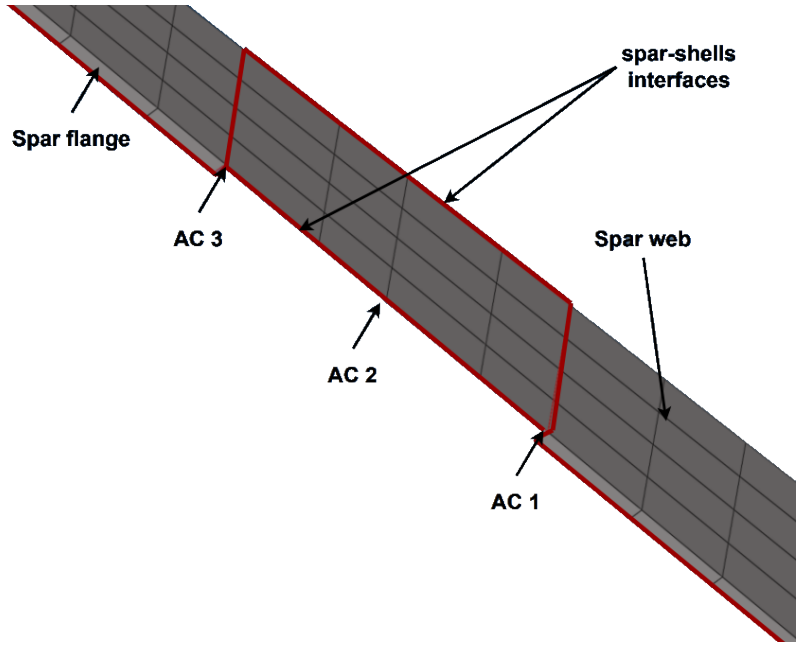

Figure 3.19: Rudder Spar Free Edges Indicatedon thr Spar Mesh by the Red Lines. Also, the Spar Flanges are Absent between AC 1 and AC 3

Moreover, to avoid big twist deformations, the spar is separated into three independent components by completely cutting the spar web at the location of the upper and bottom actuator

brackets, AC 1 and AC 3 (the components are not joined by means of riveting). Again, two sets of nodes with the same coordinates are created in the spar web at the AC 1 and AC3 locations to disconnect the three independent spar components in the FEM model.

With this design solution, the relatively low aerodynamic forces are the only loads acting on the rudder shells, and the actuator force fighting loads are introduced only in the spar-box. Thus, the internal and external loads are carried by different structures.

However, there must be one connection between the spar-box and the shells, otherwise, the rudder deflection would not take place, as it would be completely disconnected from the actuators. This connection requires a larger monolithic area in the shells in the region of the actuators to accommodate a shear joint to the spar-box. It is not ideal to place the connection in the sandwich area, as no holes and fasteners should be present through the core to prevent moisture ingression [37].

Thus, the ramp of the sandwich shells is locally moved one row of elements more aft, towards the trailing edge of the rudder and creates a monolithic area to connect the box. The spar-box concept attached to the spar is depicted in Figure 3.20 with the two grid points that model the box attachment to the shells and the updated properties of the shells, including the common nodes with the box, can be visualised in Figure 3.21. Significant connection stiffness modifications are mitigated by modelling the box-shell connection containing one node common for the spar, the middle actuator bracket, the box and the rudder shell.

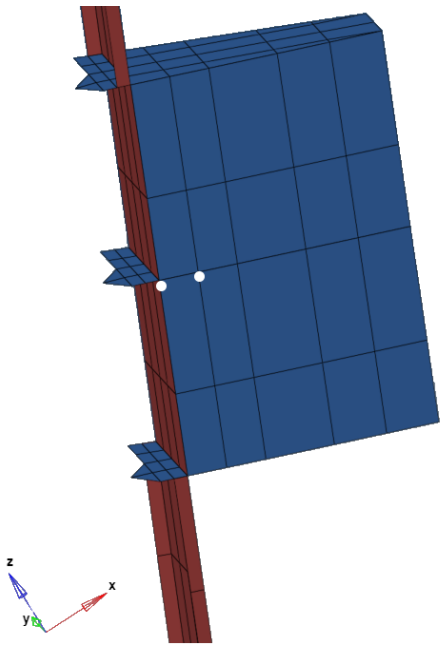

Figure 3.20: Decoupeled Spar-box Concep FEM Mesh with Box-Shell Interface Nodes. Different Colours Indicate Different Structural Components

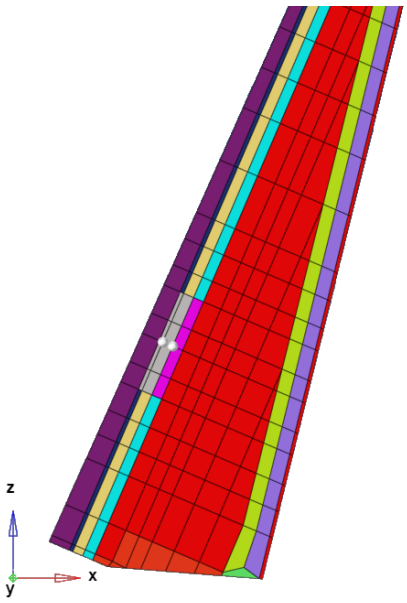

Figure 3.21: Rudder FEM Mesh and Box-shell Connecting Nodes. Different Colours Indicate Different PCOMP Properties

The PCOMP FEM property modelling legend of the extended monolithic area is presented in Figure 3.22. The layup sequence per PCOMP property, created by accounting for the

composite design rules, is given by Figure 3.23. It has been chosen to use mainly 0 ° layers because of the actuator loads, and the thickness is limited by manufacturing aspects, allowing three extra layers compared to the overhang area, to avoid big thickness transitions that would affect the quality of the structure.

Figure 3.22: PCOMP Property Legend of the Extended Monolithic Area

Property	Sequence
PCOMP 8	$[45°/0°_3/45°/0°]_s$
PCOMP 9	$[45°/0°/15\ mm\ core]_s$

Figure 3.23: Layup Sequence per PCOPMP Property of the Extended Monolithic Area

The decoupled spar-box has the same web profile at all actuator bracket locations and the same profile shape in the areas between the actuators, as previously depicted in Figure 3.8 and Figure 3.9. Moreover, the extended monolithic area is present between AC 1 and AC 3, not only AC 2, where the box-shell riveted connection is located.

The reason for these design choices is represented by the desire to maximise the enclosed area of the box. Moreover, the extended monolithic area contains more than one or two fabric layers, rendering this area in the shells stronger compared to the sandwich ramp.

All the bullet points enumerated for concept A apply. Below, additional changes valid for concept B only are enumerated.

- The web is cut at the location of the AC1 and AC3 without riveting, resulting in a 4-component spar, not connected by fasteners
- The box is connected directly to the rudder shells via a shear joint
- Span-wise, in the area of the spar-box (between AC1 and AC3), the first 50 mm in the x-direction at the rudder shell leading edge are monolithic and the ramp-down is moved in this area 50 mm in the x-direction, as depicted in Figure 3.21
- In the area of the spar-box (between AC1 and AC3), the spar flanges are deleted

The main advantage of concept B is that it structurally decouples the box from the shell and subsequently, most of the actuator jamming loads are carried by the spar-box. This results in a lower box mass, as the enclosed area of the box does not have to compete with the higher torsional stiffness provided by the shell dimension. Hence, the material would be used more efficiently.

On the other hand, structural decoupling can lead to a local change in the stiffness provided by the actuators due to their disconnection from the rest of the rudder, which might result in frequency changes and modal shapes. This aspect will be checked with a modal analysis in the next chapter.

Another point of concern would be the assessment of the elements containing the two grid points modelling the box-shell connection, which might feature peak strains, as all the load

transfer takes place via the two nodes. In reality, there will be a shear join at the box-shell interface, and the load would be transferred by more than 2 rivets.

Thus, the peak strains might not be realistic, and the load transfer capabilities have to be separately checked with initial calculations for bearing stress. The bearing stress check is performed in the same way it was done in the case of the composite actuator brackets in the attachment area, with the equation repeated for convenience in Equation 3.4, where F is the nodal force extracted from the FEM results, $\sigma_{bearing}$ is the bearing stress, t is the thickness of one flange and d is the bolt diameter. .

$$\sigma_{bearing} = \frac{F_x}{n_z t d} \tag{3.4}$$

Moreover, the monolithic area had to be extended to the shells in the area of the actuators to accommodate the connection to the box. Thus, manufacturing modifications have to be performed on both the actuator brackets and shells. However, the shells would be manufactured with completely different technology compared to the current ones, thus possible manufacturing challenges caused by a local design modification can be addressed from the beginning.

While the external sizing load case, one engine out, is not expected to modify, the location of the minimum reserve factor might change, to occur in the region of AC 2, even if AC 1 or AC 3 jams and the peak strain elements are disregarded, due to the box-shell connection in the area of AC 2. In the detailed design phase, the calculations for buckling will be performed for the extended monolithic area as well, in addition to the spar-box.

3.5.3 Concept C: Truss Spar-box Concept

The third concept retains the metallic brackets design while incorporating principle 1, thus no modifications are performed on the actuator brackets compared to the original design. The brackets are connected to the roof of the spar-box via a metallic truss structure.

The main advantage of concept C is the retention of the current bracket design. Moreover, if the truss structure can lead the jamming loads in the spar-box, the concept has the potential to reduce the weight compared to concepts A and B. Conversely, the disadvantage is represented by the composite-metal contact that would lead to galvanic corrosion problems and requires insulation, such as glass fibre fabric.

The trusses are arranged in an X shape as this geometry is good for carrying shear and one vertical truss would provide a load path for the jamming force with its main contribution in the x-direction. In this concept, the shells are still riveted along the entire span to the spar flanges, similar to concept A.

The box has the same cross-sectional geometry as the other two concepts, but the webs attached to the brackets for the spar-box ribs are substituted with a metallic truss structure, which is modelled with three stiff CROD elements, as shown in Figure 3.24 and Figure 3.25.

The property card used for the CROD elements representing the truss structure is given in Table 3.17 with the material and profile area used to account for the truss stiffness, corresponding to the actuator properties. A very high stiffness (due to the unrealistically high

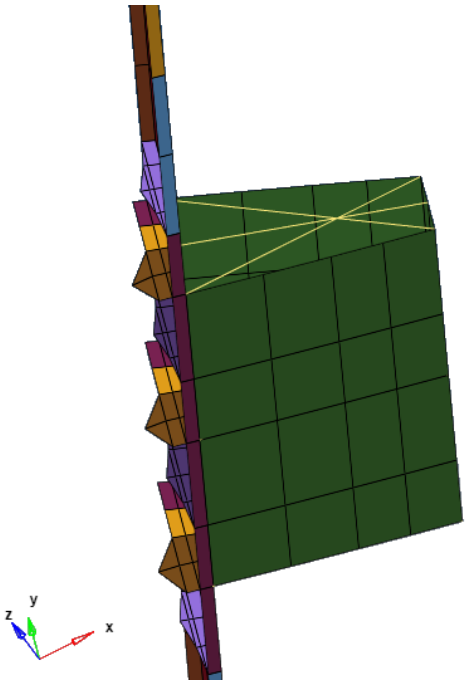

Figure 3.24: FEM Modelling of the Truss Spar-box. Different Colours Correspond to Different Element PCOMP Properties (or PROD in the Case of Trusses)

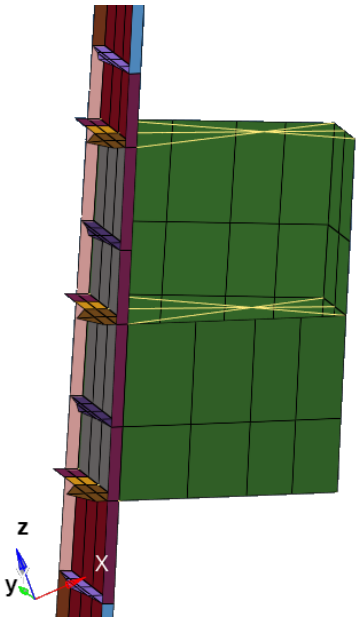

Figure 3.25: FEM Modelling of the Truss Spar-box with the Left-hand Wall Partially Hidden to Allow the AC 2 Truss System View

cross-sectional area) is assigned to the CROD elements to investigate the design feasibility only!

Property	Material	Area $[mm^2]$
PROD	Aluminium	551

Table 3.17: Truss FEM Property Modelling for Concept C

It is expected that the strain will be relatively high as the truss structure might not be able to introduce the actuator loads into the spar-box as effectively as the composite webs. In case the stiffness of the trusses is not big enough, a significant shift should be observed in the natural frequencies as well with the possibility of introducing new modes. Making the trusses stiffer would lead to a weight increase, which would be an indicator of the poor performance of the concept.

Chapter 4

Spar-box Concept Trade-off

This chapter encompasses the trade-off set-up for the previously described three spar-box concepts. In section 4.1, the general trade-off methodology and set-up are presented, also establishing the relevant criteria, particularly for the current study, based on the design requirements. The concepts are further analysed in the context of appropriate FEM simulations that enable the evaluation of the defined trade-off criteria, the numerical results supporting the criteria assessment being presented in section 4.2. Lastly, the trade-off results are presented in section 4.3, which enables the identification of the feasible concepts.

4.1 Trade-off set-up

A common and unbiased trade-off methodology relies on the Analytical Hierarchy Process [19], [42], where the trade-off weights are determined by performing a relative comparison between criteria. The general trade-off methodology is presented in subsection 4.1.1, being followed by the criteria definition in subsection 4.1.2 and the corresponding trade-off weights attribution in subsection 4.1.3.

4.1.1 Trade-off Methodology

The first step undertaken during the trade-off process is represented by the relevant criteria establishment, to which the appropriate weights have to be attributed based on an importance and relevance assessment.

The criteria importance comparison can be conducted in a table like Table 4.1, where r denotes the assessment coefficients, chosen accordingly based on a defined scale. While it could be argued that the numerical values selected for the relative coefficient still might not be entirely objective, providing a clear scale definition and reasoning, mitigates the risk of introducing an unconscious bias during the trade-off process.

The numerical values of the relative coefficients are attributed based on the scale presented in Table 4.2. In case one criterion is more important than another, the inverse of the coefficient

	Criterion 1	Criterion 2	Criterion 3	Criterion j
Criterion 1	1	$r_{1,2}$	$r_{1,3}$	$r_{1,j}$
Criterion 2	$r_{2,1}$	1	$r_{2,3}$	$r_{2,j}$
Criterion 3	$r_{3,1}$	$r_{3,2}$	1	$r_{3,j}$
Criterion i	$r_{i,1}$	$r_{i,2}$	$r_{i,3}$	$r_{i,j}$

Table 4.1: Weight Attribution Table Template

is attributed to the mirrored element in the matrix (e.g. 0.5 when the symmetric element is 2, 0.33 when the symmetric element is 3).

Scale	Meaning
1	Equally important
2	Slightly more important
3	Moderately more important
4	Strongly more important
5	Other aspects become negligible

Table 4.2: Relative Coefficients Scale

The study goal, which should be attained by the trade-off result, plays a major role in assigning the numerical value of the relative coefficient. While the equally important coefficient attribution (the numerical value of 1) is self-explanatory, slightly more important provides the possibility to evaluate criteria that under normal circumstances would be equally important for the design, but the assessment method is not on the same detail level.

If on a general note, the criteria are equally important, but one affects the result more based on the study goal and the methods are consistent, moderately more important is assigned, but if the methods do not provide the same detail of analysis, 4 is assigned. The value of 5 should be attributed if there is a clear dominant aspect that drives and defines the trade-off, irrespective of the used methods.

For each column, an intermediate weighting factor v_i is calculated using Equation 4.1. The final weight is then computed using Equation 4.2.

$$v_i = \left(\prod_{j=1}^{n} r_{i,j} \right)^{\frac{1}{n}} \tag{4.1}$$

$$w_i = \frac{v_i}{\sum_{i=1}^{n} v_i} \tag{4.2}$$

Once the weighting factors are determined, the criteria can be assessed per concept based on a scale as presented in Table 4.3, where the meaning of the scale is self-explanatory, and the provided reasoning should mitigate the risk of bias. Intermediate values (.5) can be assigned if the concepts are comparable (e.g. two concepts can be good, but still one slightly outperforms the other). The numbers are multiplied by the trade-off weight and simply summed up, being normalised at the end.

Scale	Legend
1	Not feasible
1.5	
2	Improvable
2.5	
3	Sufficient
3.5	
4	Good
4.5	
5	Exceeds expectations

Table 4.3: Criteria Assessment Scale

4.1.2 Trade-off Criteria Establishment

As a first step in the particularised trade-off, the criteria are defined, being mainly derived from the design requirements. They can be both quantitative and qualitative and represent important considerations in attaining the study goal, which is the preliminary structural design of a rudder spar-box that is able to carry torsional system failure loads.

As the reserve factors define the structural performance under static loading, computing and identifying the rudder shell minimum reserve factor is essential. It provides an understanding of the load distribution, level and critical location, enabling a valuable comparison with the original design and defining the feasibility of the concept.

Since all three spar-box concepts use the same box geometry and FEM modelling, having the minimum reserve factor in the rudder shells as a criterion enables the identification of the spar-box design that efficiently decreases the strain levels in the shells. Hence, the first criterion quantitatively addresses **REQ-01-DESIGN**.

As previously mentioned, aeroelasticity is a very important aspect to consider during the rudder design, as changes in mass and stiffness distribution could lead to flutter problems. Thus, the second criterion is numerically quantified by the natural frequency and modal shapes assessment, addressing **REQ-02-DESIGN** and **REQ-03-DESIGN**. As the preliminary design relies with priority on the structural performance under static loading, a dynamic analysis is not performed, as results would be more conducive for a defined initial, more detailed structure than a preliminary one.

Since the same, unoptimised, spar-box FEM modelling is used for the three concepts, the assessed weight is the one of the overall rudder, the third criterion being also quantitatively assessed, addressing **REQ-04-DESIGN**. In the case of the spar-box itself, weight minimisation is the objective function rather than a trade-off criterion.

The initial spar-box design does not surpass the initial reinforcement weight by more than 5% (disregarding the truss structure for concept C), and the criterion is meant to compare the effects of the concepts on the rudders shells modifications on weight, such as the actuator bracket material change or extension of the monolithic area in the shells.

From the concept presentations, it was anticipated that peak strains are expected due to the connection nature between the spar-box and rudder, especially for concept B. However, the peak strains might not represent the realistic strain level, as in reality there would be more than one row of rivets. For this reason, a criterion dedicated to studying load transfer feasibility is established, due to the differences in load transfer nature based on the two different enunciated principles. Thus, a simple analysis for preliminary calculations for bearing stress can show the viability of the load transfer.

The first four criteria can be numerically quantified. However, two qualitative criteria were introduced regarding manufacturing & assembly and reparability & inspectability. The first one addresses the feasibility of design implementation, as the ease of manufacturing plays a role in the delivery lead time.

Reparability and inspectability address in-service and operational needs, as structural components often need inspections and repairs, and the lead time for such activities is a driver in the aircraft design decision-making process. The structure should be easily inspectable and repairable, one key aspect during the aircraft's operational lifetime.

Buckling is a driving aspect for the thickness of the spar-box components and the buckling load is not assessed in the trade-off, as it is relevant for the weight optimisation of the feasible concept(s). The trade-off aims to assess the spar-box concepts' performance based on the principles (thus on the type of box-shell connection) and since the same spar-box geometry is used for all concepts, there is no weight difference due to the spar-box components' thickness.

4.1.3 Weight Attribution

As the criteria have been established, their corresponding weight can be computed in Table 4.4 and the coefficient designation process is detailed below. The coefficient attribution is performed per column (the criterion stated at the top of the column is compared against the other criteria). The criteria final wights add up to 1.

	RF	Natural frequencies	Load Transfer	Weight	Manufacturing& Assembly	Reparability & Inspectability
RF	1	0.5	0.5	0.5	0.33	0.33
Natural frequencies	2	1	1	1	0.33	0.33
Load Transfer	2	1	1	1	0.33	0.33
Weight	2	1	1	1	0.33	0.33
Manufacturing& Assembly	3	3	3	3	1	1
Reparability& Inspectability	3	3	3	3	1	1
Final weight	0.29	0.19	0.19	0.19	0.07	0.07

Table 4.4: Weight Attribution Table for the Spar-box Concept Trade-off Criteria

The structural performance assessment for static loads is also a validation and certification method, linked to experimental data, due to the use of strain allowables to compute reserve

factors. The modal analysis, load transfer and weight assessments are not detailed calculations used for certification and are not linked to experimental data. Moreover, they are not addressed with detailed calculations, but rather preliminary ones (no separate, specific dynamic or aeroelastic analysis is performed, also no detailed shear joint assessment). For a product certification, a more detailed analysis would be performed. Even though under normal circumstances the four criteria would be equally important for the rudder and certification, only the reserve factors are assessed accordingly.

Consequently, the reserve factor criterion is rated with 2 in comparison to natural frequencies, load transfer and weight, while the latter three are rated with 1 in comparison to each other, as it can be seen in Table 4.4.

Manufacturing& assembly and reparability& inspectability are equally important to each other, as they are both linked to the aircraft operation. While these are important considerations, they are not as critical as the others in proving the design feasibility from a concept perspective, they can make a difference instead. Moreover, the two criteria are assessed qualitatively, and no NDT methods are applied to experimentally prove the manufacturing& assembly and reparability& inspectability, they are addressed from engineering experience. While manufacturing and reparability aspects are important for the aircraft's performance over its entire operational lifetime, these are simply not as relevant as the others for the formulated goal of the thesis.

Subsequently, a 1 is assigned when comparing Manufacturing& Assembly and Reparability& Inspectability to each other, and a 0.33 when compared to the other quantitative criteria (and a 3 assigned for the mirrored element of the matrix in Table 4.4).

4.2 Trade-off Criteria Assessment

This section presents the criteria assessment based on FEM analysis results, commencing with the reserve factors in subsection 4.2.1 and continuing with the peak strain and load transfer assessment in subsection 4.2.2. The static loading assessment is continued with modal analysis results in subsection 4.2.3 and weight comparison in subsection 4.2.4. The quantitative criteria are complemented with the qualitative assessment of the last 2 criteria in subsection 4.2.5. Finally, the trade-off results are presented and commented in section 4.3.

4.2.1 Reserve Factors

The first criterion quantifies the numerical value of the minimum reserve factor in the rudder shells for each concept. Hence, a straightforward assessment and comparison can be performed between the three concepts regarding their structural performance under static loading.

The minimum reserve factors have been identified and computed by running a static analysis for all three concepts, based on the FEM models and load selection as presented in the previous chapter. The strains in the three directions have been extracted in the analysis system (thus principal strains) and the reserve factors are computed per element, as the maximum strains in the three directions do not occur in the same element.

For all three concepts, the one engine out with actuator 1 jammed while retracting at 80°C load case, LC-03-01-01, resulted in the smallest reserve factors, similar to the original design,

except the temperature. Figure 4.1 shows the shear strain distributions for LC-03-01-01, revealing also the peak strains predicted for concept B, indicating a general load alleviation in the rudder towards its trailing edge.

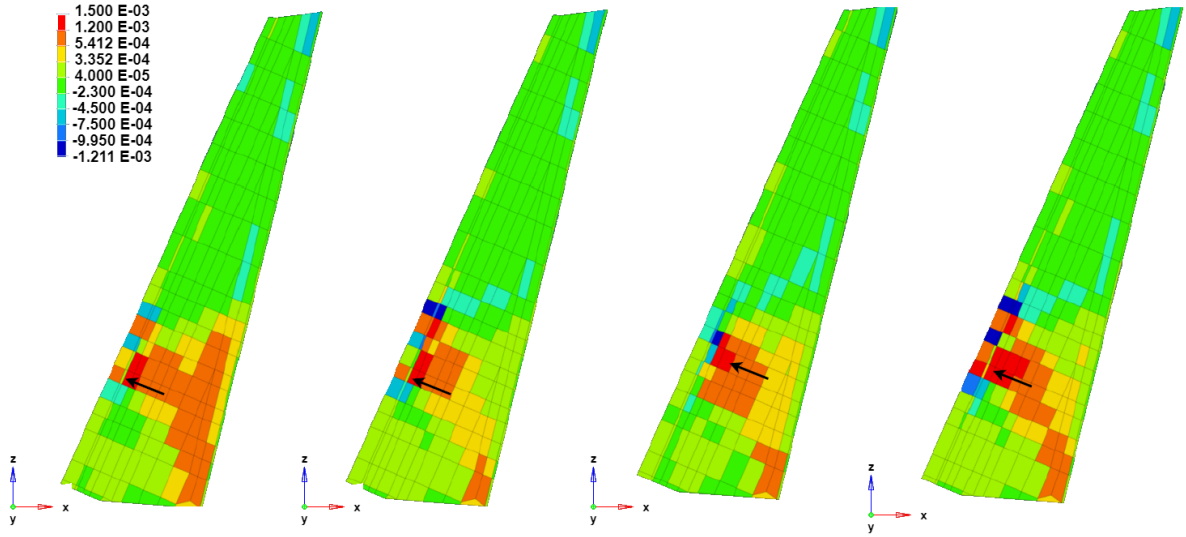

Figure 4.1: Shear Strain Distribution Comparison in the Original Rudder Shells (Figure 3.2) obtained by running a static analysis of the GFEM (Figure 2.12) for the sizing load case (minimum RF) LC 03-01-01. From left to right, the strains are plotted for the results obtained with the original design, concept A (the local torsion stiffening concept), concept B (the decoupled concept) and concept C (the truss concept). The arrows indicate the minimum reserve factor element.

However, the peak strains occurring at the box-shell connection might not be realistic because in reality there would be a joint with more than one row of rivets. The choice of analysed elements must be carefully chosen for concept B in this case for the trade-off. The feasibility of load transfer for concept B is assessed in the next criterion.

The reserve factors are given in Table 4.5, with the strain ratios in all three directions, minimum shell reserve factors and also their corresponding locations. All minimum reserve factors occur on the left-hand side, where the actuator load introduction is.

Concept	LC	$\frac{\varepsilon_{xx}}{\varepsilon_{xx,allow}}$	$\frac{\varepsilon_{yy}}{\varepsilon_{yy,allow}}$	$\frac{\varepsilon_{xy}}{\varepsilon_{xy,allow}}$	Min RF	Location
Original	03-01-02	0.09	0.35	0.70	1.27	Ramp Above AC 1
A	03-01-01	0.01	0.14	0.81	1.22	Ramp Above AC1
B with Peaks	03-02-02	0.15	0.09	1.39	0.71	Monolithic Above AC 2
B without Peaks	03-02-01	0.22	0.01	0.78	1.23	Shell
C	03-01-02	0.01	0.17	1.03	0.96	Ramp Above AC 1

Table 4.5: Rudder Shells Minimum Reserve Factors

For all concepts, A, B and C, the shear strains are locally increased close to the AC1 bracket, for concepts A and B due to the actuator bracket material change, and for concept C mainly

due to the inefficient truss structure. On the other hand, the strains are further reduced towards the trailing edge. Thus, it can be concluded that the presence of the spar-box also generally reduces the strains in the region of the actuators.

The minimum reserve factor occurs in the same element for the same load case. For concepts A and C, it occurs in the ramp area, as for the original design, and for concept B, it is in the shell AC 2 area, where the core has a thickness of 30 mm.

It can be seen from Table 4.5 that for concepts A and B (without peak strains), the minimum reserve factor occurs for the same base load as the original design, just at different temperatures. This can be directly attributed to the change in bracket material, from metallic to composite, as the latter one has a smaller thermal expansion coefficient.

As expected, it can be seen that the peak stresses for the de-coupled box occur in the shells that contain the connecting grid points, and in the monolithic area that is connected to the spar flanges, which also contain one of the two connecting grid points. However, if the peak strains are disregarded, the minimum reserve factor occurs in the shell, close to the ramp in the area of AC2 and AC1.

Given that with an unoptimised spar-box, the reserve factors are slightly lower compared to the ones pertaining to the current rudder design (1.23 compared to 1.27), concepts A and B are perceived to be between sufficient and good, being awarded a score of 3.5.

The results indicate that for concept C, the truss structure connecting the actuator brackets to the box top can not reduce the shear strains and redirect them in the spar-box. Thus, it can be concluded that the spar-box ribs play a major role in introducing the shear loads in the spar-box, as they capture the loads in the x-axis and reintroduce them as shear in the spar-box. Consequently, concept C is considered unfeasible and awarded a score of 1.

4.2.2 Load Transfer

The main aim of the second criterion is to investigate if the load can be safely transferred in the case of concept B, which poses a sole shear joint between the shells and spar-box, addressing the issue regarding the peak strain elements.

In the case of peak strain elements containing nodes that model a (shear) joint, the feasibility of carrying the load can be checked for preliminary calculations regarding joint failure. The desired failure mode is bearing stress, as it is the least violent.

With the formula for the bearing stress state, the required number of rivet rows can be computed. If the number is not realistic for the loading extracted from the FEM simulations, the design is not feasible.

Knowing that the maximum allowed bearing stress for composites as used by Airbus is 440 MPa (conservative value), the number of fastener rows in the x and z axes is given by Equation 4.3 [50],[15]. Equation 4.3 provides means for a preliminary shear joint assessment, which does not include secondary bending, interference effects, fatigue performance and bypass effects (bypass influencing fatigue only, not the bearing strength).

$$\sigma = \frac{F}{ntd} \Longrightarrow n_x = \frac{F_z}{\sigma td} \quad n_z = \frac{F_x}{\sigma td} \tag{4.3}$$

The interface loads corresponding to the common nodes, shared by the shells and the spar-box, that model the shear joint, can be extracted from the static FEM simulation and be implemented in the analytical formula for bearing stress, given by Equation 4.3.

Since the peak strains (at a joint location) occurred only for concept B, the other 2 concepts are not subjected to calculations for bearing stress. For the calculations, rivets with a 6.4 mm diameter have been utilised, which is a standard in manufacturing the rudder and other aircraft components. The number of rivet rows in the relevant orientation and the corresponding loading are given in Table 4.6, with the number of rivets rounded to the upper integer.

F_x [kN]	n_z	F_z [kN]	n_x
13.8	2	67.5	6

Table 4.6: Transfer Forces and Resulting Number of Rivet Rows for Bearing Stress Calculations

As a rule of thumb, to avoid stress concentrations, the recommended distance between rivets is around three times the diameter [20], [29], [38] (compared to metallic components, where the Sain Vernant principle describes a stress filed uniformisation within a distance equal to three times the rivet radius; for composites, the stress field becomes uniform within a greater distance). Given that the length covered by the two elements along the x-axis account for is 118.76 mm and the rivets have a 6.4mm diameter, the rivet pitch should be at least 19.2mm. For the available length, 118.76 mm, and 6 rivet rows, the resulting rivet pitch would be 19.8mm, which is higher than 19.2 mm.

Consequently, the results entailed by the preliminary calculations, the load can be safely transferred between the spar-box and the rudder shells for concept B, thus the concept is evaluated with a 4. Since there are no particular peak strain elements for concepts A and C that would entail problems in load transfer, they are also rated with 4.

4.2.3 Natural Frequencies

For aeroelastic considerations, it is important that the natural frequencies, especially the first elastic eigenfrequency, do not change dramatically, with a maximum allowable change of 7% for preliminary designs.

A modal analysis is performed on the VTP with the three spar-box concepts implemented. For these simulations, only the VTP fin and rudder are modelled, without the rear fuselage, as depicted in Figure 4.2, while still applying the appropriate boundary conditions.

Omitting the rear fuselage is appropriate since the mode shapes do not reflect the real displacement magnitudes, and the boundary conditions are enough to capture the VTP natural frequencies. Moreover, its modelling could lead the analysis away from the VTP assessment, which is the goal of the study.

Another important consideration is represented by the discrepancies between the FEM model and the real structure. It is known that the mass of the FEM model, computed with the reported material densities, is smaller than the one of the real VTP, as the weight of the paint, hoisting points and rivets are not accounted for. Thus, the natural frequencies resulting from

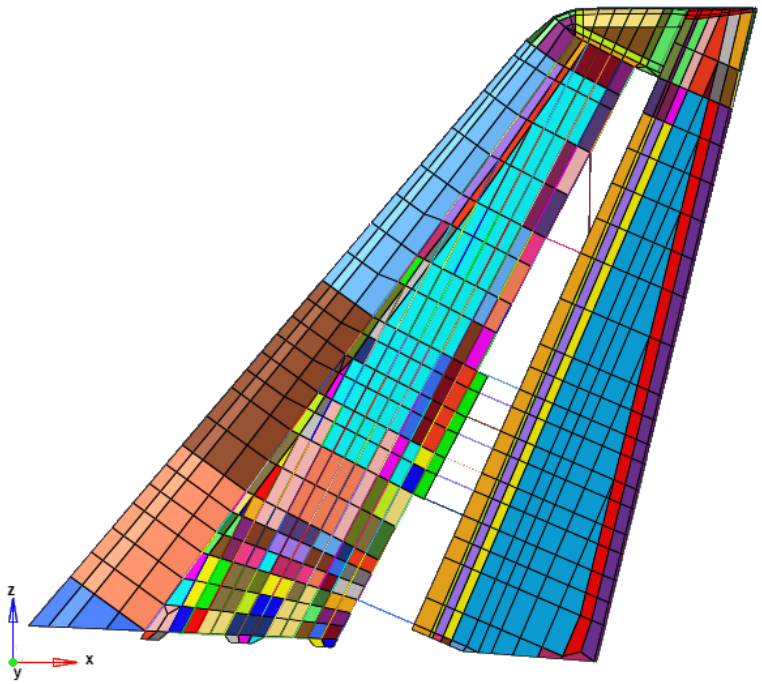

Figure 4.2: GFEM VTP Mesh Used for the Modal Analysis, Without the aft Fuselage. Each Colour Corresponds to a Different Element Property

the modal analysis are slightly higher than the real ones, as the stiffness of the structure is implemented accurately.

However, the difference is correlatable, given that the difference in mass is known. Moreover, in reality, the eigenfrequencies also change depending on other integration factors, such as the play of the hinge bearings. Depending on their tolerance, the natural frequencies can vary up to 23%. Since the accurate dynamic response is not part of this study's scope and from experimental results, it is known that the difference is within acceptable margins, the modal analysis is a good indicator of whether one of the concepts would imply drastic response alterations and be unfeasible from the beginning.

The results of the modal analysis are presented in Table 4.7 for the first five natural frequencies, including the current rudder design, and the maximum relative difference compared to the current rudder. In case a new mode is introduced in the structure, the relative error is not computed since the concept does not meet the requirements.

Concept	f_1 [Hz]	f_2 [Hz]	f_3 [Hz]	f_4 [Hz]	f_4 [Hz]	Δmax
Original	26.0	29.4	34.4	42.2	43.3	-
A	26	28.7	33.8	42.2	43.6	2.44%
B	25.9	27.7	33.2	42.2	43.6	6.14%
C	22	26	28.5	33.6	42.2	New mode

Table 4.7: Natural Frequencies

The biggest changes were expected for concept B, due to the local separation between the rudder shells and spar in the area of the actuators, with the possibility of posing new modes as well. However, the maximum relative change is below the set threshold for the preliminary design, 7%, with no new modes introduced.

The positive modal analysis results for concept B might be due to the connection between the spar-box and shells which is relatively close to the spar. To confirm this assumption, some extra simulations are performed.

Firstly, a new modal analysis has been conducted, with the box-shell common grid points (modelling the interface between the spar-box and the shells) moved one row more aft, towards the trailing edge, as depicted in Figure 4.3. This change has indeed led to a new mode introduction, as anticipated, at a first eigenfrequency equal to 21 Hz.

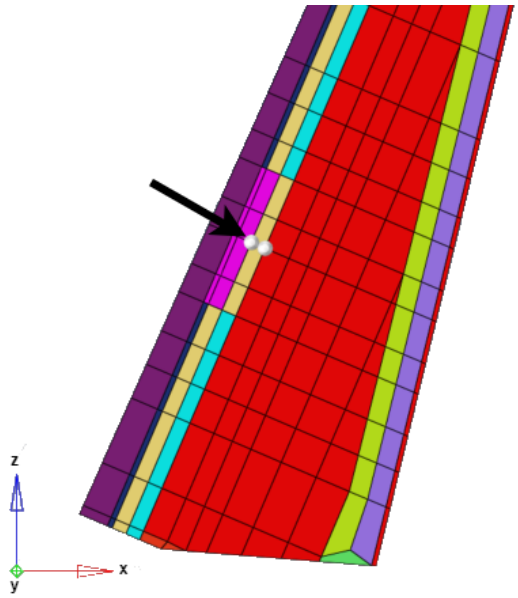

Figure 4.3: Updated Shell-box Connection Nodes for the Decoupled Concept, Moved one Row More Aft than in the Initial Modelling Depicted in Figure 3.21

Thus, it can be concluded that, as expected, the spar-shell decoupling in the area of the actuators leads to stiffness alterations, but by keeping the connection between the spar-box and the shells closer to the spar web, the change is mitigated. In order to keep the rudder's stiffness and natural frequency change within allowed limits, the shear joint between the box and the shells has to be as close as possible to the spar web (and consequently to the actuators).

Moreover, if the modelling of the decoupled concept is correct, changes in the rudder's bending stiffness should be present in the area of the actuators. This would be reflected by the difference between the observed y-displacements in the decoupled and original rudder concepts, resulting from a load applied in the y-axis.

For this assessment, the rudder FEM mesh is isolated for both the original and decoupled concepts (including the spar, the brackets and the spar-box for the latter one), applying only SPCs (with the enforced displacement equal to 0) as boundary conditions at the tips of the

10 brackets. A unit point force is applied in the y-direction at the rudder trailing edge at the location of the second actuator, as illustrated in Figure 4.4.

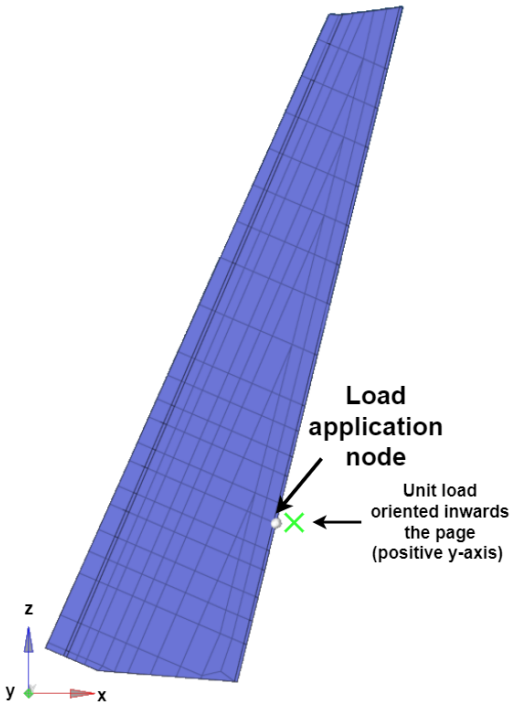

Figure 4.4: Properties of the Reinforced Shells

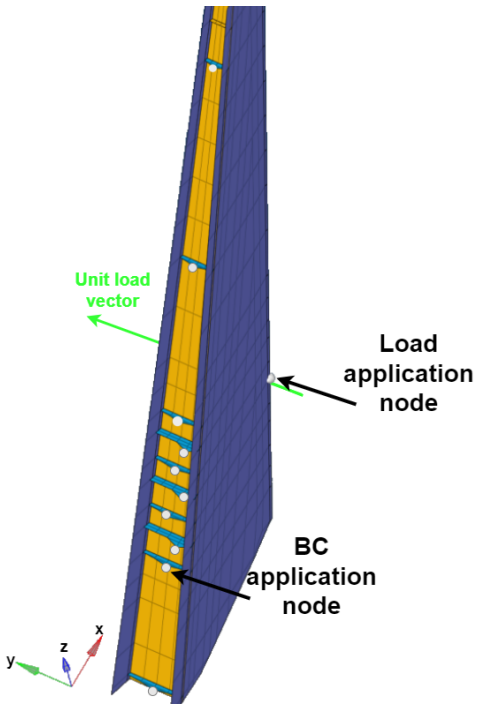

Figure 4.5: Properties of the Unreinforced Shells

For the actuator brackets, the first degree of freedom (transaltion in x-direction, in the rudder coordinate system) is constrained, as the actuators provide stiffness mainly in the x-direction (the force balancing the rudder hinge moment). For the hinge brackets, the first and the second degrees of freedom (transaltion in the x and y-direction) are constrained, as the hinge arms are the main y-load carriers. The boundary condition application nodes can be visualised in Figure 4.5 The displacements obtained at the monolithic leading edge (LE) in the area of AC2 and trailing edge (TE) node where the unit load is applied are shown in Table 4.8.

Concept	LE Displacement [mm]	Δ	TE Displacement [mm]	Δ
Original	0.61	-	2.70	-
B	0.84	38%	4.78	77%

Table 4.8: Displacement Comparison at the Leading and Trailing Edge Nodes at AC2, Where the Unit Load is Applied Between the Current (Original) Rudder Design and Concept B Shell

The results indicate, as expected, a relatively big difference in displacements (and implicitly bending stiffness). Since higher trailing edge displacements do not affect the rudder design at this stage and the structure behaves as expected while still meeting the natural frequency requirements, concept B is deemed viable. However, if the decoupled concept is pursued,

the displacements at the leading edge should be checked and should not exceed the current maximum displacement by more than 2 mm, as the clearance between the rudder monolithic leading edge and the fin rear spar is very small when the rudder is fully deflected. As concept B just meets the natural frequency and mode shapes requirements, it is evaluated with a 3, just sufficient.

Based on the high strain results, significant changes in the eigenmodes were also expected for the truss concept, corroborated by the modal analysis, which indicates the introduction of new modes. Hence, concept C is also not feasible from the perspective of modal analysis, being awarded a score of 1. Given the relatively small changes in eigenfrequencies for concept A, it is evaluated as good and is assigned a score of 4 in the trade-off.

4.2.4 Weight

Since the geometry of the spar-box is the same for all concepts during the trade-off, the impact on the weight of the other implied rudder changes can be assessed. At this design point, the actual rudder weight does not represent a problem, since the designs are not weight-optimised.

The preliminary weights are given in Table 4.9 per component, as calculated by the FEM software, based on the provided densities, emphasising the importance of comparing the entire rudder and not only the spar-box against the current reinforcement since weight differences are also observed in brackets.

The shell weight is separated from the reinforcement, which in the original version is represented by the additional 0° layers and for the other concepts is represented by the spar-box. The brackets' weight includes both the hinge brackets and actuator brackets, differences being caused solely by the actuator brackets since the metallic hinge brackets retained the original design and material.

Concept	Shell [kg]	Reinforcement [kg]	Brackets [kg]	Spar [kg]	Total [kg]
Original	43.7	8.5	7.5	8.3	68
Concept A	43.7	12.8	6.1	8.3	70.9
Concept B	43.7	12.8	6.1	8.3	70.9
Concept C	43.7	20.5	7.5	8.3	80

Table 4.9: Concept Weights per Structural Rudder Component

Table 4.9 indicates that locally extending the monolithic area in the actuator region for concept B does not lead to rudder shell weight modifications. Moreover, the material change of the actuator brackets from metallic to composite leads to weight reductions.

Given that with a slightly higher weight of the reinforcement, the reserve factors are slightly lower compared to the ones pertaining to the current rudder design (1.23 compared to 1.27), concepts A and B are perceived to be between sufficient and good, being awarded a score of 3.5.

Once more it can be seen that concept C does not meet the design requirement, given that the reserve factors are below 1 even if very stiff (and subsequently heavy) trusses are used in the design. Thus, concept C is rated with 1, which stands for unfeasible.

4.2.5 Manufacturing& Assembly and Reparability& Inspectability

The two criteria have been assessed based on experience, and are quantitatively assessed. From the manufacturing&assembly perspective, none of the concepts poses any killer difficulties, as separating the spar into four components does not lead to major difficulties in assembly. Hence, all three concepts pose a good manufacturing& assembly viability.

However, for concept B, extra steps would have to be taken during the shell manufacturing, since the monolithic overhang area is extended only in the region of the actuators, and for concept C, the addition of insulating glass fibre between the metallic brackets/ trusses and composite spar-box to avoid galvanic corrosion involves additional tasks compared to concept A. For these reasons, concept A is rated with 4.5 and concepts B and C are rated with 4.

Regarding reparability& inspectability, concepts A and B have equal performance, deemed to be sufficient, as repairing and inspecting the spar-box structure, which is hidden by the shells, could be lucrative due to the necessity to remove and reinstall rivets, but not unfeasible, awarding a score of 3.5 to the two concepts.

On the other hand, based on experience accumulated by operating the A380, metallic truss structures, which are inaccessible due to the closed nature of rudder shells and spar assembly, can not be accurately assessed, leading to higher maintenance costs. For this reason, concept C is assigned a score of 2.5, as ways to improve inspectability should be found to ensure the concept's viability.

4.3 Trade-off Results

Based on the methodology and scales presented in section 4.1, the criteria are assessed with the trade-off summary and result table presented in Table 4.10, based on the score designation detailed in the previous section.

Criterion	Weights	Concept A	Concept B	Concept C
Strain	0.29	3.5	3.5	1
Load Transfer	0.19	4	4	1
Aeroelasticity	0.19	4	3	1
Weight	0.19	3.5	3.5	1
Manufacturing & Assembly	0.07	4.5	4	4
Reparability & Inspectability	0.07	3.5	3.5	2.5
Total	1	3.76	3.54	1.32

Table 4.10: Final Trade-off Matrix

Even though the proven unfeasibility of only one criterion suffices to exclude one concept, model C has been evaluated for all criteria, in order to emphasize the choice of not further searching ways to improve the concept. The highly stiff rods did not match the performance

of the web in maintaining the current strain levels in the rudder shells, the natural frequencies and the weight of the VTP. Adding more trusses would only increase the already high mass of the spar-box, hence different truss geometries are not further pursued.

Due to the metallic nature of the trusses, inspectability is also not facilitated. Thus, it becomes clear that for the current aim of the study to enable the external-internal load separation, the actuator brackets shall be made out of composite and the connection between the brackets and spar-box top shall be accomplished by the use of composite webs. They provide stiffness and guide the internal loads in the spar-box instead of the rudder shells.

As concept C will not be further developed, the focus is shifted to concepts A and B. Initially it was deemed that the structural de-coupling would lead to new eigenfrequencies and modes, alongside with high loads, unable to be handled by a shear joint. However, the analyses showed that a connection between the spar-box and shells close to the actuator brackets (around the rudder spar flanges) renders concept B viable, scoring close to concept A at the end of the trade-off.

Given that both load separation principles are viable based on preliminary calculations, both concepts A and B are further optimised for weight reduction. Eventually, the concept that better reduces the weight of the spar-box can be identified.

Chapter 5

Local Torsion Stiffening Spar-box Concept Optimisation

In the optimisation stage of the selected concepts, the possibility of reducing the spar-box weight is investigated. The spar-box geometry modelled for the trade-off represents the starting point of the optimisation and the final numerical values of the design variables are determined for an optimised weight.

The current chapter focuses on the optimisation of the local torsion stiffening concept. It commences with the final choice of the spar-box span in section 5.1, which is straightforward compared to the computation of the other variables, mainly due to the FEM results presented in the previous chapter. The optimisation process will thus focus solely on the spar-box height, box-top shape and thickness.

An analytical method that analyses the shear flow in a "box within a box" geometry due to torsional loads is derived in section 5.2, adapting the method originally developed for conventional aerospace multi-cell structures [48]. The analytical equations enable the identification of the variables' impact on the shear flow and hint towards the results' sensitivity to the design variables, rendering an unautomated parametric study a more suitable optimisation approach than, for example, an automated scheme or a design of experiment study [2], [40].

An unautomated parametric study was preferred over an automated one due to the time required to develop a converging automated framework, with the appropriate initial guess and definition of the design space. Nonetheless, this thesis provides the basis for future work which can include an automated optimisation of the spar-box, as its structural behaviour is understood. Moreover, a design of experiment study would be suitable to supersede a trial and error study method in case the variable influence on the structural performance is not known, which for this thesis is not the case, due to the availability of analyitical equations.

An analysis of the box height, top shape and thickness is performed in section 5.3, which enables a first modelling of a more realistic box geometry, that incorporates the clearance required to account for the shell core thickness. Lastly, the check for buckling is performed in section 5.4 and the final design with the minimum reserve factors for each rudder component is provided in section 5.5.

5.1 Spar-box Span Optimisation

The first variable that can be numerically defined based on the FEM results obtained during the trade-off and common sense is the spar-box span. The preliminary simulations performed for the concept trade-off showed that the spar-box webs play a significant role in redirecting the jamming loads into the spar-box and alleviating the rudder shell strains. Thus, as any of the three actuators could jam, all three spar-box webs are needed in the spar-box design and consequently, the minimum box span is equal to the distance between AC1 and AC3.

Increasing the span of the box could lead to further reductions in strain levels but at the cost of additional weight. Given that the trade-off simulations resulted in rudder shell reserve factors higher than 1, it is sensible to set the span to its minimum possible value, to mitigate the weight.

However, a small study is performed to investigate the effects of extending the spar-box span on the minimum rudder shell reserve factors, providing supporting evidence to confirm the efficiency of the spar-box webs in decreasing the strains in the rudder shells and re-directing the jamming load in the spar-box.

The box span is extended to the two neighbouring hinge arm brackets below AC1 and above AC3, which are BR3 and BR5 respectively (see Figure 2.2), leading to two designs, which can be visualised in Figure 5.1. The figure on the left shows the span elongation without the addition of webs that connect the hinge arm brackets and the box top, providing the possibility to investigate the ability of a geometry with open ends to reduce the strains in the rudder shells. On the other hand, the design depicted on the right includes webs that connect the hinge arm brackets and the spar-box roof. The thickness of all spar-box components is kept at 4.9 mm and the trade-off height of 500 mm is retained.

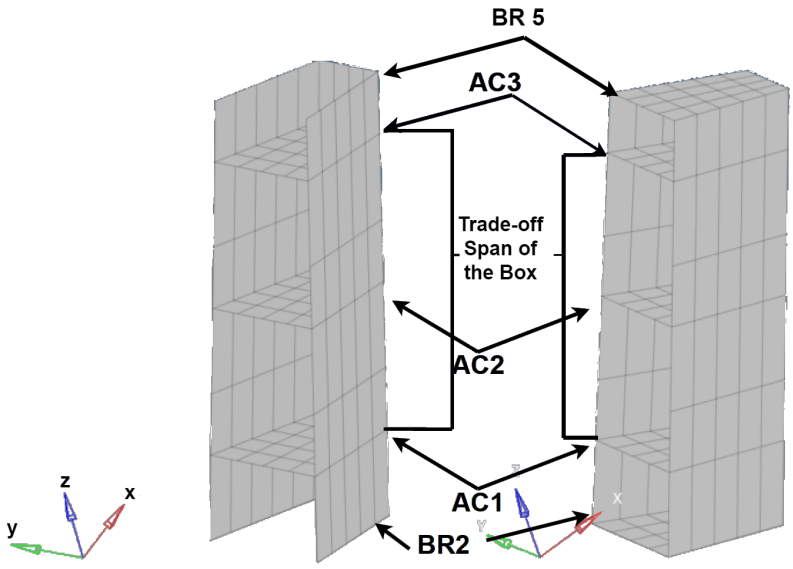

Figure 5.1: FEM Mesh of the BR2 to BR5 Extended Span Box Concepts. On the Left the Concept Without BR Webs and on the Right the Concept With BR Webs

The corresponding rudder shell minimum reserve factors are given in Table 5.1, resulting from static analyses. All minimum reserve factors occur for the same load case, LC-03-01-01 (one

engine out, AC1 jammed at 80°C), and arise in the same element, ramp area (third row) right above AC1 on the left-hand side, as expected, given the jamming load introduction point. The relative reserve factor difference Δ recorded in Table 5.1 is always computed with respect to the results corresponding to geometry of the torsion stiffening concept used in the trade-off.

Concept	Mass[kg]	$\frac{\varepsilon_{XX}}{\varepsilon_{XX,allow}}$	$\frac{\varepsilon_{YY}}{\varepsilon_{YY,allow}}$	$\frac{\gamma_{XY}}{\gamma_{XY,allow}}$	RF	Δ	Location
Trade-off	12.4	0.14	0.01	0.81	1.22	-	Ramp Above AC1
Without BR webs	14.2	0.07	0.08	0.65	1.52	24.6%	Ramp Above AC1
With BR webs	16.5	0.04	0.07	0.56	1.76	44.3%	Ramp Above AC1

Table 5.1: Rudder Shell Minimum Reserve Factors for LC-03-01-01

Given the symmetrical increase in span, it is not surprising that the location of the minimum factors did not change. As expected, both designs further mitigate the strains in the rudder shells, the addition of webs leading to even bigger reductions. However, just the simple span increase, with the spar-box ends open, provides a significant reserve factor decrease of 24.6%, for a lower mass addition compared to the concept incorporating the BR webs.

Considering the unavoidable weight penalties, the original spar-box span between AC1 and AC3 is kept. However, knowing that the simple spar-box span extension can entail reserve factor mitigations as high as 24% could be used in future design iterations. Note that the current reinforcement (of the original rudder shells) extends span-wise beyond the actuator brackets.

5.2 Analytical Method

In order to identify the most important design variables and their influence on the rudder shell shear strain, which is the most important sizing parameter for the spar-box, an analytical approach that characterises the shear flows due to torsion in a ”box within a box” design is developed. Since the shear strain is directly linked to the shear flow, the method will limit to the shear flow characterisation and represent an adaption of the multi-cell shear flow analysis [48].

The method is meant to provide a hint regarding the spar-box design variables' influence on the shear flow distribution in case of system failure. Identifying the most important spar-box design variable could ease the optimisation process.

Considering both the fact that deriving an accurate analytical method that computes the shear flow is not the aim of the study and that the rudder shells can take alone the aerodynamic loads, for the analytical assessment, only the torsional loads that would be induced by the system failure are considered. The contribution of the aerodynamic loading to the shear flow characterisation would not add value to the study regarding spar-box variable influence on the shell shear flow, it would only make the analytical shear flow calculations numerically more accurate [5], which is not pursued in the current study, due to the availability of the GFEM model.

The major assumption for the shear flow equation derivation is that in the sandwich structure, the two carbon face sheets are the main load carriers, and consequently the shells can be idealised as thin-walled structures [25]. Moreover, due to the small dimension of the sandwich ramp compared to the overall shell size and lack of impact on the spar-box variable contribution, the thickness of the shell face sheets is considered constant throughout its entire length, neglecting the local thickness difference in the first 10 cm with 2 extra fabric layers.

As the core has very low strength and its main role is to increase the moment of inertia for buckling considerations, by placing the face sheets away from the neutral axis [25], the core height is included in computing the moment of inertia of the shells only. Hence, the thickness of the sandwich structure considered in the shear flow calculations is equal to the thickness of the two fabric face sheets. Another equally important assumption is represented by the fact that the twist of the box, modelled as a trapezoidal structure, is equal to the twist of the structure enclosed by the rudder shells, modelled as a triangle, as depicted in Figure 5.2.

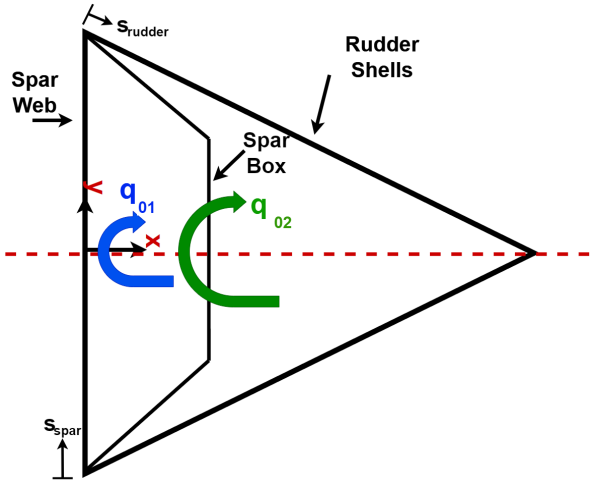

Figure 5.2: Structural Idealisation of The Rudder Shells and Spar-box in the x-y Plane for the Analytical Derivations, at a Certain Span-wise Location

The total torque T introduced at any span-wise location for the torsion stiffening concept by the actuator jamming in each box, which is dependent on the enclosed area A and shear flow due to torsion q_0 (the 0 subscript indicates the shear flow is induced by torsion loading and not shear forces, e.g. aerodynamic loading), is stated in Equation 5.1, where the subscript 1 refers to the spar-box and the subscript 2 defines the rudder shells geometry. The summation of the two torques adds up to the total applied torque, as stated in Equation 5.2. The only variable that has an impact on the shear flow distribution due to torsion q_0 is the spar-box enclosed area A_2, as the enclosed area by the rudder shells A_1 is known and fixed.

$$\begin{cases} T_1 = 2A_1 q_{01} \\ T_2 = 2A_2 q_{02} \end{cases} \tag{5.1}$$

$$T = T_1 + T_2 \tag{5.2}$$

Hence, the shear flow in the spar-box q_{01} can be expressed as a function of the shear flow in the rudder shells q_{02}, as expressed in Equation 5.3.

$$T = 2A_1 q_{01} + 2A_2 q_{02} \rightarrow q_{01} = \frac{T - 2A_2 q_{02}}{2A_1} \tag{5.3}$$

Moreover, the twist assumption can be visualised in Figure 5.3. The spar-box and the rudder shells rotate by the same amount θ around the shear center of the assembly, which lies somewhere on the symmetry axis (the determination of its exact location along the x-axis is not relevant for the current equations).

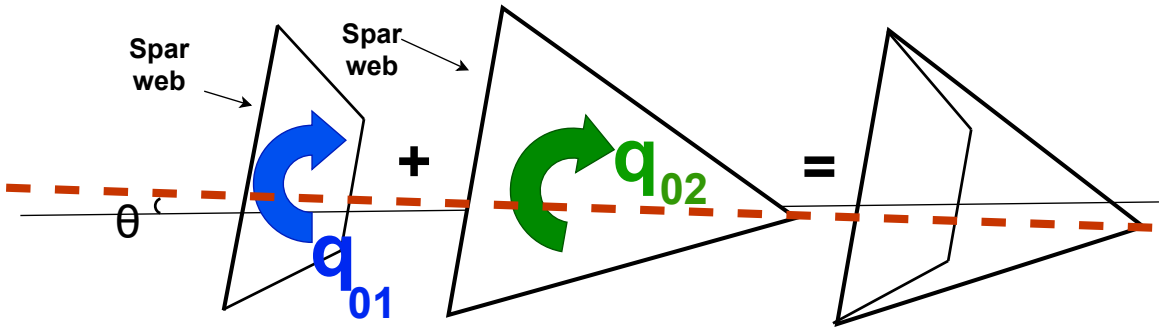

Figure 5.3: Structural Idealisation of The Rudder Shells and Spar-box in the x-y Plane Emphasizing the Twist Definition, at a Certain Span-wise (z-coordinate) Location

The twist of each box is expressed in Equation 5.4 as a function of the enclosed area A and the line integral of the shear flow due to torsion q_0, component thickness t and material shear modulus G, with respect to the component length ds. In each equation, the spar web thickness is the same, 3.5 mm, and the shear flows resulting from the box and rudder expressions are superimposed on the spar web. Considering that both boxes are attached to the spar, the twist compatibility condition is stated in Equation 5.5. The twist condition introduces new dependencies on the thickness and shear modulus.

$$\begin{cases} \left(\frac{d\theta}{dz}\right)_1 = \frac{1}{2A_1} \oint \frac{q_{01} ds}{t_{s1} G_{s1}} \\ \left(\frac{d\theta}{dz}\right)_2 = \frac{1}{2A_2} \oint \frac{q_{02} ds}{t_{s2} G_{s2}} \end{cases} \tag{5.4}$$

$$\left(\frac{d\theta}{dz}\right)_1 = \left(\frac{d\theta}{dz}\right)_2 \tag{5.5}$$

Substituting Equation 5.3 and Equation 5.4 in Equation 5.5 enables the derivation of a formula describing the shear flow q_{02} due to jamming-induced torque in the rudder shells stated in Equation 5.6, where the line integrals can be expressed as a sum due to the constant thickness in each component, where cursor j corresponds to the rudder shells geometry and cursor i is assigned to the spar-box geometry.

$$q_{02} = \frac{T}{2\left(A_2 + \frac{A_1^2}{A_2} \frac{\sum \frac{ds_j}{t_j G_j}}{\sum \frac{ds_i}{t_i G_i}}\right)} \tag{5.6}$$

By performing further simplifications on Equation 5.6, the influence of the spar-box variables can be emphasized. Considering the fixed rudder shell planform dimensions, the terms involving the shell enclosed area A_2, lengths (ds_j), thicknesses (t_j) and shear moduli (G_j) can be substituted by constants (denoted by c). Moreover, the thickness of all spar-box components can be assumed constant for the beginning. Even though the spar-box material shear modulus can vary due to different thicknesses, placing the fibres mainly at 45° leads to a more or

less value of 45 MPa. Hence, Equation 5.6 can be simplified to Equation 5.7, where p_1 is the perimeter of the spar-box. The constants are expressed in Equation 5.8, Equation 5.9 and Equation 5.10.

$$q_{02} = \frac{T}{c_1 + A_1^2 \cdot \frac{c_2}{c_3 + \frac{p_1}{t_1 G_1}}} \tag{5.7}$$

$$c_1 = 2A_2 \tag{5.8}$$

$$c_2 = \frac{2}{A_2}\left(\frac{l_{shell}}{t_{shell}G_{shell}} + \frac{l_{spar}}{t_{spar}G_{spar}}\right) \tag{5.9}$$

$$c_3 = \frac{l_{spar}}{t_{spar}G_{spar}} \tag{5.10}$$

As it can be seen from Equation 5.7, the area of the spar box has a bigger effect on the shear flow compared to the thickness, which also indicates that slight differences between component thicknesses do not influence the results as much as the enclosed area does. Hence, the optimisation should focus first on the effect of the enclosed area on the rudder shell shear strain, influenced mainly by the box height and shape. Substituting the height in the enclosed area and perimeter does not yield an equation that better predicts the shear flow distribution, as it results in an inverse function of a polynomial of degree 4, which can not be further simplified.

Moreover, an analytical study on variable influence plays a major role in deciding whether an automated optimisation scheme or unautomated parametric study is more suitable. In the absence of an analytical method, the variable impact on the results can not be easily predicted, thus an automated design of the experiment is more suitable [22]. However, with an analytical method and an understanding of the variable influence on the results, an unautomated parametric could be faster to implement and understand the structural behaviour of the spar-box in the context of the VTP GFEM. Due to the availability of the verified and validated VTP GFEM with nodal loads accurately computed, the analytical method is not extended and implemented for the aerodynamic loading as well, as it would not be time-efficient.

5.3 Local Torsion Stiffening Spar-box Concept Optimisation

This section describes the unautomated parametric study process for the box height, top shape and component thicknesses. First, a sensitivity analysis on the box height and top shape is conducted in subsection 5.3.1, as the two variables directly affect the enclosed area, which has been identified as the most impactful parameter.

Subsequently, a more realistic spar-box shape is created in subsection 5.3.3, by taking into account the required geometrical clearance with respect to the rudder shells. Finally, the final simulations conducted to determine the final height, top shape and thicknesses are described in subsection 5.3.3.

5.3.1 Spar-box Height, Shape and Thickness Parametric Study

Considering that the shear flow is mostly influenced by the spar-box enclosed area as indicated by Equation 5.7, first, a study on the spar-box height and top shape has been performed

with the trapezoidal modelling of the box used for the trade-off, before modelling it more realistically.

The reason is represented by the simplicity of generating different FEM models for this geometry. Since these variables have a direct impact on the shear flow (and thus shear strains) by only affecting the enclosed area, any subsequent geometry, targeting the same enclosed area, should produce the same shear strains in the shells. Hence, a good first height prediction can be made for the updated box design.

Regarding the spar-box shape, it is clear that the enclosed area, bounded by the rudder shell planform design, has to be maximised, leaving little room for spar-box shape variations. Given the limited space due to the fixed rudder planform geometry (essentially the triangular shape depicted in Figure 5.2), the only shape variance that could have an impact on spar-box weight and rudder shell strains (due to the direct influence on the enclosed area) is represented by the shape of the roof of the spar-box. Thus, the influence of curving the top of the box is also studied alongside the height.

The simulations have been conducted by initially keeping the thickness of the spar-box components constant, 4.9 mm, unchanged from the trade-off analysis. The height is varied between 550 mm, the one used for the trade-off (also of the booster area of the current design) and 200 mm, when a reserve factor below 1 occurred for the model with the straight roof.

The static simulations with height change steps of 50 mm have been performed for both the straight and curved top shapes, for the same height, the two generic models being depicted in Figure 5.4. The left-hand side depicts the straight-top design and the right-hand side illustrates the curved-top design, which has been obtained by confining a circle arc in the top row of elements corresponding to the straight-top design.

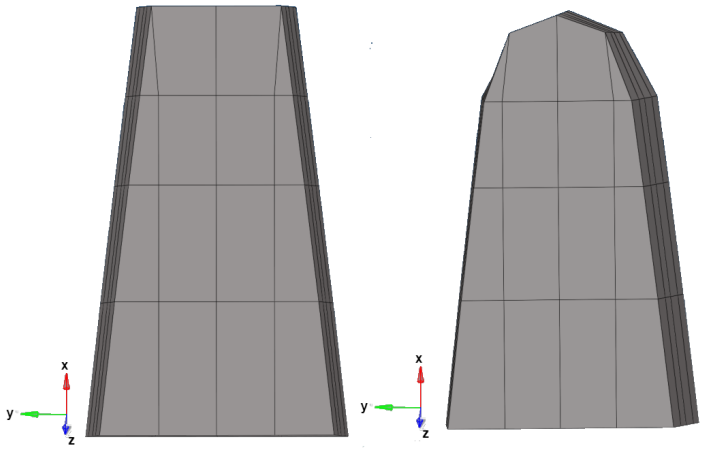

Figure 5.4: Generic Shape and FEM Meshing of the Two Box-top Shapes Used in the Sensitivity Analysis

By varying the spar-box roof shape for the same height, the sensitivity of the rudder shell minimum reserve factor to small changes in the enclosed area will be identified. By assigning the same area for the two different cross-sections, the results are not expected to vary.

Due to the triangular profile defined by the rudder shells that constitute the boundaries for the spar-box width, increments in spar-box height result in smaller and smaller added profile

areas. Each extra row of elements (row insertions performed from the leading edge towards the trailing edge of the rudder) adds a smaller area compared to the one corresponding to the row of elements below. Thus, it is expected that for a certain critical height, further augmentations will not lead to major changes in shear strain and subsequently, rudder shell reserve factors.

Figure 5.5 illustrates the rudder shell reserve factor results for the two box-top geometries, as obtained from the static FEM simulations, keeping the thickness constant at 4.9mm. The individual results are denoted by bullets and are polynomially interpolated to generate the two curves. The interpretation of the results is provided below.

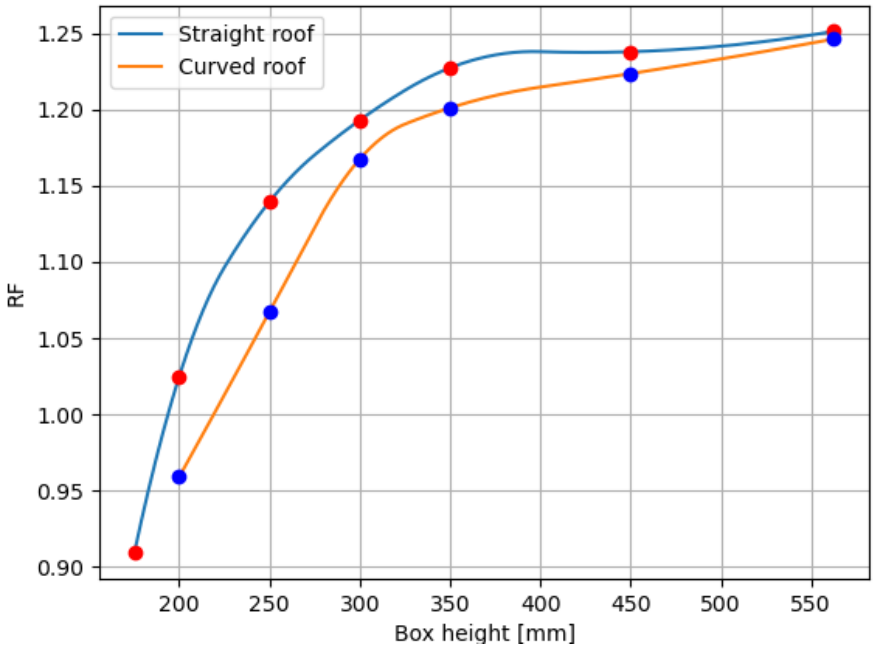

Figure 5.5: Height Influence on Rudder Shell Reserve Factor for Straight and Curved Box-top Shapes

The first observation that can be made is that, as expected, the reserve factors obtained for the curved top shape are consistently smaller than the ones yielded by the straight top design (for the same box height), due to the inherently smaller enclosed area. As the box height increases, the difference in reserve factors between the two models decreases, because the added enclosed area itself and the area differences between the straight and curved roof become smaller and smaller.

For heights above 300 mm (corresponding to an enclosed area of 0.37 m^2), the difference in reserve factors for the two different box shapes is below 1%. However, for heights below 300 mm, the relative difference increases up to 6.5%, due to the higher differences in enclosed areas. Thus, for a height below 300 mm, the box-top shape has more influence on the rudder shell reserve factors and implicitly on the enclosed area, which exhibits the anticipated effect on the results.

For the trapezoidal box, a height of 300 mm (corresponding to an enclosed area of 0.37 m^2) represents also the point where height augmentations do not provide major improvements

in reserve factors, with a relative difference between 0.8% and 2%. The reasoning is still related to the enclosed area, which, with every 5 cm of added height, becomes smaller and less contributing to shear flow being re-directed in the spar-box. For heights below 300 mm, the relative differences in reserve factors caused by 5 cm height changes are as high as 10.7%.

In the case of curved top geometries, an increase in height has the same effect as for the straight-top designs, considering that for heights below 300 mm, the difference in reserve factors is as high as 10.9%. For heights above 300mm, an additional 1% increase in relative difference compared to straight-top designs can be observed, as height augmentations can lead to an increase in reserve factors between 1.5% and 3%.

The impact of height and top shape on weight is also of paramount importance, as its minimisation represents the objective of the current study. Figure 5.6 illustrates the weights of the boxes, where for the same thickness of 4.9 mm, a constant difference of 600-800 g is observed between the straight and curved box-top, the curved top better distributing the area, for less structural weight.

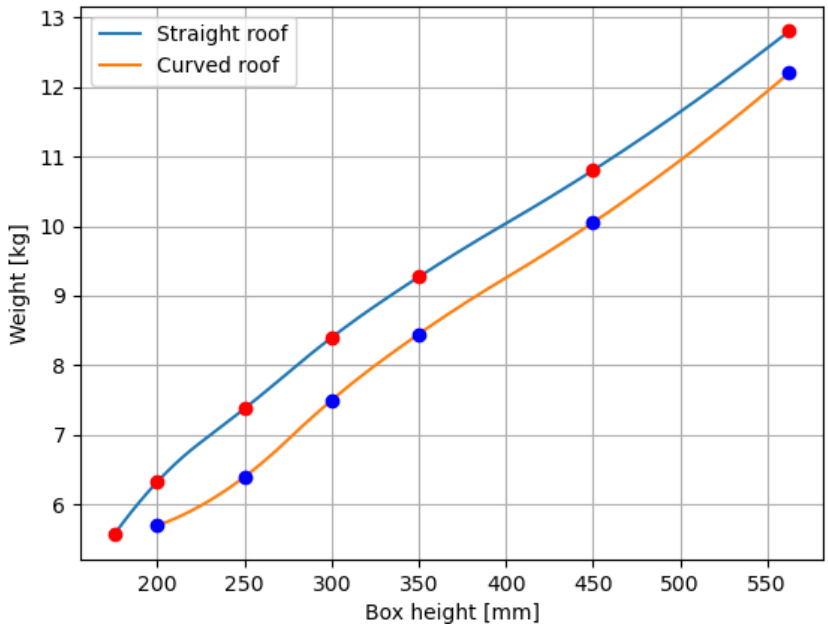

Figure 5.6: Weight Comparison of the Two Spr-box Profile Shapes

However, as Figure 5.5 shows, targeting the height with a reserve factor close to 1 for a box with a straight top and curving it afterwards could eventually lead to reserve factors below 1, requiring an increase in component thickness, which might lead to a weight exceedance compared to the straight box top design.

The simulations repeated for all spar-box components' thicknesses set to 4.2 mm did not alter the reserve factors by more than 3%. Running simulations with all spar-box components' thicknesses set to 3.5 mm resulted in a more abrupt reduction in the rudder shells reserve factors, causing the reserve factor corresponding to the curved top design and 250 mm height to fall below 1, as depicted in Figure 5.7.

Conclusively, by running simulations for different spar-box heights with the two proposed top shapes, it has been discovered that for the assigned width, heights above 300 mm do

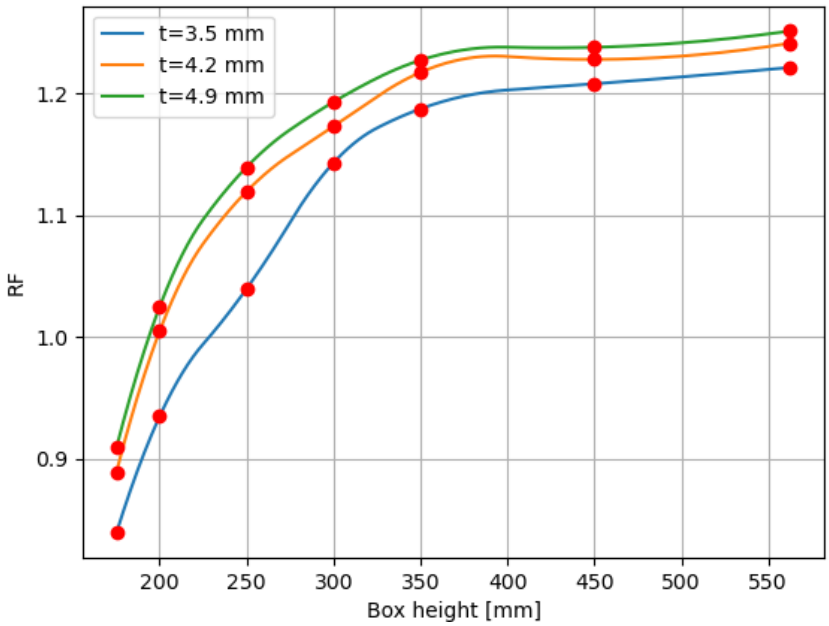

Figure 5.7: Rudder Shell Minimum RFs Corresponding to Straigh-top Spar-Box Design for Different Thicknesses

not entail major improvements in shell reserve factors. Similarly, increasing the spar-box thickness above 4.2mm does not lead to a significant increase in rudder shell reserve factors (differences below 1%), and decreasing the spar-box thickness below 4.2 mm causes more abrupt changes in rudder shell reserve factors (as high as 7%).

However, a more realistic spar-box modelling that accounts for the thickness of the sandwich rudder shells is required, and the insights obtained with the sensitivity analysis form the basis of a good first model prediction. Based on the preliminary sensitivity analysis, the thickness assigned to the updated spar-box geometry is 4.2 mm and is further presented in the next subsection.

5.3.2 Spar-box Updated Geometry

The trade-off has been conducted with the spar-box modelled as a trapezoidal geometry that encloses the entire space between the modelled shells, with no margin between the rudder and box skins. However, the shells have a 30 mm core height and consequently a geometry that better represents the real spar-box and its enclosed area is required, taking into account the space occupied by the shell core, as the current calculations only reflect a concept feasibility demonstration, rather than a proposed design.

By analysing the results yielded by the previous static simulations, it can be observed that the maximum y-displacement of the shells is constantly equal to the maximum y-displacement displacement of the spar-box (displacement discrepancies below 1mm). This indicates that the spar-box does not undergo higher deformations than the rudder shells, which could lead to contact between the two structures.

Thus, from a simulation perspective, there is no need for clearance between the shell geometry

(considering the 30 mm core) and the spar-box geometry, as the spar-box does not undergo higher displacements than the shells. However, to make the design more realistic, a 5 mm clearance is considered while modelling the geometry of the new box, as indicated in Figure 5.8, which could change during detailed design phases.

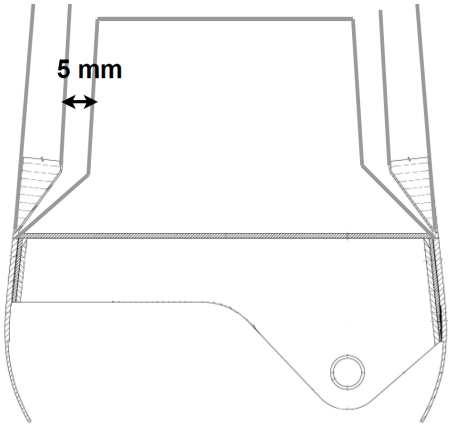

Figure 5.8: Clearance Between the Rudder Shells and Spar-box

With the results of the sensitivity analysis in mind, a first estimate for the height of the updated spar-box model can be computed based on the enclosed area equivalence. The enclosed area for the trapezoidal box with a straight top with a reserve factor of 1.06 with a height of 250mm corresponds to the new geometry with a height of 330 mm. The updated geometry and its mesh are depicted in Figure 5.9 and represent the new starting point for conducting the optimisation.

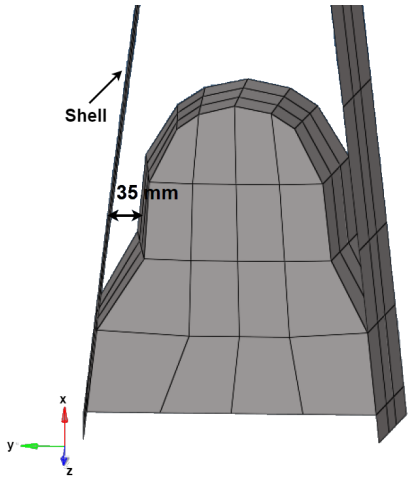

Figure 5.9: Generic Shape and FEM Meshing of the Updated Spar-box Geometry, Emphasizing the Clearance Between the Shells and the Box

Note that simulations have been performed for both curved and straight spar-box top geometries, and initially, the thickness of all spar-box components is set to 4.2 mm, as concluded from the previous sensitivity analysis.

5.3.3 Spar-box Height, Shape and Thickness Optimisation

The FEM results corresponding to the updated spar-box geometry, with a height of 330 mm and all components' thickness set to 4.2, are given in Table 5.2. The sizing load case, one engine out, AC1 jammed at 80°C (LC-03-01-01), and critical element (ramp area, third row, right above AC1 on the left-hand side) have been retained. For comparison, results obtained for a thickness of 4.9 mm are also displayed emphasizing the accuracy in reserve factors obtained for different spar-bow widths but the same enclosed area.

Thick. [mm]	Height [mm]	Top-box Shape	Mass [kg]	$\frac{\varepsilon_{XX}}{\varepsilon_{XX,allow}}$	$\frac{\varepsilon_{YY}}{\varepsilon_{YY,allow}}$	$\frac{\gamma_{XY}}{\gamma_{XY,allow}}$	RF
4.9	330	Straight	7.9	0.06	0.03	0.95	1.05
4.2	330	Straight	6.5	0.14	0.08	0.98	1.01

Table 5.2: Rudder Shell Minimum Reserve Factors for the Updated Spar-Box

With the expected results entailed by the updated spar-box geometry, a simulation with a curved top-box shape has been performed, yielding a reserve factor of 0.99. In this situation, two different changes are performed on the box, to increase the reserve factor above 1.

One simulation is performed by increasing the height by 20 mm while keeping all components thickness to 4.2 mm, resulting in a minimum rudder shell reserve factor of 1.01. This measure leads to a spar-box weight of 6.6 kg.

Another simulation with the thickness increase of one component is attempted, remembering that the thickness is able to alter only in overall increments of 0.7mm, to retain the laminate symmetry. The box-top thickness only has been increased to 4.9 mm, as it has been identified as the lightest component. The static simulation entails a reserve factor of 1.01, for a spar-box weight of 6.1 kg.

The results are summarised in Table 5.3, where it is also indicated that a further decrease in thickness does not lead to spar-box weight mitigation. The results are reported for the same load case (LC-03-01-01) and sizing element, in the ramp area above AC 1.

Top-box Thick. [mm]	Height [mm]	Top-box Shape	Mass [kg]	$\frac{\varepsilon_{XX}}{\varepsilon_{XX,allow}}$	$\frac{\varepsilon_{YY}}{\varepsilon_{YY,allow}}$	$\frac{\gamma_{XY}}{\gamma_{XY,allow}}$	RF
4.2	330	Straight	6.5	0.14	0.08	0.98	1.01
4.2	330	Curved	6.1	0.14	0.08	0.99	0.99
4.9	330	Curved	6.2	0.13	0.08	0.98	1.01
4.2	350	Curved	6.6	0.14	0.08	0.97	1.02
3.5	370	Straight	6.8	0.14	0.07	0.99	0.99

Table 5.3: Shell Minimum Reserve Factor for Different Updated Box Configurations

The results also indicate that for heights below 350 mm, the thickness influence on the shell reserve factor is in the order of magnitude 10^{-2} (e.g. the minimum shell RF changes from

1.06 to 1.01), while the height has an order of magnitude 10^{-1} (e.g. the minimum shell RF changes from 1.16 to 1.06). The validity of the statement is emphasised by the fact that, given that per data point, the thickness and height have been changed in equal relative increments, with thickness relative steps even slightly higher than the height (16.7% for the thickness and 14.3% for the height).

From a static analysis perspective, the final spar-box design for the torsion stiffening concept corresponds to a box height of 330 mm, a box-top thickness of 4.9 mm and other components thickness of 4.2 mm, based on the results presented in Table 5.3. To ensure the feasibility of the concept, the spar-box is subjected to a buckling analysis to confirm the compliance with **REQ-05-DESIGN**.

5.4 Buckling Assessment

This section presents the design check against buckling below the sizing ultimate load for the proposed final spar-box design pertaining to the torsion stiffening concept, to confirm the compliance with **REQ-05-DESIGN**. Since the only requirement is to ensure no buckling occurrence below the ultimate load, the only required output of the buckling analysis is an eigenvalue above 1. Thus, the numerical value of the buckling load is not computed. In subsection 5.4.2 the buckling analysis (SOL 105) set-up is described and subsection 5.4.2 presents the results.

5.4.1 Buckling Analysis Pre-Processing

From the static analysis perspective, the preliminary spar-box shape and thickness that minimises weight have been identified. As a final step, the proposed spar-box design with its corresponding thickness is checked for buckling requirements.

A linear analysis is run due to the material linearity and the goal of the study to provide a preliminary design of the spar-box, as the study is not concerned with post-buckling behaviour. Note, however, that the critical buckling load resulting from a linear analysis is usually overestimated compared to the results produced by a non-linear analysis [3].

The buckling analysis is performed for the load case that entails the smallest rudder shell reserve factor, which is one engine out with AC1 jammed while retracting at 80°C. Even though the spar-box web at AC1 is loaded in tension, it experiences the highest shear load out of all considered subcases. If the buckling behaviour is dominated by compression and not shear, the eigenvalues will be negative and their magnitude is considered to be similar to the positive eigenvalue value that would be obtained if the subcase with actuator extending (loading the web in compression) is run. This is because the rudder loading is very similar, with slightly lower shear and the compressive load of the jammed actuator has the same magnitude as the retracting case.

For the buckling analysis, a more refined mesh is required to conduct reliable buckling load calculations and accurately capture the buckling pattern. To refine the mesh, the spar-box has to be isolated from the rest of the rudder, as the other rudder components are inherently designed against buckling (with high post-buckling factors demonstrated experimentally),

including the shells without reinforcement, given their core height can account for the buckling loads. The original location of the spar-box in the GFEM is kept (thus the coordinates of the nodes) and the surrounding mesh is deleted. In this way, the buckling analysis focuses on the novel structure, whose preliminary design represents the core of the study.

In the first step, the spar-box geometry alone is isolated and the mesh is refined from 96 elements to 11786 elements (majority CQUAD4), out of which only 12 are CTRIA3, at non-critical locations, towards the top of the box, due to the tapered nature of its trapezoidal shape. Another simulation with a mesh size of 7865 elements is run in parallel to confirm the mesh quality, by comparing the relative difference of the output eigenvalues. The mesh size is quite refined, leading to a detailed finite element model (DFEM), but the buckling analysis requires only a few seconds to run. The locations of the original nodes, common to the box and rudder spar in the GFEM, are retained, to facilitate the application of the displacements.

Subsequently, the internal loading of the box has to be reproduced, since the loads acting on the rudder are deleted from the model as the surrounding mesh is removed. The spar-box loading is reproduced by imposing the nodal displacements at the box nodes that were common to the rudder spar and the box in the GFEM, as resulted from the static analysis of the considered load subcase. From the applied displacements, the solver is able to reproduce the internal loading in the box and determine the buckling eigenvalue.

In Figure 5.10 the difference in the number of elements between the coarse (on the left) and detailed mesh (on the right) can be visualised. The resultant displacements in mm of the spar-box obtained with the coarse mesh for the critical load case are shown.

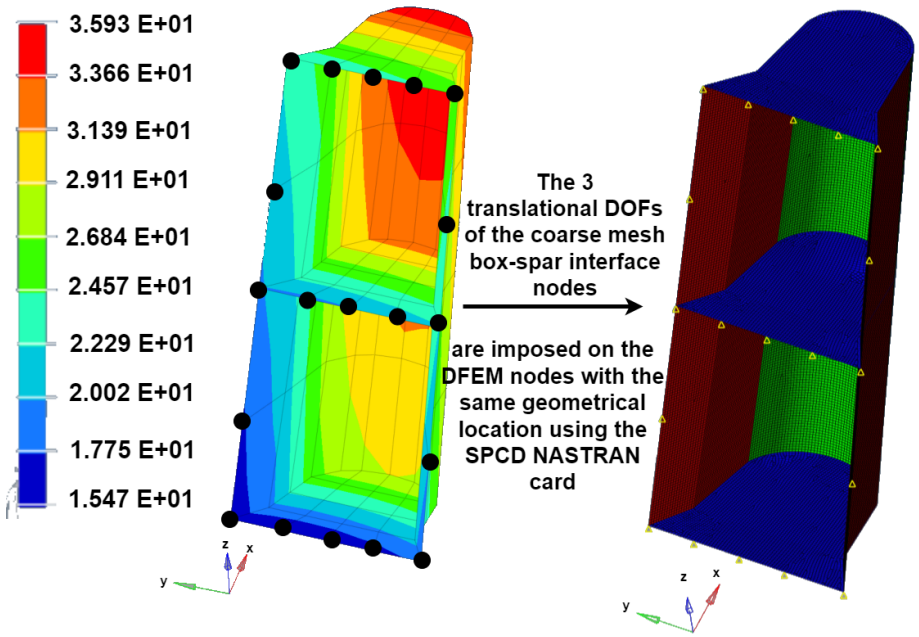

Figure 5.10: On the Left, The GFEM Spar-box Mesh with the Resultant Displacements from the Static Analysis corresponding to the Critical Load Case vs. The DFEM Spar-box Mesh for the Buckling Analysis with the Application of the SPCDs, on the Right

In the first step, the displacements of all the nodes constituting the interface between the spar-box and the spar web, as yielded by the static simulation of LC-03-01-01, are reinforced

on the DFEM nodes with the same location coordinates for the three translational degrees of freedom only[51], as it can be seen in Figure 5.10. The nodes on the GFEM marked with black dots correspond to the DFEM nodes marked with yellow triangles.

The displacement contour shown autoreffig:meshc represents resultants, thus the legend values are positive. However, some of the individual displacement components are negative (since the loading bends the VTP to the left), as the spar-box displacements are also a result of the VTP-fin bending, not only the internal loading of the box. In the DFEM, different mesh colours indicate different PCOMP properties.

The nodal displacements are imposed on the DFEM by utilising the SPCD card [4] (the SPCD card generates the yellow triangles), where the node ID, the degree of freedom and the numerical value of the deformation are introduced. The SPCD card acts both as a boundary condition and a loading.

It represents the boundary conditions because the degrees of freedom for which the SPCD card is created define the type of edge condition. In the current case, since only the translational degrees of freedom are included in the SPCD, the edges are simply supported. Moreover, the SPCDs represent a loading because the magnitudes of the three translational displacements correspond to the resultant loading transferred in the spar-box in the context of the VTP GFEM (only a part of the applied load in the GFEM is carried by the box, as the shells carry the rest).

The rotational displacements could have been added, but by omitting them, the simulation is as conservative as it can be, assuming thus that the edges can not transfer moments [51]. With the edges modelled as simply supported for all rotational degrees of freedom, the buckling pattern is expected to occur closer to the edges.

In the second step, the values of the displacements in mm applied at the retained grid points (as illustrated in Figure 5.10) are interpolated for the new grid points pertaining to the refined mesh. In this way, the boundary conditions modelled by the SPCDs are extended and correctly applied to the entire length of the spar-box edges.

Otherwise, only the SPCDs shown Figure 5.10 would model local, pinned boundary conditions, and the rest of the edges would be free. The interpolation function takes the same form as the nodal shape function and the coordinates of the intermediate nodes are plugged into the shape function to yield their corresponding interpolated displacements.

The displacements retrieved from the coarse mesh are interpolated for the three translational degrees of freedom to extend the SPCD to the other grid points, as depicted in Figure 5.11. Thus, it can be observed that all the nodes in the DFEM that constitute the interface between the spar web and the box have the three translational degrees of freedom constrained and loaded in the form of displacements applied at those nodes with the SPCD card, indicated by the yellow triangles.

To confirm the correct application and interpolation of the displacements modelled with the SPCD card, a static analysis of the DFEM is run in parallel, as the resulting DFEM displacements should match the original displacements, obtained with the coarse mesh. This ensures the correct reproduction of the spar-box loading. Once the SPCDs are applied on the entire spar-box edges and the mesh is checked for free edges, double elements and double grid points, the static and buckling analysis is run. The results of the static analysis run for

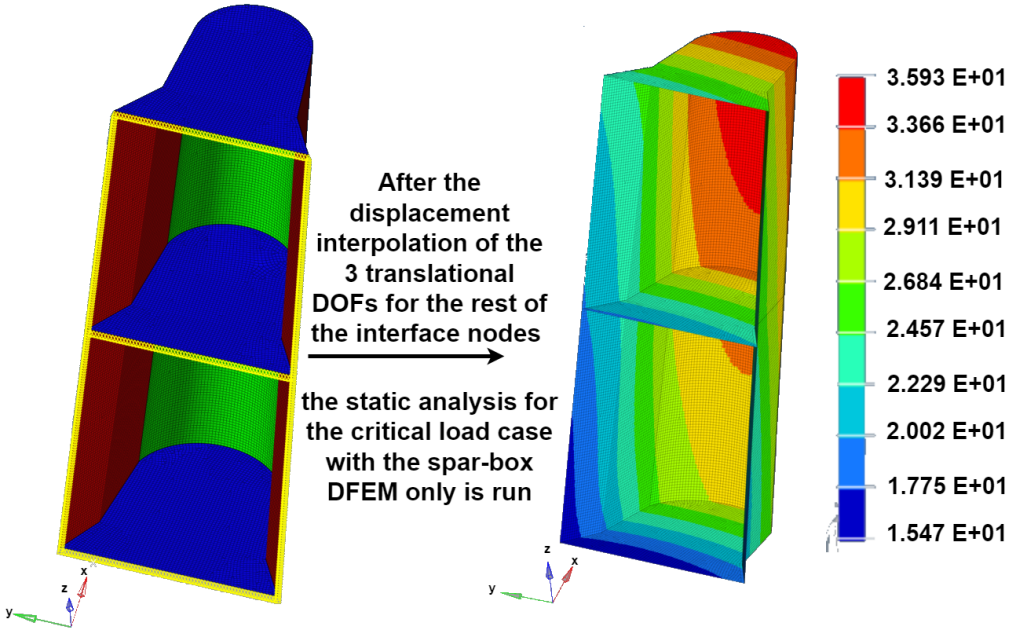

Figure 5.11: The Application of the SPCD on the Entire Spar-box Edges as a Result of Displacement Interpolation vs. The Resultant Displacement Obtained from the DFEM Static Analysis for the Critical Load Case

the critical load case indicate the displacements match, as can be seen in Figure 5.11, with a maximum discrepancy of 0.4%, and the buckling results can be analysed.

5.4.2 Buckling Analysis Results

As the static analysis results confirm the correct application of the SPCDs, the buckling analysis is performed without further modifications. Firstly, the eigenvalues obtained from the model with 8865 elements and 11786 elements were compared. The first eigenvalue computed by the model with 11786 elements is -2.2, with a relative error of 4.4% compared to the results yielded by the model with 7865 elements, with an eigenvalue of 2.3.

This confirms the mesh quality, and the model with 11786 elements will be further used to refer to the buckling analysis results. The first eigenvalue of -2.2 implies that the structure would buckle at a load that is 2.2 times higher than the current load if applied in an opposite direction. Not surprisingly, the first eigenmode occurs in the box web corresponding to the AC1 location, as it can be seen in Figure 5.12, with the buckling pattern close to the edge, due to the lack of boundary conditions in the rotational degrees of freedom.

The second mode occurs at a value of -4.2 in the AC1 box web as it can be seen in Figure 5.12. This is an indicator that the first two modes would be driven by compression if the jamming loads were applied in the opposite direction (jamming while extending), as buckling due to shear would more likely be attributed if the first two eigenvalues would have close magnitudes but different signs [47]. This behaviour can be observed for the fourth mode with an eigenvalue of 5 and the fifth mode with an eigenvalue of -5.9, where the buckling modes resemble the displacement observed for the second mode, but the half-waves have a mirrored shape.

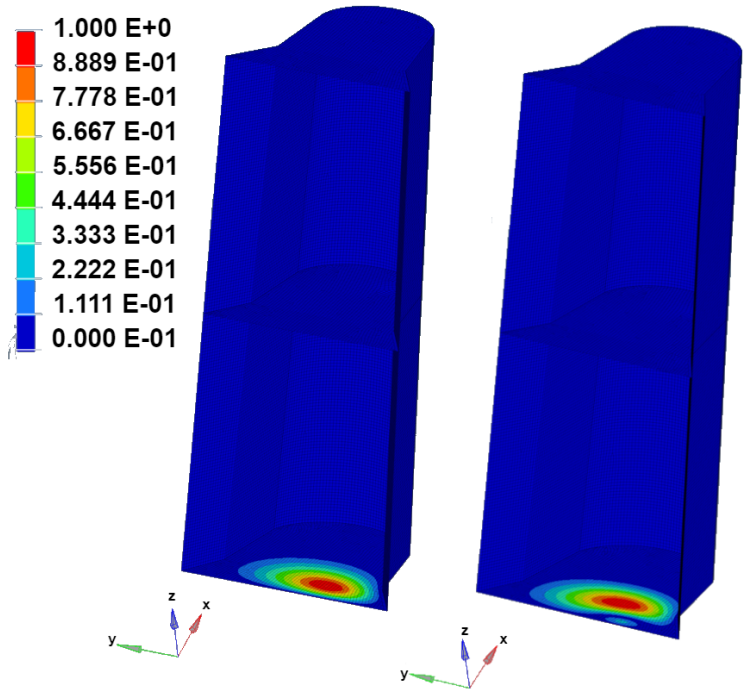

Figure 5.12: Bucklin Mode 1 (Left) and Mode 2 (Right) for the Local Torsion Stiffening Concept

Since the load magnitudes do not differ significantly between LC-03-01-01 and LC-03-02-01, the eigenvalues are deemed representative for AC1 jamming while extending. Thus, with the chosen thickness, the structure will not buckle under the ultimate loads, complying with **REQ-05-DESIGN**.

Conclusively, the buckling behaviour of the spar-box is dominated by the compression induced by the actuator jamming while extending, occurring in the spar-box web of the jammed actuator, in this case, AC1. Furthermore, with the first eigenvalue magnitude above 1 with only the translational degrees of freedom enforced, it is ensured that with the proposed preliminary design, the spar-box will not buckle. In the absence of stiffeners, the response is a global buckling of the web.

5.5 Torsion Stiffening Spar-box Concept Final Design

For the local torsion stiffening concept, a study has been performed on the spar-box height, top shape and thickness effect on the minimum rudder shell reserve factors and weight. It has been concluded that for this spar-box concept, the weight is mitigated for a height of 330 mm and, a curved box-top of thickness of 4.9 mm, while all of the other components have a thickness of 4.2mm. The buckling analysis results indicate that the proposed final design will not buckle under the ultimate loads, complying with **REQ-05-DESIGN**.

Setting all the components to a thickness of 4.2 mm leads to reserve factors below 1 in the shells, and a compensatory increase in height would lead to an increase in weight. The final

box dimensions are shown in Figure 5.13, geometrically maximising the enclosed area given by the boundaries set by the 30 mm core of the shells, and the ramp-down at the base of the spar-box.

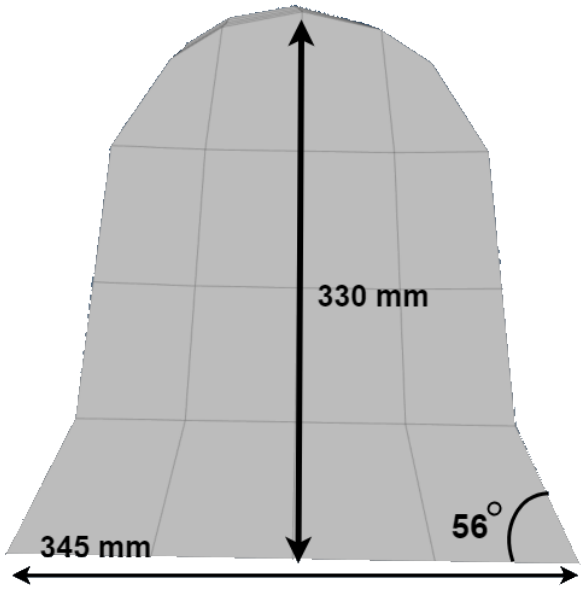

Figure 5.13: Final Dimensions of the Spar-box for the Local Torsion Stiffening Concept shown on the GFEM Mesh

For the straight top designs, higher thicknesses did not result in significant height reduction to meet the requirement of reserve factors above 1, as the thickness influence was in the order of magnitude equal to 10^{-2}, while the height had an influence in the order of magnitude 10^{-1}. During the analyses, the thickness and height were changed in similar relative increments (16.7% for the thickness and 14.3% for the height). For thicker spar-box components, the required height is still close to 330 mm, simply resulting in higher weight.

The final thicknesses and layer sequence are given in Table 5.4 per spar-box component, respecting the lay-up sequence design rules. The final spar-box weight for a rudder shell minimum reserve factor of 1.01 is 6.2 kg, complying with **REQ-01-DESIGN** and **REQ-04-DESIGN**.

Region	Layup	Thickness [mm]
Walls	$[45^\circ_3/0°/45^\circ_2]_s$	4.2
Roof	$[45^\circ_3/0°/45^\circ_3]_s$	4.9
Webs	$[45°/0^\circ_2/45°/0^\circ_2]_s$	4.2
Spar	$[0^\circ_2/45°/0^\circ_2]_s$	3.5

Table 5.4: Spar-box Component Final Layup Sequence and Thickness

Since the design change of the torsion box spar is local, and consequently the overall stiffness of the entire VTP does not change significantly compared to the one observed during the trade-

off process, the modal analysis results run for the final concept does not present significant changes compared to the trade-off results. Thus, the design is compliant with **REQ-02-DESIGN** and **REQ-03-DESIGN**.

The integrity of all rudder components is checked, with the values presented in Table 5.5. For all components, the sizing load case occurred for one engine out conditions with the base actuator AC1 jammed, variations being encountered in temperature only. Due to limit reserve factors recorded for the spar as well, no thickness modifications have been performed for the spar web. Moreover, the von Mises stress in the metallic brackets undergoes alterations below 5%.

Component	Load Case	$\frac{\varepsilon_{XX}}{\varepsilon_{XX,allow}}$	$\frac{\varepsilon_{YY}}{\varepsilon_{YY,allow}}$	$\frac{\gamma_{XY}}{\gamma_{XY,allow}}$	RF	Location
Shells Original	03-01-02	0.09	0.35	0.70	1.27	Ramp Above AC1
Shells Updated	03-01-01	0.15	0.12	0.97	1.01	Ramp Above AC1
Spar Original	03-01-02	0.01	0.11	0.81	1.22	Web at AC1
Spar Updated	03-01-01	0.12	0.14	0.89	1.10	Web at AC1
AC Brackets	03-01-01	0.02	0.15	0.57	1.70	AC1 Attachment
Spar-box	03-01-02	0.20	0.06	0.63	1.51	AC1 Web

Table 5.5: Rudder Components Minimum Reserve Factors

Chapter 6

Decoupled Spar-box Concept Optimisation

This chapter presents the optimisation process and final design of the decoupled spar-box concept, commencing with the general optimisation process in section 6.1. The optimised design for minimum rudder shell reserve factor is checked for buckling in section 6.2, with the final overview of the optimised concept being provided in section 6.3. In section 6.4 the verification and validation tasks performed throughout the study are summarised.

6.1 Decoupled Spar-box Concept Optimisation

This section presents the optimisation process for height, top-box shape and thickness for the de-coupled concept, making use of the insights gained during the optimisation of the local torsion stiffening concept. Thus, subsection 6.1.1 presents modification performed on the rudder shell modelling due to the results obtained from the trade-off and the initial spar-box geometry subjected to the optimisation, being complemented by subsection 6.1.2, which presents the simulations conducive to the spar-box final design.

6.1.1 Pre-Optimisation Concept Updates

Before delving into the spar-box optimisation process, one update is performed on the rudder shells, due to a design weakness indicated by the trade-off results. The shell element with the minimum reserve factor is located in the ramp area above AC1, despite the box attachment to the shells in the area of AC2 only. Hence, the shell monolithic area used for the spar-box attachment is extended to the first elements below AC1 and above AC3 in the first row of sandwich elements, as illustrated in Figure 6.1.

Moreover, as indicated by the trade-off modal analysis, the box-shell connection area is kept close to the spar web, as moving the joint more aft, towards the shell trailing edge, leads to

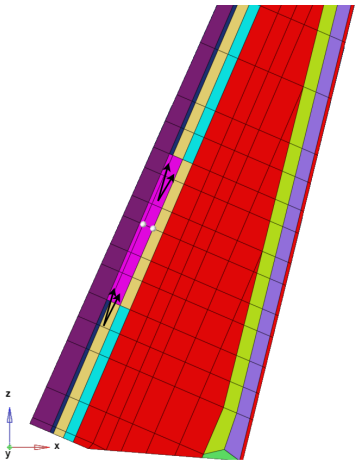

Figure 6.1: Elements Corresponding to the Extended Monolithic Area Properties

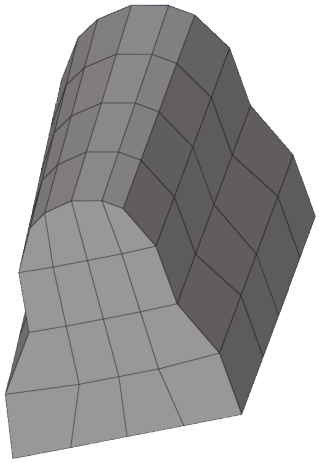

Figure 6.2: Generic Decoupeled Spar-box Shape and FEM Mesh

higher natural frequency alterations due to the local stiffens distribution change provided by the actuators.

Based on the span analysis performed in the previous chapter, the decoupled box will also span only between AC1 and AC3, as the current value leads to reserve factors above 1 in the shells and further augmentations result in a weight increase. The starting design for the optimisation features the spar-box thickness set to 4.2 mm for all its components and a height of 320 mm, based on the insight gained during the local torsion stiffening concept optimisation.

As indicated by the trade-off static analyses, the spar-box maximum displacement is not different from the rudder shell's highest displacement. Hence, similarly to the local torsion stiffening concept, a 5 mm margin between the 30 mm shell core and spar-box is attributed during the box re-modelling, except for the box base, which corresponds to the monolithic region in the shells, where no margin is used.

Hence, the geometry corresponding to the base row of elements has the same width as the spar web, to enable the attachment to the rudder shells, being followed by a row of elements with a 5 mm margin from the shell ramp area, the rest of the geometry having a 35 mm distance from the shell geometry. The generic shape of the decoupled spar-box concept is depicted in Figure 6.2, noting that both curved and straight top-box designs are further investigated.

6.1.2 Optimisation

The insights gained during the design optimisation of the torsion stiffening concept have been used in the decoupled spar-box concept optimisation. As it has been observed that changes in height have more influence on both weight and the rudder shell minimum reserve factor, simulations with different box heights have been carried out with priority, followed

by a component thickness assessment, investigating the reserve factor sensitivity to thickness changes.

The minimum reserve factors for the shells are presented in Table 6.1, where it can be quickly identified that the required box height, for a straight-top design, only extends up to the rudder shell ramp, corresponding to a height of 160 mm. However, curving the geometry of the box-top resulted in a minimum rudder shell factor of 0.99 and increasing the thickness of the box roof only to 4.9 mm did not alter the result.

Top-box Thick. [mm]	AC Web Thick. [mm]	Height [mm]	Top-box Shape	Mass [kg]	$\frac{\varepsilon_{XX}}{\varepsilon_{XX,allow}}$	$\frac{\varepsilon_{YY}}{\varepsilon_{YY,allow}}$	$\frac{\gamma_{XY}}{\gamma_{XY,allow}}$	RF
4.2	4.2	320	Straight	6.3	0.12	0.10	0.84	1.17
4.2	4.2	240	Straight	5.7	0.16	0.10	0.88	1.11
4.2	4.2	160	Straight	4.40	0.13	0.12	0.97	1.01
4.2	4.2	160	Curved	4.06	0.16	0.12	0.98	0.99
4.9	4.2	160	Curved	4.16	0.16	0.12	0.98	0.99
4.9	4.9	160	Curved	4.25	0.14	0.12	0.97	1.01
5.6	6.3	80	Straight	4.40	0.17	0.13	1.01	0.97

Table 6.1: Rudder Shell Minimum RF for Different Box Parameters, LC-03-01-02

Thus, for a curved-box shape, the thickness of the spar-box webs also has to be increased to 4.9 mm which provides a lighter design than increasing the thickness of the spar-box walls) still resulting in a lighter box than the straight-top design. Further increasing the thickness did not enable the height reduction to a value compatible with a lower weight.

The minimum reserve factor element is the same one for all simulations, located in the ramp area above AC 1. Increasing the shell monolithic area and reducing the size of the box lead to a change in the temperature of the critical load case (from 80°C to -54°C) and a shift in the location of the critical element, probably due to the strength of the material and the smaller size of the box. However, the minimum reserve factor still occurs in the weakest sandwich area, the ramp.

Due to the structural decoupling, the jamming loads are not distributed to the shells (only locally at the location of the box-shell connection) as in the case of the local torsion stiffening concept and consequently, the (shear) strains are higher in the decoupled spar-box web of the jammed actuator compared to the local torsion stiffening concept. As the minimum reserve factors of the spar-box fall below 1.05, their values are followed in parallel with the shell reserve factors, Table 6.2 presenting their value per simulation. The element location of the minimum spar-box reserve factor is the same for all simulations, the most-left element in the bottom row of the AC 1 web.

One of the most important aspects revealed by Table 6.2 is the fact that curving the top of the box results in higher reserve factors (and shear strains) in the spar-box, compared to the ones corresponding to the straight-top design. This result is not surprising, as the twist, which is proportional to the shear strain, is dependent on the polar moment of inertia, maximised by a circular profile [48].

Top-box Thick. [mm]	AC Web Thick. [mm]	Height [mm]	Top-box Shape	Mass [kg]	$\frac{\varepsilon_{XX}}{\varepsilon_{XX,allow}}$	$\frac{\varepsilon_{YY}}{\varepsilon_{YY,allow}}$	$\frac{\gamma_{XY}}{\gamma_{XY,allow}}$	RF
4.2	4.2	320	Curved	6.3	0.04	0.12	0.95	1.04
4.2	4.2	240	Straight	5.7	0.04	0.10	0.99	1.01
4.2	4.2	160	Straight	4.40	0.02	0.13	1.01	0.98
4.2	4.2	160	Curved	4.06	0.02	0.13	0.94	1.05
4.9	4.2	160	Curved	4.16	0.02	0.13	0.94	1.05
4.9	4.9	160	Curved	4.25	0.02	0.12	0.94	1.05
5.6	6.3	80	Straight	4.40	0.03	0.13	0.91	1.09

Table 6.2: Spar-box Minimum RF for Different Box Parameters, LC-03-01-02

While the straight-top design with a height of 160 mm and all components' thickness set to 4.2 mm might be feasible from the perspective of rudder shell loading, this design resulted in spar-box reserve factors below 1. Conversely, curving the top resulted in critical results for the shell.

Compared to the local stiffening concept, this concept also emphasises that curving the top of the box not only decreases the box weight but also decreases the strain levels in the spar-box. At the same time, the effects on the rudder shells remain unchanged, increasing the shear strain level.

It also shows that curving has the same effect as increasing thickness. For the same top geometry, increasing the thickness with 2 layers does improve (or alter at all) the rudder shell RFs, while adding weight, and in the case of spar-box the effect of increasing the thickness is equal to curving the top, while the latter one has a positive impact on the weight.

6.2 Buckling Analysis

This section presents the buckling analysis for the decoupled spar-box concept, optimised for the rudder shell minimum reserve factors, and the extended monolithic region in the rudder shells. In subsection 6.2.1 the analysis set-up is described and in subsection 6.2.2 the results are presented.

6.2.1 Buckling Analysis Pre-Processing

The buckling analysis procedure for the decoupled box design is the same as the one described for the local torsion stiffening concept, with the addition of the shell monolithic area buckling assessment, which is a design alteration performed to accommodate the decoupled spar-box concept. The loading corresponds to the load case with the highest loading, LC-03-01-02, one engine out conditions with AC1 retracting at -54°C.

Even though the spar-box web at AC1 is loaded in tension, it experiences the highest shear load out of all considered subcases. If the buckling behaviour is dominated by compression

and not shear, the eigenvalues will be negative and their magnitude is considered to be similar to the positive eigenvalue value that would be obtained if the subcase with actuator extending (loading the web in compression) is run. This is because the rudder loading is very similar, with slightly lower shear and the compressive load of the jammed actuator has the same magnitude as the retracting case.

Regarding the spar-box, the GFEM mesh is refined from 56 elements to a DFEM containing 23976 elements, to better capture the buckling pattern and load. The buckling analysis is also run for a DFEM containing 168742 elements, to check the mesh reliability. Most of the utilised elements are CQUAD4, with a few CTRIA3 elements being used due to the tapered nature of the box shape.

The only discrepancy in the buckling analysis setup from the local torsion stiffening concept is represented by the boundary condition extension to the nodes modelling the box attachment to the rudder shells, which are the common nodes between the AC2 box web and the box lateral walls. The displacements of the three translational degrees of freedom corresponding to the original GFEM nodes, extracted from the static analysis, are enforced on the DFEM using the SCPD card and interpolated for the new nodes pertaining to the DFEM nodes. As previously stated, the SCPD card captures both the box loading and the boundary conditions.

The omission of the rotational displacements renders the analysis conservative, as virtually, the moments can not be carried by the constrained edges [51], leading to a buckling mode development closer to the edges, and the interpolation is performed by using the shape function defining the mesh nodes. The comparison between the GFEM and DFEM meshes can be visualised in Figure 6.3. The GFEM model features the displacement distribution in mm for the critical load case LC-03-01-02, where the black dots represent the nodes that carry the displacement information that is imposed on the DFEM model using the SPCD card, its application being visually represented by yellow triangles.

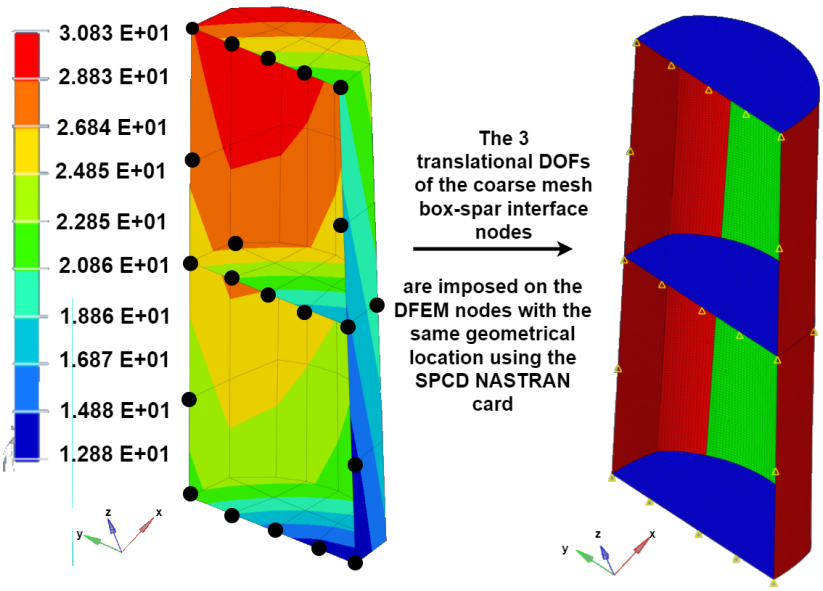

Figure 6.3: On the Left, the GFEM Displacement Distribution for LC-03-01-02. On the Right, the DFEM Mesh and SPD Visualisation for the Decoupled Spar-box

From the applied displacements, the solver is able to compute the resulting loading. Since **REQ-05-DESIGN** only requires a check for buckling under ultimate load. Hence, obtaining eigenvalues with a magnitude above one is sufficient to indicate that the spar-box will not buckle under the applied load. The correct displacement enforcement is tested by running a static analysis with the refined mesh, considering that the SPCD card is able to capture the box deformation but also the movement of the box due to the bending of the fin box.

Similarly to the previous concept, the displacements extracted from the GFEM mesh at the nodes modelling the interface between the box and the spar, and the box and the shells, are interpolated for the rest of the DFEM nodes that constitute the two interfaces, using the nodal shape function, as shown in Figure 6.5. The correct interpolation of the SPCDs is checked by running a static analysis for the DFEM as well. The results indicate complementary displacement values, the plot depicted in Figure 6.5 representing the resultant displacements in mm.

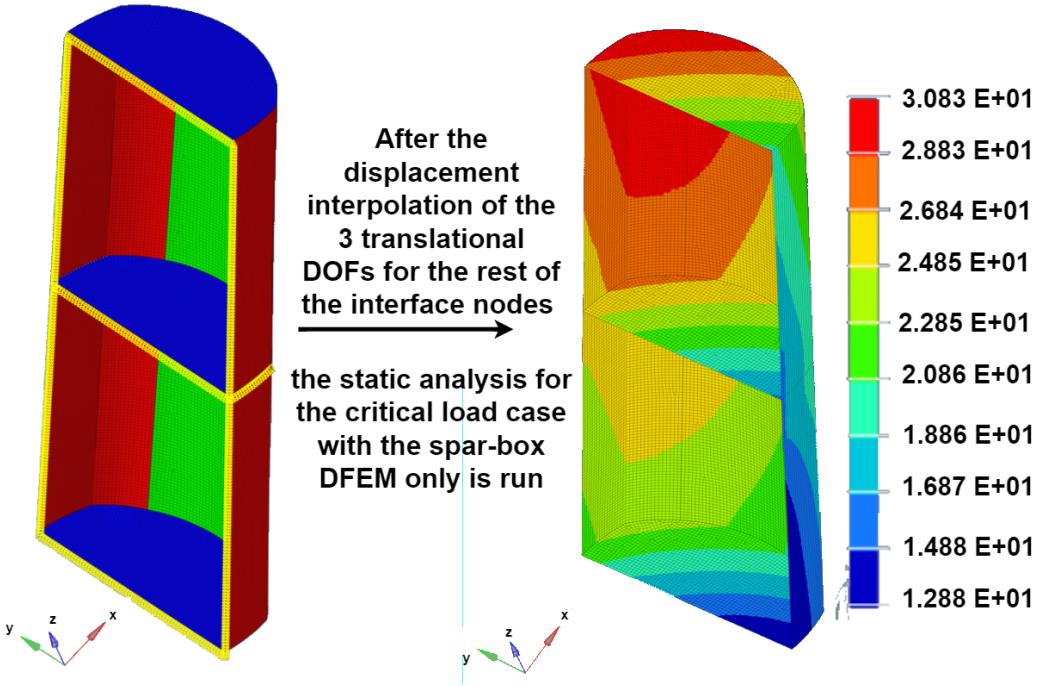

Figure 6.4: On the Left, SPCD Interpolation on the DFEM. On the Right, the Resultant Displacement from Static FEM Analysis of the Spar-box DFEM

The same procedure has been applied to the isolated monolithic region in the rudder shells. Since the left-hand side is loaded with higher loads due to the actuator jamming, the results are presented for this side only. The mesh has been refined from 6 elements to 7040 elements, and the three translational displacements corresponding to the original 14 nodes are interpolated to cover all 4 edges, the congruent resultant displacements yielded by static simulations using the GFEM and the DFEM being provided in Figure 6.5.

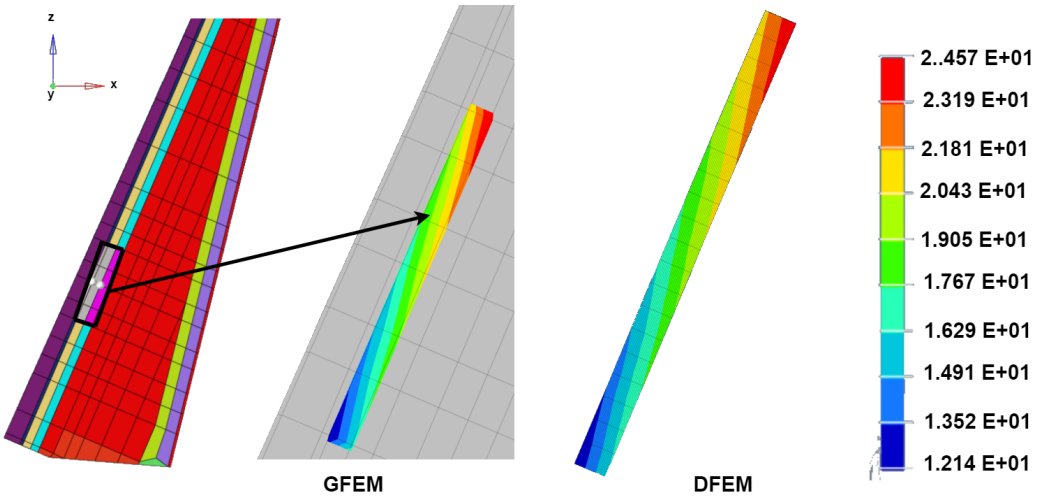

Figure 6.5: Resultant Displacement from Static FEM Analysis in the Extended Monolithic Area using the Coarse Mesh (on the Left) and the Refined Mesh (on the Right)

6.2.2 Buckling Analysis Results

In the case of the decoupled spar-box final design, the first eigenvalue is -2.17, with the first eigenmode occurring in the AC1 web, with one half-wave, as illustrated in Figure 6.6. The second eigenvalue is also -3.46, occurring in the left lateral wall below AC2 as shown in Figure 6.6 and the third eigenvalue is 3.5, occurring in the left web, above AC2. The linear buckling analysis indicates that even though the box-rudder connection at AC2 is a highly loaded area, the local loads introduced in the box webs due to actuator jamming are higher. The relative difference between the two refined meshes for the first eigenvalue is 3.7%, corroborating the mesh quality.

The results imply that the compression load that is exerted by the jammed actuator while it extends dominates the buckling behaviour of the box, due to the negative sign of the first eigenvalue. Since the second and the third eigenvalues have close magnitudes but different signs at the location of AC2, where the connection between the box and the shells is located, this buckling behaviour could be attributed to shear buckling [47]. Moreover, the fourth and the fifth modes show similar behaviour, with one eigenvalue positive and the other one negative, with resembling buckling modes at the location of AC2, but on the right-hand side of the box.

Given that the jamming loads do not change orientation for the jamming actuator while extending, and that the shear loads are slightly lower (order of a few tens of micro-strains), the positive eigenvalues that would be obtained for this load case (LC-03-02-02) would be close in magnitude. As the obtained magnitudes of the eigenvalues are above 1, the proposed spar-box design meets the buckling requirement **REQ-05-DESIGN**.

The buckling results for the rudder shell monolithic area also indicate alignment with **REQ-05-DESIGN**, as the first two eigenvalues are -6.505 and 6.536, indicating shear dominance. With the magnitude of the eigenvalues above 1, the monolithic area will not buckle under the

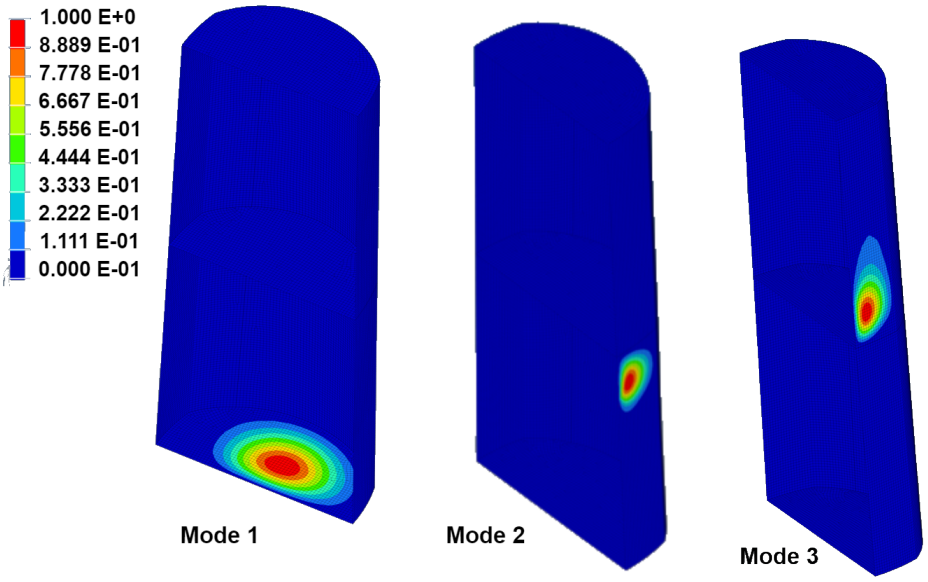

Figure 6.6: Buckling Mode 1 (Most Left), Mode 3 and Mode 2 (Most Right) for the Decoupled Spar-box Concept

ultimate loads acting on the rudder.

6.3 Decoupled Concept Final Design

By making use of the insights gained due to the optimisation of the local torsion stiffening concept, it has been concluded that the optimal height of the decoupled spar-box design is 160 mm, with an additional increase in roof and box-webs thickness to 4.9 mm and a curved box-top design. The final thicknesses and layer sequence are given in Table 6.3 per spar-box component.

Region	Layup	Thickness [mm]
Walls	$[45^\circ_3/0°/45^\circ_2]_s$	4.2
Roof	$[45^\circ_3/0°/45^\circ_3]_s$	4.9
Webs	$[45°/0^\circ_3/45°/0^\circ_2]_s$	4.9
Spar	$[0^\circ_2/45°/0^\circ_2]_s$	3.5

Table 6.3: Spar-box Component Final Layup Sequence

As the structural decoupling limits the introduction of the actuator jamming loads predominantly to the spar-box, the decoupled concept achieves the goal of reducing the shell loading more efficiently, as for the final proposed design both the minimum rudder shell and spar-box reserve factors are close to 1. The lower reserve factors in the spar-box webs required the box strains monitoring in parallel to the shell, emphasizing that the curved top design reduces the shear strain levels in the box, as the curved design has a higher polar moment of inertia,

influencing the value of the twist and consequently the shear strain. The final weight of the box is 4.25 kg for minimum reserve factors above 1, complying with **REQ-01-DESIGN** and **REQ-04-DESIGN**. The final dimension overview is provided in Figure 6.7.

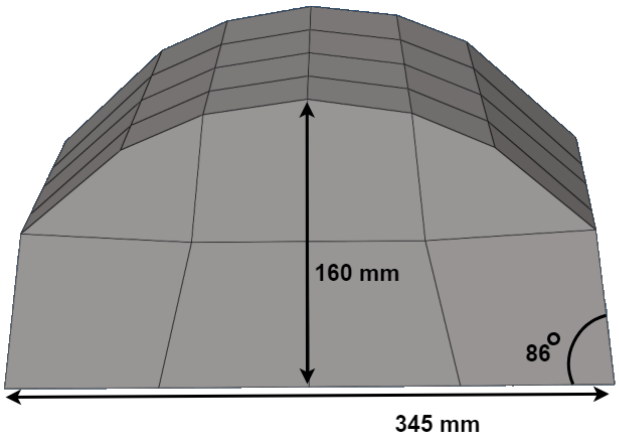

Figure 6.7: Final Dimensions for the Decoupled Sapr-box Design Shown on the FEM Mesh used for the Static Analysis Shown on the GFEM Mesh

The buckling analyses indicate the design viability, as the magnitude of the eigenvalues is above 1, in both spar-box and extended monolithic area in the rudder shells, the design is compliant with **REQ-02-DESIGN**. Even though the buckling is a result of the combined contribution of compression and shear, the first eigenvalue is attributed mostly to compression in the area of AC 1 (in the box web) and the following modes to shear in the area of AC 2.

For the critical load case of each rudder component, the integrity of all rudder structural elements is checked, with the corresponding minimum reserve factors provided in Table 6.4 in comparison to the ones recorded in the current, original design.

Bracket Material	LC	$\frac{\varepsilon_{XX}}{\varepsilon_{XX,allow}}$	$\frac{\varepsilon_{YY}}{\varepsilon_{YY,allow}}$	$\frac{\gamma_{XY}}{\gamma_{XY,allow}}$	RF	Location
Rud. Shell Original	03-01-02	0.09	0.35	0.70	1.27	Ramp Above AC 1
Rud. Shell Updated	03-01-01	0.15	0.12	0.97	1.01	Ramp Above AC 1
Spar Original	03-01-02	0.01	0.11	0.81	1.22	Web at AC 1
Spar Updated	03-01-01	0.01	0.08	0.94	1.06	Web at AC 1
AC Brackets	03-01-01	0.02	0.15	0.57	1.70	AC 1 Attachment
Box	03-01-01	0.02	0.12	0.94	1.05	AC 1 web

Table 6.4: Rudder Components Minimum Reserve Factors

The AC brackets have the minimum reserve factor in the actuator attachment area (Region 1), with the highest values as expected in the AC 1 bracket. As the spar reserve factor is close to 1, no further modifications have been performed on the lay-up sequence. Additionally, the von Mises strains in the metallic hinge arm brackets did not undergo relative changes higher than 5%.

Moreover, the load transfer at the shell elements with peak strains does not change significantly from the trade-off results. Hence, as proven in the trade-off, the decoupled design is compliant with **REQ-02-DESIGN** and **REQ-03-DESIGN**. Additionally, the maximum leading edge displacement obtained for the critical load case, 5.8 mm, does not alter significantly from the maximum leading edge displacement of the original design, 5.4 mm, obtained for the same load case. Without the extension of the monolithic area to the first elements below AC1 and above AC3, the rudder shell reserve factors would have been below 1 for the proposed spar-box design (disregarding the rudder shell elements containing the nodes connecting the box and the shells).

6.4 Notes on Results Verification and Validation

Throughout the study, result verification steps have been constantly undertaken for each design change that has been performed on the original (current) rudder design. However, before a summary of the verification activities is provided below, one aspect has been so far neglected during the spar-box optimisation: the mesh size influence on the rudder shell minimum reserve factors and a mesh convergence study.

The reasoning behind the lack of mesh stability investigations for the static analyses is presented in subsection 6.4.1 and the notes on verification and validation for the static, modal and buckling analyses are described in subsection 6.4.3.

6.4.1 Mesh Size and Stability

The spar-box has been consistently modelled with element sizes compatible with the provided GFEM, which has been verified and experimentally validated by Airbus, with tests conducted on the real-scale single-aisle VTP. The overall VTP mesh is coarse, as the strain allowables used to compute the reserve factors were determined as far-field strains. These strain allowables and mesh size are considered appropriate for a preliminary design, and due to the GFEM model experimental validation, no mesh convergence tests have been performed. The buckling eigenvalues have been compared for two different DFEM mesh sizes, with a relative difference below 5%, showing convergence.

To provide consistent results, the spar-box has been meshed with elements of the same size as the spar and shells' elements. However, extra static simulations have been performed for the final spar-box designs of both concepts, with the mesh doubled in size. This is considered an important step, as the minimum shell reserve factors have been reduced to values of 1.01. With a more refined spar-box mesh, the rudder shell strains decreased on average by 5%, rendering the spar-boxes design with all components thickness set to 4.2 mm a viable design.

As a thickness change of 0.7 mm in some of the spar-box components, to obtain rudder shell reserve factors above 1, leads to a box weight increase between 100 and 200 grams, determining the exact spar-box components thickness becomes rather an experimental task. The study aims to provide a spar-box preliminary design, which has identified the suitable spar-box thicknesses being around the value of 4.2 mm.

Moreover, considering that the strain allowables represent far-field strains, if the numerical values of the strains belonging to the critical element are averaged with the strains of the

adjacent elements, the resulting reserve factors would be above 1 with the spar-box mesh as well. After all, does a reserve factor of 0.99 lead to structural failure? Does the thickness increase of the spar-box top really improve the structural performance? These questions can be only reliably answered by experimental testing. For the current study, a line has to be drawn to provide a design solution and is defined by the design requirements, including the one regarding reserve factors. The proposed spar-box designs meet these requirements, for spar-box FEM models compatible with the provided GFEM mesh.

6.4.2 Material Change in Actuator Brackets

The first change introduced in the rudder design was the actuator bracket material substitution, from metallic to composite. The correct modelling has been verified by modelling the brackets with both PCOMP and PSHELL properties, resulting in relative differences in rudder shell reserve factors below 7% for non-sizing load cases and below 5% for the sizing load case. The design can be further improved by using unidirectional tape instead of fabric, which can better tailor the layup sequence to maximise the mechanical properties, for the same thickness.

6.4.3 Spar-box Modelling and Static Analyses

Considering that the reserve factors are computed based on strain allowables determined experimentally for far-field strains, obtaining reserve factors above 1 is considered a result validation method for static analyses. The correct addition of the spar-box to the original FEM model has been constantly checked for the presence of free edges, which indicates disruptions in mesh connection, double grid points and double elements.

Moreover, the positive results of modal analysis corresponding to the decoupled concept, which did not lead to new mode shapes and natural frequencies alterations above 7%, have been checked with a simulation comparing the local rudder bending stiffness, indicating as expecting displacement relative differences of 73% and with another modal simulation for a rudder-box grid connection moved more aft, which did result in a new modal shape. The only modal results that can be validated are the original natural frequencies.

Furthermore, The correct displacement enforcement and interpolation on the spar-box DFEM used for the buckling analyses have been verified by comparing the displacements yielded by the static simulations against the displacements obtained with the GFEM, resulting in congruent values. Given the verified and validated GFEM, verification methods using the analytical approaches are redundant, as the aim of the thesis was not the creation of a new calculation tool or development of a novel methodology, but rather a novel structural design.

Chapter 7

Conclusion

The aim of the thesis was to provide a feasibility study and preliminary design for a rudder torsion box spar, sized for static loading, enabling load alleviation in the Airbus single-aisle sandwich rudder shells, caused by actuator force-fighting loads. The torsion box spar would act as a substitute for the current additional CFRP layers in the shell actuator area, rendering the relatively low aerodynamic loads the main forces acting on the shells. Hence, sustainable materials, with lower mechanical properties or manufacturing challenges, could be introduced in primary aircraft structures.

The current feasibility study used the thermoset material properties in the rudder shells, as the torsion box spar would become the enabler for the usage of green materials in future studies. After the load selection, which included three sizing corners from the fin bending-rudder hinge moment envelope at the VTP root, two main mechanisms that enable the separation between the internal and external loads have been identified: locally increasing the torsional stiffness in the area of the actuators by designing the rudder spar as a box while still retaining the shell-spar connection (through riveting) or structurally decoupling the spar-box from the shell by removing the riveted interface in the area of the actuators.

As the rudder actuator brackets are the load-introduction structure of the jamming loads, the possibility of incorporating them in the spar-box design has also been investigated, by modifying their material from metallic to composite and by connecting them to the spar-box top via composite webs. The possibility of retaining the current metallic design of the brackets has also been studied through a spar-box concept that incorporated the first principle while connecting the actuator brackets to the spar-box top with metallic truss structures.

However, during the trade-off process, it was discovered that despite the high stiffness assigned to the trusses, the concept (with metallic actuator brackets) failed to reduce the loads in the shells and introduced a new first natural frequency, indicating the unfeasibility of the truss concept. In comparison, the trade-off results also indicated the importance of the spar-box webs connecting the composite brackets to the top of the spar-box in directing the jamming loads in the box and not the shells, as the unfeasibility of the truss concept can not be attributed to the bracket material (the composite brackets have slightly lower stiffness).

The two concepts with carbon actuator brackets successfully maintained the shell reserve factors above 1 under jamming load conditions. Moreover, in the case of the decoupled concept, where various issues were expected due to the interface decoupling, the modal analysis showed the concept viability, as the natural frequencies did not change more than 7% due to the spar-box-shell connection close to the spar web, which ensures a relatively similar connection stiffness as the original design. Additionally, basic calculations for bearing stress indicated successful load transmission capabilities, as the minimum required rivet pitch has not been crossed. Due to the comparable trade-off scores of the two composite actuator brackets concepts, both designs have been further optimised for proposed preliminary designs.

The first major rudder design alteration was represented by the actuator brackets material change to composite. The use of fabrics limits the material's attainable mechanical properties (maximum 59 MPa membrane stiffness), leading to a rudder shell minimum reserve factor reduction from 1.27 to 1.24 compared to the original, current rudder design (the aluminium's stiffness is 70 MPa). Thus, the use of unidirectional tapes is the first point of design improvements that can be considered in future studies, as they better allow for material property tailoring. Hence, the composite brackets could attain the same material stiffness as the original design, reducing the minimum reserve factor gap.

The rudder shell's original minimum reserve factor is 1.27, but during the spar-box optimisation process, it was allowed to drop to 1.01. The first reason is that the strain allowables are very conservative and the concepts' weight obtained for reserve factors of 1.01 can challenge the values of the allowables, which can be better tailored for the load case and fibre orientation of the structure.

Secondly, Airbus uses further design knock-down factors, related to manufacturing, which might not be relevant anymore if the rudder shell material changes. For a shell minimum reserve factor of 1.01, the optimised weight of both spar-box concepts is smaller than the weight of the current reinforcement (8.5 kg). Rudder shell minimum reserve factors comparable to the current design are attained for a higher spar-box weight (around 12.5 kg). Hence, if the exact value of reserve factors is required, the solution provided by the torsion box would be a slightly heavier one.

During the optimisation process, the decoupled concept (4.2 kg) results in lower mass compared to the local torsion stiffening concept (6.4 kg). The decoupled concept is more weight-effective because the jamming loads are de-coupled. With the local torsion stiffening concept, the rudder shells are still connected to the spar; thus, some jamming loads are still transferred to the shells. Since the area enclosed by the rudder shells is always higher than the profile area of the box, the later structure has to compensate with a high area, even though the loads in the box itself are not that high.

The decoupled concept better uses the design to redistribute the jamming loads in the box, as the minimum reserve factors of the spar-box itself are also close to 1 compared to the other concept, where the minimum reserve factor is around 1.5. As the spar-box component thickness plays a lesser role in reducing the strain levels in the shells, the two concepts have similar component thicknesses. The most important spar-box parameter is represented by the enclosed area, influenced mainly by the spar-box height due to the limited design space imposed by the rudder shell planform triangular, fixed cross-sectional geometry. Additionally, the span that minimises the box weight and ensures acceptable loads in the shells is equal to the distance between the most lower and upper actuator brackets.

The viability of the decoupled concept requires more detailed dynamic and aeroelastic analyses, as no transient simulation has been conducted in this thesis (only a modal analysis has been used as a first feasibility indicator). Moreover, the decoupled concept undergoes higher stiffness alterations due to the structural de-coupling, materialised in the removal of riveted spar-shell interfaces, to which the aeroelastic results are susceptible.

The spar-box optimisation itself can be improved by using a finer mesh, which can be connected to the VTP GFEM by using RBE rigid elements, as the weight of the spar-box could be improved due to a better height and top box shape sensitivity analysis. The current study investigated the height sensitivity with change variations of 20 mm and 40 mm, but an automated optimisation routine applied on a finer mesh could lead to weight savings of a few hundred grams compared to the current solution.

Moreover, it has also been observed that a curved shape of the box top leads to weight reductions compared to a straight top geometry, and also alleviates the loads at the critical locations in the box webs. The decoupled concept also indicated the load reduction in the spar-box web in the area of the jammed actuator, as the maximised polar moment of inertia reduces the twist, and consequently the shear strain. An automatised routine could also improve the shape sensitivity study for two box top geometries (straight and curved) with the same enclosed area instead of the same box height.

For a preliminary design, the workload can be further reduced by considering fewer load subcases, as analysing the two temperature subcases does not lead to a significant discrepancy between the minimum reserve factors and their location. Moreover, the jamming of AC 1 and AC 3 produces similar reserve factors, thus subcases involving AC 3 can be disregarded during a preliminary concept design. Additionally, the gust load case can be entirely skipped, as there is no rudder hinge moment, and subsequently the loads acting on the rudder are very small, as the lateral gusts lead to the formation of an aerodynamic pressure (and thus bending) on the VTP fin, which has a considerably larger surface area. Opting for only one jamming load direction (when the actuator is either extending or retracting) can further simplify the preliminary analysis, as the resulting minimum reserve factors are not considerably different.

Future studies could include details regarding the efficient manufacturing of the spar-box, its integration in the rudder structure, assembly and the interface design of the box and the spar (given the spar web is split into 4 components). Furthermore, a non-linear buckling analysis could provide more conservative buckling loads and post-buckling performance, as the stiffness matrix is updated for each incremental step. In this case, the jamming of the actuator while extending should be considered

Conclusively, the current study has proven the spar-box concept feasibility to supersede the currently reinforced rudder shells, enabling further research regarding the use of sustainable materials in rudder shells. The rudder shell material properties can be changed in the first step with carbon thermoplastic material and subsequently bio-materials, with lower mechanical properties.

References

[1] S. al Jaberi. Application of c/pekk ud tape for welded aircraft movables. *Master Thesis, TU Delft, Delft*, 2018.

[2] E. Barkanov, O. Ozoliņš, E. Eglitis, F. Almeida, M. C. Bowering, and G. Watson. Optimal design of composite lateral wing upper covers. part i: Linear buckling analysis. *Aerospace Science and Technology*, 38:1–8, 2014. ISSN 12709638. doi: 10.1016/j.ast.2014.07.010.

[3] E. Barkanov, E. Eglitis, F. Almeida, M. C. Bowering, and G. Watson. Optimal design of composite lateral wing upper covers. part ii: Nonlinear buckling analysis. *Aerospace Science and Technology*, 51:87–95, 4 2016. ISSN 12709638. doi: 10.1016/j.ast.2016.01.020.

[4] C. Bisagni and R. Vescovini. Analytical formulation for local buckling and post-buckling analysis of stiffened laminated panels. *Thin-Walled Structures*, 47:318–334, 3 2009. ISSN 02638231. doi: 10.1016/j.tws.2008.07.006.

[5] R. P. Cardoso. A new beam element which blends the euler-bernoulli beam theory with idealised transverse shear flows for aircraft structural analysis. *Thin-Walled Structures*, 157, 12 2020. ISSN 02638231. doi: 10.1016/j.tws.2020.107118.

[6] B. Castanie, C. Bouvet, and M. Ginot. Review of composite sandwich structure in aeronautic applications. *Composites Part C: Open Access*, 1, 8 2020. ISSN 26666820. doi: 10.1016/j.jcomc.2020.100004.

[7] B. Castanié, J. J. Barrau, J. P. Jaouen, and S. Rivallant. Combined shear/compression structural testing of asymmetric sandwich structures. *Experimental Mechanics*, 44:461–472, 10 2004. ISSN 00144851. doi: 10.1177/0014485104047607.

[8] D. Chatterjee, A. Ghosh, and D. Chakravorty. Finite element prediction of first-ply failure loads of composite thin skewed hypar shells using nonlinear strains. *Thin-Walled Structures*, 167, 10 2021. ISSN 02638231. doi: 10.1016/j.tws.2021.108159.

[9] R. Cirillo. Detailed and condensed finite element models for dynamic analysis of a business jet aircraft. *Master Thesis, Politecnico di Milano, Milano*, 2011.

[10] EASA:. Acceptable means of compliance for large aeroplanes cs-25. tech. rep. amendment 17. european aviation safety agency, 2015. URL https://www.easa.europa.eu/en/document-library/certification-specifications/group/cs-25-large-aeroplanes#cs-25-large-aeroplanes.

[11] J. H. Fogarty. Honeycomb core and the myths of moisture ingression. *Applied Composite Materials*, 17:293–307, 6 2010. ISSN 0929189X. doi: 10.1007/s10443-009-9121-7.

[12] J. Ge, M. Luo, D. Zhang, G. Catalanotti, B. G. Falzon, J. McClelland, C. Higgins, Y. Jin, and D. Sun. Temperature field evolution and thermal-mechanical interaction induced damage in drilling of thermoplastic cf/pekk – a comparative study with thermoset cf/epoxy. *Journal of Manufacturing Processes*, 88:167–183, 2 2023. ISSN 15266125. doi: 10.1016/j.jmapro.2023.01.042.

[13] M. Ginot, M. D'Ottavio, O. Polit, C. Bouvet, and B. Castanié. Benchmark of wrinkling formulae and methods for pre-sizing of aircraft lightweight sandwich structures. *Composite Structures*, 273, 10 2021. ISSN 02638223. doi: 10.1016/j.compstruct.2021.114387.

[14] M. Ginot, C. Bouvet, B. Castanie, M. D'Ottavio, J. Serra, and N. Mahuet. Local buckling on large sandwich panels applied to light aviation: Experimental and computation dialogue. *International Journal of Solids and Structures*, 268, 4 2023. ISSN 00207683. doi: 10.1016/j.ijsolstr.2023.112170.

[15] P. J. Gray, R. M. O'Higgins, and C. T. McCarthy. Effect of thickness and laminate taper on the stiffness, strength and secondary bending of single-lap, single-bolt countersunk composite joints. *Composite Structures*, 107:315–324, 1 2014. ISSN 02638223. doi: 10.1016/j.compstruct.2013.07.014.

[16] J. T. Hang, W. Zhao, L. Liu, and G. K. Xu. Damage sensitivity studies of composite honeycomb sandwich structures under in-plane compression and 4-point bending: Experiments and numerical simulations. *Composite Structures*, 321, 10 2023. ISSN 02638223. doi: 10.1016/j.compstruct.2023.117279.

[17] L. Hart-Smith. Lessons learned from the dc-10 carbon-epoxy rudder program. *Transactions*, vol. 95:686–702, 1986.

[18] S. R. Hegde and M. Hojjati. Performance of composite sandwich structures under thermal cycling. *Journal of Composite Materials*, 54:271–283, 1 2020. ISSN 1530793X. doi: 10.1177/0021998319862324.

[19] M. Higgins and H. Benaroya. Utilizing the analytical hierarchy process to determine the optimal lunar habitat configuration. *Acta Astronautica*, 173:145–154, 8 2020. ISSN 00945765. doi: 10.1016/j.actaastro.2020.04.012.

[20] C. Horgan and J. Sbmonds. Saint-venant end effects in composite structures, 1994.

[21] J. V. Ingen, A. Buitenhuis, M. V. Wijngaarden, and F. Simmons. Development of the gulfstream g650 induction welded thermoplastic elevators and rudder. *Conference Paper*, 5 2010.

[22] M. N. B. Kamarudin, J. S. M. Ali, A. Aabid, and Y. E. Ibrahim. Buckling analysis of a thin-walled structure using finite element method and design of experiments. *Aerospace*, 9, 10 2022. ISSN 22264310. doi: 10.3390/aerospace9100541.

[23] Y. Karsandik, B. Sabuncuoglu, B. Yildirim, and V. Silberschmidt. Impact behavior of sandwich composites for aviation applications: A review. *Composite Structures*, 314, 6 2023. ISSN 02638223. doi: 10.1016/j.compstruct.2023.116941.

[24] C. Kassapoglou. Compression strength of composite sandwich structures after barely visible impact damage. *Journal of Composites Technology and Research*, 18:274–284, 1996. ISSN 08846804. doi: 10.1520/ctr10113j.

[25] C. Kassapoglou. *Design and analysis of composite structures: With applications to aerospace structures, 2nd ed.* New York: John Wiley & Sons, 2013. ISBN 9780470972632.

[26] E. Kececi and R. Asmatulu. Effects of moisture ingressions on mechanical properties of honeycomb-structured fiber composites for aerospace applications. *International Journal of Advanced Manufacturing Technology*, 88:459–470, 1 2017. ISSN 14333015. doi: 10.1007/s00170-016-8744-8.

[27] N. N. Kermani, P. Simacek, and S. G. Advani. Porosity predictions during co-cure of honeycomb core prepreg sandwich structures. *Composites Part A: Applied Science and Manufacturing*, 132, 5 2020. ISSN 1359835X. doi: 10.1016/j.compositesa.2020.105824.

[28] S. Kumar and B. Reddy. Design and linear static analysis of transport aircraft vertical tail for different rudder deflection. *International Journal for Scientific Research and Development*, vol. 3, 2015. ISSN 2321-0613.

[29] G. Li, G. Renaud, and M. Liao. *Assessing the riveting process and the quality of riveted lap joints in aerospace and other applications*, pages 383–426. Elsevier, 2021. doi: 10.1016/b978-0-12-819140-8.00013-4.

[30] S. Liu, Z. Zhang, J. Zhao, X. Wu, X. Hong, and H. Liu. A comparative study on milling-induced damages and residual tensile strength during milling of thermoplastic and thermoset carbon fibre reinforced polymers. *Polymer Testing*, 125:108132, 8 2023. ISSN 01429418. doi: 10.1016/j.polymertesting.2023.108132.

[31] X. Liu, C. A. Featherston, and D. Kennedy. Two-level layup optimization of composite laminate using lamination parameters. *Composite Structures*, 211:337–350, 3 2019. ISSN 02638223. doi: 10.1016/j.compstruct.2018.12.054.

[32] Y. Ma, Z. Kou, Y. Hu, J. Zhou, Y. Bei, L. Hu, Q. Huang, P. Jia, and Y. Zhou. Research advances in bio-based adhesives. *International Journal of Adhesion and Adhesives*, 126, 8 2023. ISSN 01437496. doi: 10.1016/j.ijadhadh.2023.103444.

[33] G. Malucelli and A. Kausar. Green composites and nanocomposites for aerospace applications. *Polymeric Nanocomposites with Carbonaceous Nanofillers for Aerospace Applications*, pages 297–316, 1 2022. doi: 10.1016/B978-0-323-99657-0.00014-4.

[34] P. Minguet. A model for predicting the behavior of impact-damaged minimum gage sandwich panels under compression. American Institute of Aeronautics and Astronautics (AIAA), 4 1991. doi: 10.2514/6.1991-1075.

[35] R. C. Moody and A. J. Vizzini. Damage tolerance of composite sandwich structures, 2000. URL https://www.tc.faa.gov/its/worldpac/techrpt/ar99-91.pdf.

[36] MSC. Nx nastran quick reference guide version 10.

[37] A. Mubashar, I. A. Ashcroft, G. W. Critchlow, and A. D. Crocombe. Investigation of moisture ingress and migration mechanisms of an aircraft rudder composites sandwich structure. *Journal of Adhesion*, 85:711–735, 2009. ISSN 00218464. doi: 10.1080/00218460902997224.

[38] S. S. Naarayan, D. V. P. Kumar, and S. Chandra. Implication of unequal rivet load distribution in the failures and damage tolerant design of metal and composite civil aircraft riveted lap joints. *Engineering Failure Analysis*, 16:2255–2273, 10 2009. ISSN 13506307. doi: 10.1016/j.engfailanal.2009.03.016.

[39] M. Oiwa, T. Ogasawara, H. Yoshinaga, T. Oguri, and T. Aoki. Numerical analysis of face sheet buckling for a cfrp/nomex honeycomb sandwich panel subjected to bending loading. *Composite Structures*, 270, 8 2021. ISSN 02638223. doi: 10.1016/j.compstruct.2021.114037.

[40] R. Rikards. Optimal design with advanced materials. in elaboration of optimal design models for objects from data of experiments. pages 149–162, 1993. doi: 10.1016/B978-0-444-89869-2.50016-0.

[41] K. M. Roughen, M. L. Baker, and T. Fogarty. Computational fluid dynamics and doublet-lattice calculation of unsteady control surface aerodynamics. *Journal of Guidance, Control, and Dynamics*, 24:160–166, 2001. ISSN 07315090. doi: 10.2514/2.4697.

[42] T. L. Saaty. A scaling method for priorities in hierarchical structures, 1977.

[43] S. Z. Shah, P. S. Megat-Yusoff, S. Karuppanan, R. S. Choudhry, F. Ahmad, Z. Sajid, P. Gerard, and K. Sharp. Performance comparison of resin-infused thermoplastic and thermoset 3d fabric composites under impact loading. *International Journal of Mechanical Sciences*, 189, 1 2021. ISSN 00207403. doi: 10.1016/j.ijmecsci.2020.105984.

[44] S. Z. Shah, P. S. Megat-Yusoff, S. Karuppanan, R. S. Choudhry, I. U. Din, A. R. Othman, K. Sharp, and P. Gerard. Compression and buckling after impact response of resin-infused thermoplastic and thermoset 3d woven composites. *Composites Part B: Engineering*, 207, 2 2021. ISSN 13598368. doi: 10.1016/j.compositesb.2020.108592.

[45] Z. Song, S. Luong, D. Whisler, and H. Kim. Honeycomb core failure mechanism of cfrp/nomex sandwich panel under multi-angle impact of hail ice. *International Journal of Impact Engineering*, 150, 4 2021. ISSN 0734743X. doi: 10.1016/j.ijimpeng.2021.103817.

[46] A. Sudhin, M. Remanan, and K. Jayanarayanan. Comparison of properties of carbon fiber reinforced thermoplastic and thermosetting composites for aerospace applications. *Materials Today: Proceedings*, 24:453–462, 2020.

[47] H. Sun, C. Wen, Y. Hou, Y. Guo, and W. Bai. Overall flexural-shear buckling strength design of built-up radially battened columns. *Journal of Building Engineering*, 79:107834, 11 2023. ISSN 23527102. doi: 10.1016/j.jobe.2023.107834.

[48] T.H.G.Megson. *Aerospace Structural Design an Analysis, 4th ed.* Oxford, UK: Elsevier, 2007. ISBN -13: 978-0-75066-7395.

[49] J. Tomblin, T. Lacy, B. Smith, S. Hooper, A. Vizzini, and S. Lee. Review of damage tolerance for composite sandwich airframe structures, 1999. URL https://www.tc.faa.gov/its/worldpac/techrpt/ar99-49.pdf.

[50] A. Wang, Z. Wang, M. Zhao, Y. Zhao, and Z. Chang. Effects of ply thickness and interference-fit on the bearing strength of single-lap countersunk composite joints. *Thin-Walled Structures*, 189, 8 2023. ISSN 02638231. doi: 10.1016/j.tws.2023.110878.

[51] P. Wang, Y. Chen, R. Pei, C. Lian, K. Zhang, and Y. Zhou. Buckling and post-buckling analysis of composite wing box under loads with torsion-bending coupling. *Thin-Walled Structures*, page 111266, 10 2023. ISSN 02638231. doi: 10.1016/j.tws.2023.111266.